

Summertime productivity and carbon export potential in the Weddell Sea, with a focus on the waters adjacent to Larsen C Ice Shelf

Raquel F. Flynn^{1*}, Thomas G. Bornman^{2,3}, Jessica M. Burger¹, Shantelle Smith¹, Kurt A.M. Spence¹ and Sarah E. Fawcett^{1,4}

¹Department of Oceanography, University of Cape Town, Cape Town, South Africa

²South African Environmental Observation Network, Elwandle Coastal Node, Port Elizabeth, South Africa

³Institute for Coastal and Marine Research, Nelson Mandela University, Port Elizabeth, South Africa

⁴Marine and Antarctic Research centre for Innovation and Sustainability (MARIS), University of Cape Town, Cape Town, South Africa

*Correspondence to: Raquel F. Flynn (flyraq001@myuct.ac.za)

Abstract

The Weddell Sea represents a point of origin in the Southern Ocean where globally-important water masses form. Biological activities in Weddell Sea surface waters thus affect large-scale ocean biogeochemistry. During January/February 2019, we measured net primary production (NPP), nitrogen (nitrate, ammonium, urea) uptake, and nitrification in the western Weddell Sea at the Antarctic Peninsula (AP) and Larsen C Ice Shelf (LCIS), in the southwestern Weddell Gyre (WG), and at Fimbul Ice Shelf (FIS) in the south-eastern Weddell Sea. The highest average rates of NPP and greatest nutrient drawdown occurred at LCIS. Here, the phytoplankton community was dominated by colonial *Phaeocystis antarctica*, with diatoms increasing in abundance later in the season as sea-ice melted. At the other stations, NPP was variable, and diatoms known to enhance carbon export (e.g., *Thalassiosira* spp.) were dominant. Euphotic zone nitrification was always below detection, such that nitrate uptake could be used as a proxy for carbon export potential, which was highest in absolute terms at LCIS and the AP. Surprisingly, the highest f-ratios occurred near FIS rather than LCIS (average of 0.73 ± 0.09 versus 0.47 ± 0.08). We attribute this unexpected result to partial ammonium inhibition of nitrate uptake at LCIS (where ammonium concentrations were $0.6 \pm 0.4 \mu\text{M}$, versus $0.05 \pm 0.1 \mu\text{M}$ at FIS), with elevated ammonium resulting from increased heterotrophy following the accumulation of nitrate-fuelled phytoplankton biomass in early summer. Across the Weddell Sea, carbon export appears to be controlled by a combination of physical, chemical, and biological factors, with the highest potential export flux occurring at the ice shelves and lowest in the central WG.

Keywords: Nitrogen uptake, primary production, phytoplankton taxonomy, nutrient depletion, ammonium inhibition, Antarctic ice shelves

1. Introduction

The Southern Ocean is an important driver of Earth's climate as it transports large quantities of heat and dissolved gases, and supplies 65-85% of the global ocean's nutrients (Keffer and Holloway, 1988; Sarmiento et al., 2004; Frölicher et al., 2015; Keller et al., 2016; Fripiat et al., 2021). Despite the Southern Ocean's central role in atmospheric CO₂ removal (DeVries, 2014; Frölicher et al., 2015; Gruber et al., 2019), the incomplete drawdown of surface-water nutrients (i.e., nitrate, phosphate, and silicic acid) due to iron and light limitation of phytoplankton (Martin et al., 1991; Sunda and Huntsman, 1997) represents a missed opportunity for CO₂ removal (Sarmiento and Toggweiler, 1984). The Weddell Sea constitutes a point of origin in the Southern Ocean where water masses form and communicate with the atmosphere before subducting (Muench and Gordon, 1995; Talley et al., 2011), thereby setting the initial physical and chemical conditions of the deep global ocean. Biogeochemical cycling in the surface Weddell Sea thus has implications for carbon transfer to and storage in the ocean interior (Hoppema et al., 2004; Kerr et al., 2018). The southern and western Weddell Sea are bounded by ice shelves, which promote high rates of summertime phytoplankton productivity, nutrient drawdown and carbon export (El-Sayed and Taguchi, 1981; Hoppema and Goeyens, 1999; Hoppema et al., 2000), largely because the surface ecosystem is less iron- and light-limited in the ice shelf-adjacent waters than in the open Weddell Sea (Klunder et al., 2014).

The Weddell Sea is separated from the Antarctic Circumpolar Current (ACC) and open Southern Ocean by the Weddell Sea fronts (Orsi et al. 1995). The general large-scale circulation takes the form of the cyclonic, wind-driven and topographically-steered Weddell Gyre (WG) (Fahrbach et al., 1994, 1995; Orsi et al., 1995). The production of bottom water is thought to occur at two sites in the Weddell Sea: at Filchner-Ronne Ice Shelf (FRIS) and Larsen C Ice Shelf (LCIS) (Gordon et al., 1993; Schröder et al., 2002; Schodlok et al., 2002). Here, Modified Warm Deep Water (MWDW) intrudes onto the continental shelf and mixes with Antarctic Surface Water (ASW), which alters its physical and chemical properties, ultimately resulting in the formation of dense bottom waters. Upon reaching the Antarctic Peninsula (AP), the transformed bottom waters either spill out over the shelf and re-enter the ACC or are entrained into the eastward flowing limb of the WG (Orsi et al., 1993; Locarnini et al., 1993).

The surface waters of the open Weddell Sea surface waters are warm and saline while those over the continental shelf are relatively cool and fresh (Nicholls et al., 2004). These different waters are separated by the Antarctic Slope Front (ASF; Jacobs, 1986; 1991), a fast-flowing jet situated between the 500 m and 1000 m isobath that separates the Open Ocean Zone (OOZ) from the Coastal and Continental Shelf Zone (CCSZ; Jacobs, 1986; 1991; Muench and Gordon, 1995). The Antarctic CCSZ has been observed to host high rates of productivity in the summer (e.g., Smith and Nelson, 1990; Arrigo et al., 2008) as melting sea-ice supplies dissolved iron and increases water column stratification, yielding favourable conditions for phytoplankton growth (Lannuzel et al., 2008). Inputs of dissolved iron from continental shelf sediments and coastal runoff further elevate the ambient iron concentrations, such that the CCSZ seldom experiences iron-depletion (Klunder et al., 2014; Dinniman et al., 2020). As a result, the large phytoplankton blooms of the CCSZ can at times almost completely deplete the surface nitrate concentrations (Jennings et al. 1984; Hoppema et al. 2000; Henley et al. 2017), supporting high rates of carbon export that fuel the benthic community on the underlying continental shelf (Isla et al., 2006, 2011; Pineda-Metz et al., 2019) and/or eventually lead to long-term storage of atmospheric CO₂ in newly-formed AABW (Arrigo et al., 2008). In contrast, the OOZ is far less productive due to persistent iron-deplete conditions, along

with incidences of light limitation associated with high sea-ice concentrations (particularly in the central WG) and/or deep mixed layers (MLD) (Klunder et al., 2011; De Jong et al., 2012). Here, the co-limitation of productivity by iron and light typically yields low rates of biological carbon export (Boyd et al., 2008; Boyd and Ellwood, 2010; Klunder et al., 2011; De Jong et al., 2012).

On an annual basis, phytoplankton growth in the euphotic zone that is fuelled by nitrate supplied from below (i.e., “new production”) must be balanced by the export of sinking organic matter into the ocean interior (i.e., “export production”), thus driving CO₂ removal (Dugdale and Goering, 1967; Eppley and Peterson, 1979). By contrast, phytoplankton growth supported by nitrogen (N) sources that are recycled within the euphotic zone, such as ammonium and urea (i.e., “regenerated production”), results in no net removal of CO₂ to the deep ocean. The biologically-driven flux of carbon from surface waters, termed the “biological carbon pump”, transfers CO₂ to the isolated waters of the deep ocean, regulating the atmospheric concentration of this greenhouse gas (Volk and Hoffert, 1985). The high nutrient-low chlorophyll state of much of the Southern Ocean represents a “leak” in the ocean’s biological carbon pump since by consuming mixed-layer nutrients more completely, phytoplankton could theoretically lower atmospheric CO₂ (Sarmiento and Toggweiler, 1984). Indeed, one hypothesis for the decrease in atmospheric CO₂ that characterized the ice ages is more complete consumption of surface nutrients (i.e., a more efficient biological carbon pump) in the open Southern Ocean (Sigman and Boyle, 2000; Sigman et al., 2010; Martínez-García et al., 2014).

Since phytoplankton in the CCSZ of the Weddell Sea consume much of the nitrate supplied to the surface (Jennings et al. 1984; Hoppema et al. 2000), they should, by mass balance, drive the export of a significant amount of atmospheric CO₂ (“fixed” as biomass) to depth, a significant portion of which will be subducted in newly-formed bottom waters to be sequestered for >1000 years (Ito et al. 2010). Understanding the controls on biological nutrient utilization in the Weddell Sea, particularly in the CCSZ, is thus central to our understanding of its contribution to the Southern Ocean’s role in setting atmospheric CO₂. In general, phytoplankton growth in the Weddell Sea is regulated by the seasonal cycle of sea-ice, with the associated availability of light and iron imposing the main constraints (El-Sayed and Taguchi 1981). In winter, sea-ice formation and wind-driven mixing supply high concentrations of nutrients to ASW (Hoppema et al. 2007; 2015) that remain largely unconsumed due to the deep mixed layers and short days (Cota et al., 1992; Scharek et al., 1994; Spiridonov et al., 1996). Relief from light limitation in spring and early summer following increased water-column stratification due to sea-ice melt combined with enhanced solar radiation leads to the development of phytoplankton blooms. The size and duration of these blooms is ultimately dependent on macro- (e.g., nitrate and silicate) and micronutrient (e.g., iron) availability (Martin et al. 1991; Boyd 2004; Boyd and Ellwood 2010; Llorca et al. 2015), as well as zooplankton grazing (Smetacek et al., 2004 and references therein; Arteaga et al., 2020).

Observations suggest that Weddell Sea phytoplankton blooms are initially dominated by smaller species (e.g., *Phaeocystis antarctica*; 2-6 µm) that are well-adapted to the low-light conditions associated with deep springtime mixed layers (Moisan and Mitchell, 1999; Arrigo et al., 1999). As the season progresses, intensifying upper water-column stratification provides suitable growth conditions for larger phytoplankton such as diatoms (Goffart et al., 2000; Nissen and Vogt, 2021). Diatoms tend to rely heavily on nitrate as their dominant N source under high light

and nutrient conditions, and are generally outcompeted by smaller phytoplankton for ammonium (Probyn and Painting, 1985; Koike et al., 1986; Lomas and Glibert, 1999; Karsh et al., 2003). Diatoms are also a major vector for carbon export due to their rapid sinking rates facilitated by their generally larger size and biogenic silica ballasting (Tréguer et al., 2017). The seasonal shift in the Weddell Sea community from small, non-silicified phytoplankton to larger, more heavily-silicified species is thus associated with a significant increase in carbon export (Assmy et al. 2013). Concomitantly, sea-ice melt supplies high concentrations of dissolved iron to surface waters (up to 7 nM in the western Weddell Sea; Lannuzel et al., 2008; Klunder et al., 2014), which helps to support nitrate drawdown (Klunder et al., 2011, 2014). Eventually, as surface iron (and occasionally, nitrate; Hoppema, et al. 2000) concentrations again become limiting, phytoplankton rely proportionally more on ammonium and other regenerated N sources that have become increasingly available due to heterotrophic processing of the accumulated (i.e., bloom) biomass (Goeyens et al., 1995; Semeneh et al., 1998). The phytoplankton community consequently shifts once more towards smaller species that are better adapted to low iron conditions and specialize in the consumption of regenerated N, ultimately leading to a decrease in carbon export (Goeyens et al., 1995).

The Weddell Sea is particularly understudied near LCIS where thick sea-ice conditions persist year-round. To our knowledge, the only biogeochemical study conducted in the vicinity of LCIS was undertaken in the austral summer of 1992/3. Using measurements of nutrient depletion, Hoppema et al. (2000) estimated primary production in the vicinity of LCIS to be 47.5-95 mmol C m⁻² d⁻¹, while in the central Weddell Sea it was substantially lower at 8.3 mmol C m⁻² d⁻¹. However, because the study did not characterize the phytoplankton community, the extent to which phytoplankton diversity may have influenced primary production and nutrient drawdown cannot be surmised. To evaluate the summertime fertility of the Weddell Sea and the potential importance of different phytoplankton groups for carbon production and export, we directly measured the rates of total, new, and regenerated production in the western Weddell Sea (predominantly at LCIS), as well as at Fimbul Ice Shelf (FIS) in the south-eastern Weddell Sea. Rates of nitrification were also quantified to account for any nitrate regenerated within the euphotic zone at the time of sampling as this N flux supports regenerated rather than new production (e.g., Yool et al. 2007; Mdutyana et al. 2020). We interpret our rate data in the context of coincident measurements of regional hydrography, macronutrient concentrations and ratios, and phytoplankton community composition.

2. Methods

2.1. Field collections

Sampling was conducted in the January/February 2019 during the Weddell Sea Expedition onboard the R/V *SA Agulhas II* (Dowdeswell et al., 2019). A total of 19 stations were sampled across the Weddell Sea and are categorised based on their geographic position as Antarctic Peninsula (AP), Larsen C Ice Shelf (LCIS), Weddell Gyre (WG), or Fimbul Ice Shelf (FIS) stations (Table 1; Figure 1). Hydrographic data were collected using a Seabird conductivity-temperature-depth (CTD) profiler equipped with a photosynthetically active radiation (PAR) sensor. Density (sigma-theta; σ_θ) was derived from CTD measurements of temperature, salinity, and pressure, and was used to identify the water mass distributions. The mixed layer depth (MLD) was determined as the depth at which the Brunt-Väisälä frequency squared (N^2 ; a function of σ_θ) reached a maximum (Schofield et al. 2015).

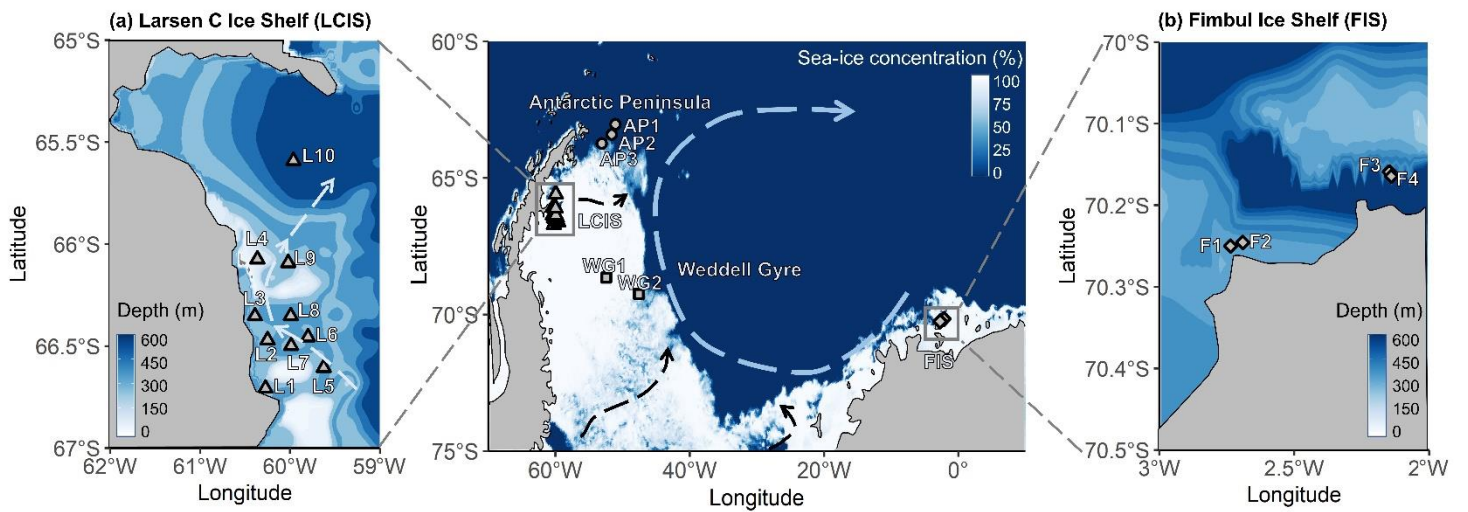


Figure 1. Maps of the Weddell Sea, Larsen C Ice Shelf (LCIS; insert a) and Fimbul Ice Shelf (FIS; insert b) showing the position of the stations where rate experiments were conducted during the Weddell Sea Expedition in January/February 2019. The symbols represent the different regions of the Weddell Sea sampled during the expedition (circle – Antarctic Peninsula (AP); diamond – FIS; triangle – LCIS; square – Weddell Gyre (WG)). The general cyclonic circulation of the Weddell Gyre (dashed blue arrow) is illustrated on the central map, with the dashed black arrows indicating the input of modified water masses from Filchner-Ronne Ice shelf (FRIS) and LCIS (Gordon et al. 1993; Schröder et al. 2002; Schodlok et al. 2002). The hypothesized circulation at LCIS (Nicholls et al. 2004; Hutchinson et al. 2020) is shown by the dashed light-blue arrow in insert (a). The 3.125 km sea-ice concentration data from 31 January 2020 shown in the central panel were taken from <ftp://ftp-projects.cen.uni-hamburg.de/seaice/AMSR2/3.125km> and the bathymetry data (inserts a and b) were taken from ETOPO1 (NOAA National Geophysical Data Center 2009).

Seawater was collected from discrete depths using a rosette of twenty-four 12 L Niskin bottles. At each station, seawater samples for nutrient analysis were collected throughout the water column (typically at 15 discrete depths), while samples for phytoplankton taxonomy and rate experiments were taken from 3–6 depths (see below) that were selected based on profiles of temperature, chlorophyll-a fluorescence, and PAR measured during the CTD down-casts.

Simulated *in situ* experiments were conducted to determine the rates of net primary production (NPP), N uptake (as nitrate (NO_3^-), ammonium (NH_4^+), and urea-N), and nitrite (NO_2^-) oxidation (a measure of nitrification). For NPP and N uptake, seawater was collected from three depths coinciding with the 55%, 10%, and 1% PAR levels, then pre-screened through 200 μm mesh to remove large grazers and transferred to six 1 L and six 2 L polycarbonate bottles per depth. ^{15}N -labeled NO_3^- , NH_4^+ , or urea-N was added to four of the twelve bottles (i.e., two 1 L and two 2 L bottles per N species) and $\text{NaH}^{13}\text{CO}_3$ was added to the bottles amended with $^{15}\text{N}\text{-NH}_4^+$. The tracers were added at ~5–10% of the assumed ambient concentrations, yielding final concentrations in each bottle of approximately 100 μM $\text{NaH}^{13}\text{CO}_3$, 1 μM $^{15}\text{N}\text{-NO}_3^-$, 0.05 μM $^{15}\text{N}\text{-NH}_4^+$, and 0.1 μM $^{15}\text{N}\text{-urea-N}$. Bottles were incubated on the deck for 4–6 hours in a custom-built incubator that was cooled with running surface (~7 m) seawater and equipped with neutral density filters to simulate the relevant light levels. Experiments were terminated via filtration onto 0.3 μm combusted (450°C for 8 hours) glass fibre filters (Sterlitech GF-75) that were stored frozen in combusted (500°C for 5 hours) foil envelopes at -80°C pending analysis.

Seawater samples for the NO_2^- oxidation experiments were collected from the 55%, 10%, and 1% light levels, just below the MLD, and at 200 m and 500 m. From each depth, seawater was transferred into duplicate 250 mL opaque high-density polyethylene (HDPE) bottles to which $^{15}\text{N-NO}_2^-$ was added to achieve a final tracer concentration of 0.1 μM . An initial 50 mL subsample (T_{initial}) was collected from each HDPE bottle immediately following tracer addition and frozen at -20°C until analysis ashore. The 55%, 10%, 1%, and MLD sample bottles were incubated in the on-deck incubator for 20-30 hours while the 200 m and 500 m samples were incubated in a $\sim 2^\circ\text{C}$ cold room. The experiments were terminated by collection and freezing of 50 mL T_{final} subsamples.

2.2. Nutrients

2.2.1. Nutrient concentration analysis

$\text{NO}_3^- + \text{NO}_2^-$ and silicic acid (Si(OH)_4) concentrations were measured using a Lachat QuickChem flow injection analysis platform following published auto-analysis protocols (Diamond, 1994; Grasshoff, 1976) in a configuration with a detection limit of 0.5 μM . Duplicate samples were measured for $\text{NO}_3^- + \text{NO}_2^-$ and Si(OH)_4 on different days, and the standard deviation for duplicates was $\leq 0.5 \mu\text{M}$, with a lower standard deviation for lower-concentration samples. NO_3^- concentrations were determined by subtraction of NO_2^- from $\text{NO}_3^- + \text{NO}_2^-$. Concentrations of phosphate (PO_4^{3-}) and NO_2^- were measured shipboard by standard benchtop colourimetric methods (Strickland and Parsons 1968; Bendschneider et al. 2020; Parsons et al. 1984) using a Thermo Scientific Genesis 30 Visible spectrophotometer. The detection limit was 0.05 μM and the standard deviation for duplicate samples was $\leq 0.05 \mu\text{M}$. Aliquots of a certified reference material (JAMSTEC; Lot CG) were analysed during autoanalyzer and manual runs to ensure measurement accuracy.

NH_4^+ concentrations were measured shipboard following the fluorometric method of Holmes et al. (1999) using a Turner Designs Trilogy fluorometer equipped with a UV module. The detection limit was $< 0.05 \mu\text{M}$ and the standard deviation for duplicate samples was $\leq 0.05 \mu\text{M}$. The matrix effect (ME) that results from the calibration of seawater samples with Milli-Q water standards was calculated using the standard addition method (Saxberg and Kowalski, 1979). All samples were corrected for the ME (Taylor et al., 2007), which was always $< 10\%$ and typically $\leq 5\%$. Urea-N concentrations were measured via the colourimetric method of Revilla et al. (2005) using a Thermo Scientific Genesis 30 Visible spectrophotometer equipped with either a 1 cm- or 5 cm-pathlength cell. The detection limit was 0.05 μM and the standard deviation for duplicate samples was $\leq 0.05 \mu\text{M}$. Hereafter, we use “urea” when referring to urea-N.

2.2.2. Estimating nutrient depletion

The net decrease in euphotic zone nutrient concentrations following nutrient recharge in winter (i.e., the extent of nutrient depletion due to consumption by phytoplankton), between the start of the growing season until the time of our sampling, can be estimated for each station as:

$$X_{\text{depletion}} = [X]_{\text{source}} - [X]_{\text{measured}} \quad (1)$$

where $[X]_{\text{source}}$ is the average $[\text{NO}_3^-]$, $[\text{Si}(\text{OH})_4]$ or $[\text{PO}_4^{3-}]$ in winter water (WW; a shallow temperature minimum layer underlying ASW that is the remnant of the winter mixed layer and considered representative of pre-bloom surface conditions) and $[X]_{\text{measured}}$ is the measured summertime nutrient concentration (Le Corre and Minas 1983; Jennings et al. 1984; Goeyens et al. 1995; Hoppema et al. 2007).

Seasonal melting of sea-ice in the Weddell Sea introduces low-salinity, low-nutrient waters that dilute the biogeochemistry of the mixed layer (Eicken, 1993), potentially leading to an overestimation of phytoplankton-driven nutrient depletion. We correct for the depletion in the surface $[\text{NO}_3^-]$, $[\text{Si}(\text{OH})_4]$ or $[\text{PO}_4^{3-}]$ due to sea-ice melt (i.e., the dilution effect) as:

$$X \text{ depletion}_{(\text{corrected})} = X \text{ depletion} - X \text{ depletion}_{(\text{melt water})} \quad (2a)$$

where $X \text{ depletion}_{(\text{melt water})}$ is the decrease in surface $[\text{NO}_3^-]$, $[\text{Si}(\text{OH})_4]$ or $[\text{PO}_4^{3-}]$ due to sea-ice melt, calculated as:

$$X \text{ depletion}_{(\text{melt water})} = [X]_{\text{sea-ice}} (f_{\text{sea-ice}}) + [X]_{\text{source}} (1 - f_{\text{sea-ice}}) \quad (2b)$$

Here, the nutrient concentrations in summertime sea-ice ($[X]_{\text{sea-ice}}$) are assumed to be: $[\text{NO}_3^-]_{\text{sea-ice}} = 1 \mu\text{M}$, $[\text{Si}(\text{OH})_4]_{\text{sea-ice}} = 5 \mu\text{M}$, and $[\text{PO}_4^{3-}]_{\text{sea-ice}} = 0.3 \mu\text{M}$ (Fripiat et al., 2014, 2017), and:

$$f_{\text{sea-ice}} = \frac{\text{salinity}_{\text{measured}} - \text{salinity}_{\text{source}}}{\text{salinity}_{\text{sea-ice}} - \text{salinity}_{\text{source}}} \quad (2c)$$

with $\text{salinity}_{\text{sea-ice}}$ taken to be 5 based on sea-ice salinity measurements made during the cruise (Dowdeswell et al., 2019) and $\text{salinity}_{\text{source}}$ set to 34.2 at FIS and 34.4 at the other stations (the salinity of WW; Figure 2g). On average, correcting for sea-ice melt changed the estimates of X depletion by $0.4 \pm 0.9\%$. Hereafter, all references to nutrient depletion are to the computed values of $X \text{ depletion}_{(\text{corrected})}$. The approach above for calculating $X \text{ depletion}_{(\text{corrected})}$ assumes, following correction for sea-ice melt, that nutrient drawdown is due to phytoplankton assimilation only, a reasonable assumption in the Weddell Sea in summer.

2.3. Uptake rates

Incubation filters were oven-dried for 24 hours at 40°C , then folded into tin cups. Samples were analysed using a Flash Elemental Analyser 1112 Series coupled to a Delta V Plus isotope ratio mass spectrometer (IRMS) in a configuration with a detection limit of $2 \mu\text{g C}$ and $1 \mu\text{g N}$. Blanks (combusted unused filters + tin cups) and laboratory running standards, calibrated to certified IAEA reference materials, were run after every five samples.

The specific rates of carbon fixation (V_C) and NO_3^- , NH_4^+ and urea uptake ($V_{\text{NO}_3^-}$, $V_{\text{NH}_4^+}$, V_{urea} ; d^{-1}) were calculated according to equation 2 in Dugdale and Wilkerson (1986). NPP and the absolute rates of NO_3^- , NH_4^+ and urea uptake (ρNO_3^- , ρNH_4^+ and ρurea ; $\mu\text{M d}^{-1}$) were then determined by multiplying V_C by the concentration of particulate organic carbon ([POC]) and $V_{\text{NO}_3^-}$, $V_{\text{NH}_4^+}$ and V_{urea} by the concentration of particulate organic nitrogen ([PON]) (Dugdale and Wilkerson 1986; equation 3).

2.4. NO_2^- oxidation rates

The T_{initial} and T_{final} samples from the NO_2^- oxidation incubations were measured for the $\delta^{15}\text{N}$ of NO_3^- ($\delta^{15}\text{N}_{\text{NO}_3}$; where $\delta^{15}\text{N} = ((^{15}\text{N}_{\text{sample}}/^{14}\text{N}_{\text{sample}})/(^{15}\text{N}_{\text{standard}}/^{14}\text{N}_{\text{standard}}) - 1) \times 1000$) using the denitrifier method (Sigman et al. 2001; McIlvin and Casciotti 2011). Prior to isotopic analysis, all samples were treated with sulfamic acid to remove NO_2^- as the denitrifier method converts both NO_2^- and NO_3^- to N_2O gas (Granger and Sigman, 2009); the difference in $\delta^{15}\text{N}_{\text{NO}_3}$ between the T_{final} and T_{initial} samples was then taken as the $^{15}\text{NO}_3^-$ enrichment due to $^{15}\text{NO}_2^-$ oxidation (Peng et al. 2015). Results were referenced to atmospheric N_2 using certified reference materials (IAEA-NO-3, USGS-34, and USGS-32; Gonfiantini 1984; Böhlke and Coplen 1995; Böhlke et al. 2003). The rate of NO_2^- oxidation ($V_{\text{NO}_2^-}$; nM d^{-1}) was calculated following Peng et al. (2015) as:

$$V_{\text{NO}_2^-} = \frac{\Delta[^{15}\text{NO}_3^-]}{f_{\text{NO}_2^-}^{15} \times t} \quad (3)$$

where $\Delta[^{15}\text{NO}_3^-]$ is the difference in the concentration of $^{15}\text{NO}_3^-$ between the end and the start of the experiment (i.e., $T_{\text{final}} - T_{\text{initial}}$) due to NO_2^- oxidation, $f_{\text{NO}_2^-}^{15}$ is the fraction of $^{15}\text{NO}_2^-$ at the start of the incubation, and t is the length of the incubation (days). The detection limit for $V_{\text{NO}_2^-}$ ranged from 0.06-0.46 nM d^{-1} (calculated following Santoro et al. 2013). We take $V_{\text{NO}_2^-}$ as a measure of the nitrification rate given that NO_2^- oxidation is the step in the nitrification pathway that produces NO_3^- .

To determine relative carbon export potential at each station, we calculated the f -ratio (a measure of new production relative to total (i.e., new+regenerated) production) using the absolute N uptake and NO_2^- oxidation rates and a modified version of the Eppley and Peterson (1979) equation:

$$f\text{-ratio}_{(\text{excluding urea})} = \frac{\rho\text{NO}_3^- - V_{\text{NO}_2^-}}{\rho\text{NO}_3^- + \rho\text{NH}_4^+} \quad (4a)$$

$$f\text{-ratio}_{(\text{including urea})} = \frac{\rho\text{NO}_3^- - V_{\text{NO}_2^-}}{\rho\text{NO}_3^- + \rho\text{NH}_4^+ + \rho\text{urea}} \quad (4b)$$

Equation 4a and b account for euphotic zone nitrification (Mdutyana et al. 2020), which yields regenerated rather than new NO_3^- that is then available for phytoplankton to consume. Not accounting for $V_{\text{NO}_2^-}$ could result in the f -ratio being overestimated (Yool et al. 2007). Equation 4b accounts for urea uptake, that was either measured (at the LCIS stations and WG1) or calculated (at the AP, FIS and WG2) (see section 3.3.4 below).

2.5. Phytoplankton taxonomy and carbon biomass

At all stations, microphytoplankton samples were collected between the surface and 30 m using a HYDROBIOS conical plankton net ($r = 12.5$ cm; $h = 50$ cm) with a mesh size of 55 μm . Samples were transferred to 50 mL centrifuge tubes, fixed with 10 μL of 25% glutaraldehyde, and stored at room temperature in the dark until later analysis via light and scanning electron microscopy. Additionally, samples for flow cytometry were collected in

50 mL centrifuge tubes from Niskin bottles fired at the 55%, 10%, and 1% PAR depths. These samples were fixed with 10 μ L of 25% glutaraldehyde and stored in the dark at 4°C until analysis.

Onshore, each preserved net-sample was homogenized, and one drop (40 μ L) was wet mounted on a slide. All the cells on the slide with intact chloroplasts (i.e., alive at the time of sampling) were counted at 400x or 630x magnification using a Zeiss AxioScope A1 light microscope (LM). The number of cells mL^{-1} was calculated as:

$$\text{cells mL}^{-1} = \left[A \left(\frac{1}{\text{mL}} \right) \left(\frac{n}{V} \right) \right] \quad (5)$$

where A is the number of cells per drop, mL is the volume of water sampled (1470000 mL; computed using the volume of a cylinder, $\pi r^2 h$, where $r = 125$ mm and $h = 30000$ mm depth), n is the total volume of concentrated sample, and V is the volume of 1 drop of concentration sample.

An aliquot of 5 mL from each preserved sample was cleaned by removing carbonate particles and organic matter using 10% hydrochloric acid and 37% hydrogen peroxide, respectively. After thorough rinsing with distilled water, permanent slides were prepared by pipetting the cleaned material onto acid-washed coverslips, air drying them overnight, and mounting the cover slips onto glass slides using Naphrax® mountant (refractive index = 1.7). The permanent slides were examined using a Zeiss AxioScope A1 LM equipped with differential interference contrast at 1000x magnification (under oil immersion) for identification of the diatom cells to the lowest taxonomic classification possible. Stubs were also prepared from the cleaned material for Scanning Electron Microscopy (SEM), with a JEOL JSM 7001F field emission SEM used to visualize the morphological features not evident under LM.

The average size (μm) and carbon content (pg C cell^{-1}) of each identified diatom species was taken from Leblanc et al. (2012) for high latitude locations (50 – 70°S) (Table S1), and the carbon content of colonial *P. antarctica* was estimated as 13.6 pg C cell^{-1} (Mathot et al., 2000) for single cells within a colony. Since the majority of *P. antarctica* were in spherical colony form, the total colony carbon biomass (C_{COL}) was calculated as:

$$C_{\text{COL}} = [13.60 \times N_C] + C_M \quad (6)$$

where N_C is the number of cells counted per litre, C_M is the mucus-related carbon calculated as $C_M = 0.213 \times V_{\text{COL}} + 4.58$, and V_{COL} is the volume of the spherical colony, calculated as $V_{\text{COL}} = 417 \times N_C^{1.67}$ (Mathot et al., 2000).

Flow cytometry samples were analyzed using a BD LSR II SORP flow cytometer with blue/red/green laser configuration. The size-class to which each cell belonged was defined based on its forward scatter area (FSC-A) relative to the FSC-A of 2.8 μm and 20 μm beads (Figure S1a). Once categorized as either picoplankton (<2.8 μm), nanoplankton (2.8-20 μm), or microplankton (>20 μm), the cells were grouped into six populations based on their orange fluorescence (indicative of phycoerythrin; PE) relative to their red fluorescence (indicative of chlorophyll-a; chl-a): two *Synechococcus* populations (Syn 1 and Syn 2), one picoeukaryote population (PicoEuk),

two nanoeukaryote populations (NanoEuk 1 and NanoEuk 2), and one microeukaryote population (MicroEuk; see section S2 in the Supplemental Information for details of population identification). The biovolumes of the eukaryotic populations were estimated based on their FSC-A relative to that of six beads of known size and volume (Figure S1c; Table S2). *Synechococcus* had an unrealistically high measured FSC-A, which is an artefact of the high ratio of photosystem I to photosystem II of the group compared to the other phytoplankton populations. This elevates electron chain activity, leading to an increase in the emission spectrum and low excitation of the *Synechococcus* populations (Kaprelyants and Kell 1993; Sunda and Huntsman 2015). The biovolume of *Synechococcus* was thus assumed to be $1 \mu\text{m}^3$ (Kana and Glibert, 1987; Paulsen et al., 2015). Biovolume is used here as a proxy for biomass.

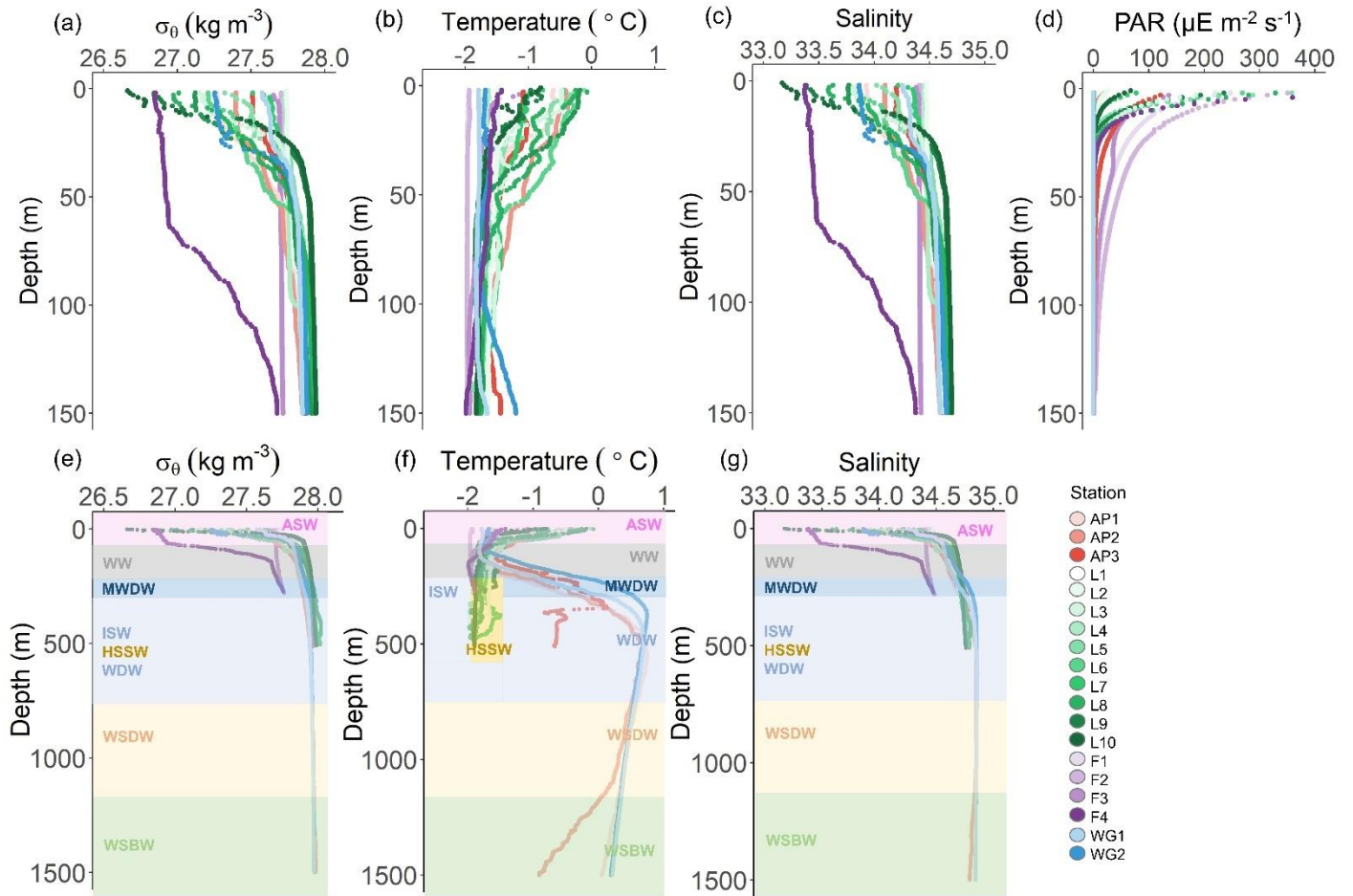
3. Results

3.1. Water column hydrography

Throughout the study region, relatively cool and fresh (-2 to 0°C and 33.0 to 34.5) ASW occurred between the surface and 135 m (Figure 2). Through this layer and down to 200 m, salinity increased with depth while temperature decreased, reaching a local minimum (-1.6°C) at ~ 100 m. These hydrographic changes are characteristic of WW, which is considered a summertime record of winter conditions and a reflection of the initial state from which the mixed layer evolves over the spring/summer growing season (Altabet and Francois, 2001). Below WW at the AP and WG stations, salinity remained constant while temperature increased with depth, reaching a local maximum (0.5°C) at 500 m and 300 m for the AP and WG, respectively. This feature is characteristic of Warm Deep Water (WDW), a temperature maximum layer that is a modified form of Circumpolar Deep Water (CDW) (Muench and Gordon, 1995; Fahrbach et al., 1995). Below WW at the LCIS and FIS stations, salinity increased, and temperature decreased with depth, reaching a local salinity maximum (34.6 at LCIS and 34.3 at FIS) and temperature minimum ($\leq -1.8^\circ\text{C}$). The increase in salinity is characteristic of High Salinity Shelf Water (HSSW) produced by brine rejection during sea-ice formation, while the decrease in temperature is indicative of Ice Shelf Water (ISW) produced by the supercooling of ASW under the ice shelves (Fahrbach et al. 1995; Nicholls et al. 2009; Hutchinson et al. 2020). The densities of WW, WDW, HSSW, and ISW are contiguous, with the mixed product of these waters termed Modified Warm Deep Water (MWDW) (Fahrbach et al., 1995). Below WDW at the AP and WG stations, temperature decreased due to the presence of Weddell Sea Deep Water (WSDW; temperature range of -0.7 to 0°C) and Weddell Sea Bottom Water (WSBW; temperature $\leq -0.7^\circ\text{C}$) (Fahrbach et al., 1995; Muench and Gordon, 1995).

Variability in the density of ASW was observed among the stations (Figure 2a). The surface density profiles at the AP, WG, and early-summer FIS stations were very similar, while the late-summer density profile at FIS revealed lower-density waters in the upper 100 m. At LCIS, the surface density profiles were highly variable, and no consistent pattern was observed, although the most northern stations (L9 and L10; Figure 1) were characterised by the lowest densities. Stations L1 and L3, situated closest to the ice shelf, were characterised by the highest densities, contiguous with the underlying WW layer.

383 The MLD appeared most strongly controlled by salinity at all stations and was always shallower than the depth
 384 of the euphotic zone (Z_{eu} ; Table 1; Figure 2a-d), the latter defined as the depth to which 1% of surface PAR
 385 penetrated (Kirk 1994). The deepest MLD and Z_{eu} were observed at FIS in early summer (average MLD of 103.0
 386 ± 36.6 m and Z_{eu} of 91.7 ± 14.4 m; $n = 3$), while the shallowest MLD and Z_{eu} were observed at LCIS (average
 387 MLD of 13.9 ± 5.9 m and Z_{eu} of 28.5 ± 9.1 m; $n = 10$) (Figure 2d; Table 1). The rates of NPP, N uptake and
 388 nitrification were therefore trapezoidally-integrated to Z_{eu} rather than to the MLD since we assume that
 389 phytoplankton were active at least to the depth of 1% PAR.



390 **Figure 2.** Depth profiles of (a) potential density (σ_θ), (b) potential temperature, (c) absolute salinity, and (d)
 391 photosynthetically active radiation (PAR) in the upper 150 m and (e) σ_θ , (f) potential temperature, and (g) absolute
 392 salinity in the upper 1500 m at all stations. The water masses present at each station, identified by their temperature
 393 and salinity characteristics, are denoted in panels (e-g) as follows: WSBW – Weddell Sea Bottom Water, WSDW
 394 – Weddell Sea Deep Water, WDW – Warm Deep Water, MWDW – Modified Warm Deep Water, ISW – Ice
 395 Shelf Water, HSSW – High Salinity Shelf Water, WW – Winter Water, ASW – Antarctic Surface Water. In panel
 396 (f), the dark yellow rectangle indicates HSSW. The general station locations are indicated by the different marker
 397 colours: red shades – Antarctic Peninsula, green shades – Larsen C Ice Shelf, blue shade – Weddell Gyre, light
 398 purple shades – early summer Fimbul Ice Shelf, and dark purple – late summer Fimbul Ice Shelf.

400 3.2. Nutrient concentrations

401 The concentrations of the regenerated N forms (i.e., NH_4^+ and urea) were generally low in the surface and
 402 increased with depth to reach a maximum in the shallow subsurface (Figure 3a and b). A sharp maximum in the
 403 NH_4^+ concentration was observed near Z_{eu} at all stations, indicative of the depth of maximum net remineralisation.
 404 Urea concentrations were more variable, likely due to variability in the processes that produce this N form (e.g.,

bacterial excretion; Berges and Mulholland 2008). The highest average concentrations of regenerated N in the euphotic zone were observed at LCIS and FIS in late summer ($0.62 \pm 0.30 \mu\text{M}$ for NH_4^+ and $0.21 \pm 0.07 \mu\text{M}$ for urea), while the lowest concentrations were observed at FIS in early summer (below detection for both NH_4^+ and urea). Elevated regenerated N concentrations were also observed at the AP stations (euphotic zone average of $0.8 \pm 0.3 \mu\text{M}$ for NH_4^+ and $0.2 \pm 0.06 \mu\text{M}$ for urea), while low concentrations were observed at the WG stations (euphotic zone average of $0.3 \pm 0.1 \mu\text{M}$ for NH_4^+ and $0.1 \pm 0.0 \mu\text{M}$ for urea).

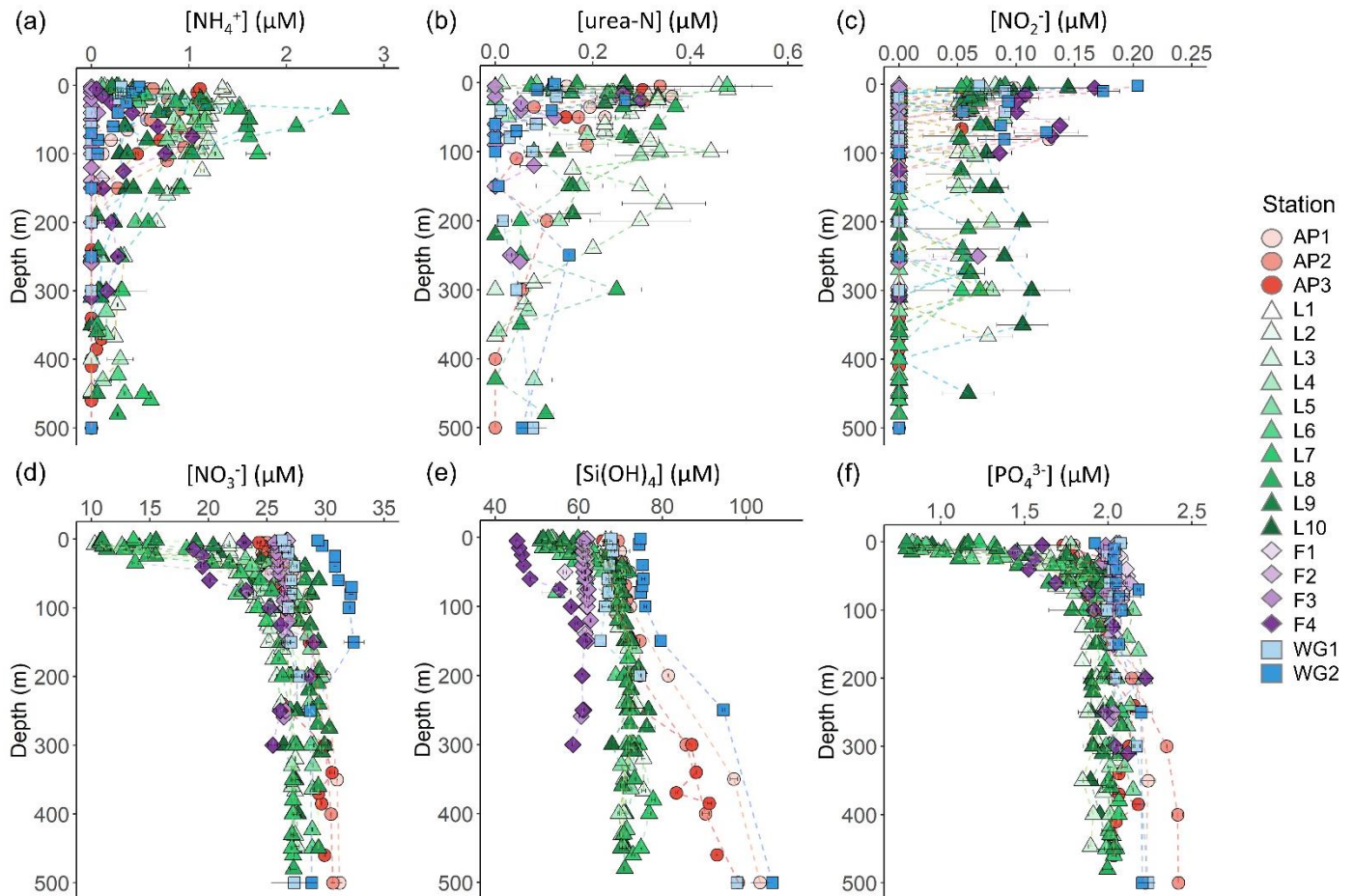


Figure 3. Depth profiles (0-500 m) of (a) NH_4^+ , (b) urea-N, (c) NO_2^- , (d) NO_3^- , (e) Si(OH)_4 , and (f) PO_4^{3-} concentrations. For all panels, the error bars represent ± 1 SD of replicate samples ($n = 2-3$). For NO_3^- , which was calculated as $\text{NO}_3^- + \text{NO}_2^- - \text{NO}_2^-$, error has been propagated according to standard statistical practices. Note that the x-axis scales in panels (d-f) do not start at zero.

The concentrations of NO_2^- were generally low throughout the euphotic zone, and decreased to below detection by 120 m at the FIS, AP, and WG stations (with the exception of a single sample from the early-summer FIS), and by 500 m at LCIS (Figure 3c). A high degree of variability was observed, with the highest surface-layer NO_2^- concentrations occurring in the WG and at FIS in late summer (average euphotic zone NO_2^- concentrations of $0.08 \pm 0.06 \mu\text{M}$ and $0.12 \pm 0.03 \mu\text{M}$, respectively).

The euphotic zone concentrations of NO_3^- , Si(OH)_4 and PO_4^{3-} decreased towards the surface due to assimilation by phytoplankton (Figure 3d-f). The lowest surface concentrations of NO_3^- and PO_4^{3-} were observed at LCIS (16.6

$\pm 3.8 \mu\text{M}$ and $1.3 \pm 0.4 \mu\text{M}$, respectively) and of Si(OH)_4 was observed at FIS in late summer ($46.1 \pm 0.8 \mu\text{M}$). The highest surface concentrations of NO_3^- , PO_4^{3-} and Si(OH)_4 occurred in the WG ($28.8 \pm 2.4 \mu\text{M}$, $2.0 \pm 0.54 \mu\text{M}$, and $70.1 \pm 3.8 \mu\text{M}$, respectively). Elevated Si(OH)_4 and PO_4^{3-} concentrations were observed between 200 and 500 m at the AP and WG stations due to the presence of WDW at these stations versus shelf waters (i.e., ISW and HSSW) at LCIS and FIS. The depth of maximum remineralisation in the open Weddell Sea is 300-500 m, the depth range occupied by WDW (Vernet et al. 2019, and references therein). The high rates of remineralisation, and therefore nutrient accumulation, in WDW account for the elevated nutrient concentrations observed in WDW relative to the shelf water masses (Whitworth and Nowlin, 1987). Estimates of NO_3^- , Si(OH)_4 , and PO_4^{3-} depletion (i.e., $X \text{ depletion}_{(\text{corrected})}$; equation 2) were highest at LCIS (average NO_3^- depletion of $8.3 \pm 3.9 \mu\text{M}$, Si(OH)_4 depletion of $8.3 \pm 4.0 \mu\text{M}$, and PO_4^{3-} depletion of $0.6 \pm 0.3 \mu\text{M}$), while the lowest nutrient depletions occurred in early summer at FIS (average NO_3^- depletion of $0.3 \pm 0.3 \mu\text{M}$, Si(OH)_4 depletion of $0.6 \pm 0.6 \mu\text{M}$, and PO_4^{3-} depletion of $0.00 \pm 0.02 \mu\text{M}$) (Figure 4a-c; Table 1).

Variations in the depletion ratios of $\text{Si(OH)}_4:\text{NO}_3^-$ and $\text{NO}_3^-:\text{PO}_4^{3-}$ can be used as indicators of the nutrient status of the phytoplankton community, particularly diatoms. Under iron-replete conditions, diatoms have been observed to consume Si(OH)_4 and NO_3^- in a ratio of $\sim 1:1$, and NO_3^- and PO_4^{3-} in a ratio of $\sim 14:1$ (Hutchins and Bruland, 1998; Takeda, 1998; Ragueneau et al., 2000; Mosseri et al., 2008), while under conditions of limitation, the ratio of $\text{Si(OH)}_4:\text{NO}_3^-$ uptake rises (to $>2:1$) and $\text{NO}_3^-:\text{PO}_4^{3-}$ uptake decreases (to as low as $10:1$) (Arrigo et al., 1999; Franck et al., 2000; Brzezinski et al., 2003; Green and Sambrotto, 2006; Mosseri et al., 2008; Weber and Deutsch, 2010a; Martiny et al., 2013). Additionally, the dominance of one phytoplankton species over another may cause deviations in the $\text{NO}_3^-:\text{PO}_4^{3-}$ depletion ratio. For example, in regions dominated by *P. antarctica*, Arrigo et al. (1999) observed a $\text{NO}_3^-:\text{PO}_4^{3-}$ depletion ratio of $\sim 20:1$, while in areas dominated by iron-deplete diatoms, this ratio was $\sim 10:1$. The $\text{NO}_3^-:\text{PO}_4^{3-}$ depletion ratios can thus also yield insights into the dominant phytoplankton species active in the upper water column. In our study, the average euphotic zone $\text{Si(OH)}_4:\text{NO}_3^-$ depletion ratios ranged from 0.5 to 6.1 (Table 1), with the highest ratios estimated for the WG stations (average of 5.4 ± 5.5) and at FIS in late summer (average of 2.3 ± 0.5). The euphotic zone average $\text{NO}_3^-:\text{PO}_4^{3-}$ depletion ratios were more variable, ranging from 3.7 ± 1.5 to 48.6 ± 11.5 , with the lowest ratios computed for the WG stations (average of 4.1 ± 1.5) and the highest for FIS in early summer (average of 33.7 ± 3.6). In the latter case, the degree of Si(OH)_4 and PO_4^{3-} depletion was extremely low (Table 1), which likely accounts for the variable and anomalous $\text{Si(OH)}_4:\text{NO}_3^-$ and $\text{NO}_3^-:\text{PO}_4^{3-}$ depletion ratios computed for stations F1-F3.

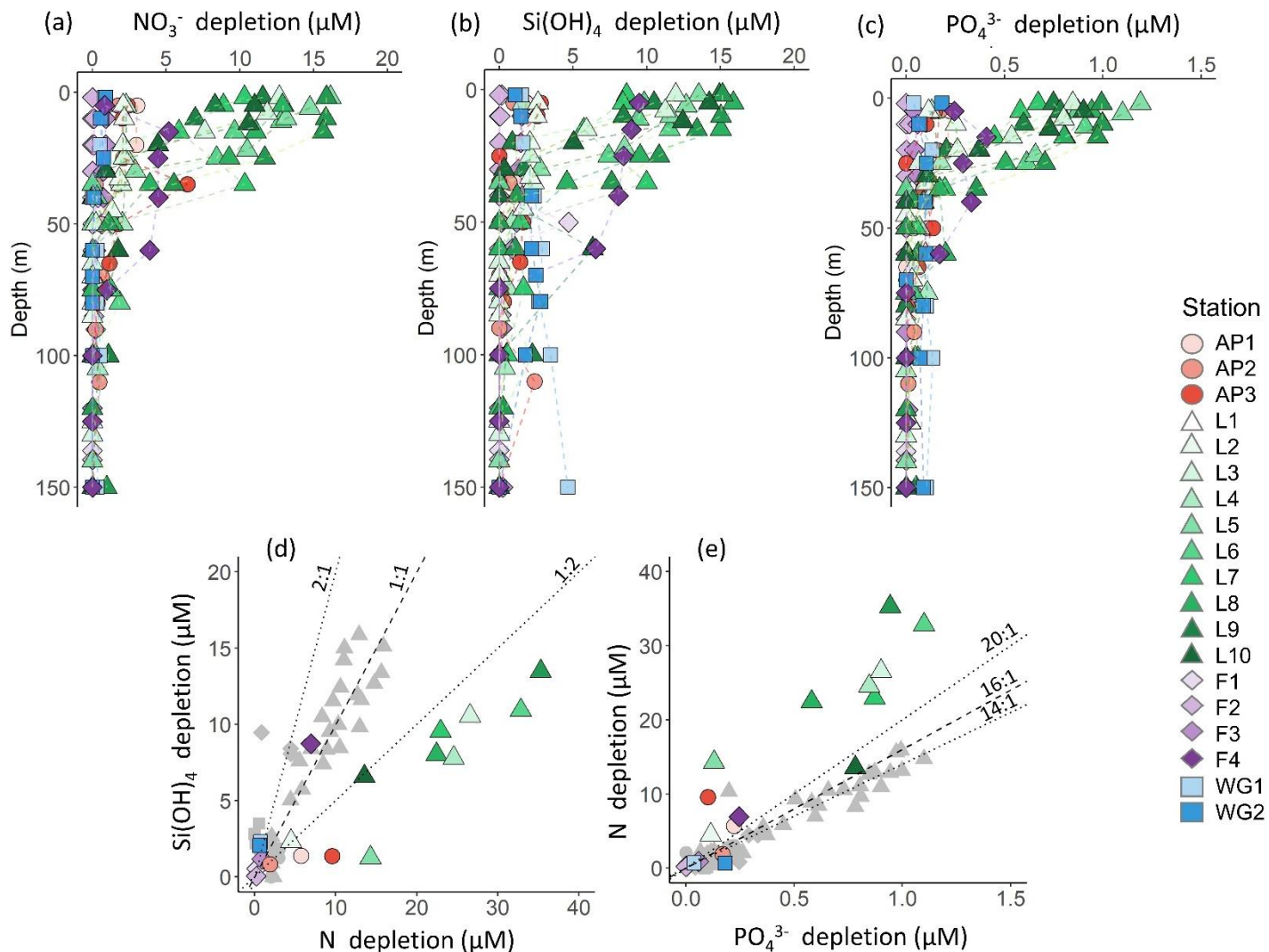


Figure 4. Depth profiles (0-150 m) of (a) NO_3^- depletion, (b) Si(OH)_4 depletion, and (c) PO_4^{3-} depletion at each station. Also shown are scatterplots of (d) Si(OH)_4 depletion versus total N depletion (coloured symbols; see text for details) and (e) PO_4^{3-} depletion versus total N depletion (coloured symbols) and PO_4^{3-} depletion versus NO_3^- depletion (grey symbols) at each station. The dashed line in panel (d) represents the 1:1 Si:N depletion ratio, expected for iron-replete diatoms (Ragueneau et al. 2000; Hutchins and Bruland 1998; Takeda 1998; Mosseri et al. 2008), while the dotted lines represent the 2:1 Si:N ratio, expected for iron-limited diatoms (Arrigo et al., 1999; Franck et al., 2000; Brzezinski et al., 2003; Green and Sambrotto, 2006; Mosseri et al., 2008; Weber and Deutsch, 2010; Martiny et al., 2013), and the 1:2 Si:N ratio, indicative of enhanced activity of non-siliceous phytoplankton. The dashed line in panel (e) represents the 16:1 N:P depletion ratio (the Redfield ratio), while the dotted lines represent the 20:1 N:P ratio, expected for *P. antarctica*, and the 14:1 N:P ratio, expected for iron-replete diatoms (Hutchins and Bruland 1998; Takeda 1998; Arrigo et al. 1999; Ragueneau et al. 2000; Mosseri et al. 2008).

3.3. Upper ocean biomass, NPP and N uptake rates

3.3.1. Particulate organic carbon and nitrogen

The highest concentrations of POC and PON were observed in the surface at all stations (Figure 5a and b), decreasing towards Z_{eu} (Figure 5g and h). Averaged over the euphotic zone, the lowest POC and PON concentrations occurred in early summer at FIS (4.6 \pm 1.5 μ M and 0.3 \pm 0.1 μ M, respectively) and the highest at LCIS (17.9 \pm 7.3 μ M and 2.5 \pm 0.8 μ M; Table 2). Across the region, the biomass C:N ratio was fairly uniform throughout the euphotic zone, except at stations F1, F2, WG1, and WG2 (Figure 5c, f and i). In general, the FIS and WG stations were characterized by significantly higher C:N ratios than those expected from Redfield stoichiometry (C:N = 6.63:1), averaging 16.5 \pm 8.8 and 12.3 \pm 1.8, respectively. By contrast, at the LCIS stations, the biomass C:N ratios were close to the Redfield ratio (7.4 \pm 1.9), while the AP stations were characterized by slightly higher C:N ratios (8.3 \pm 2.5).

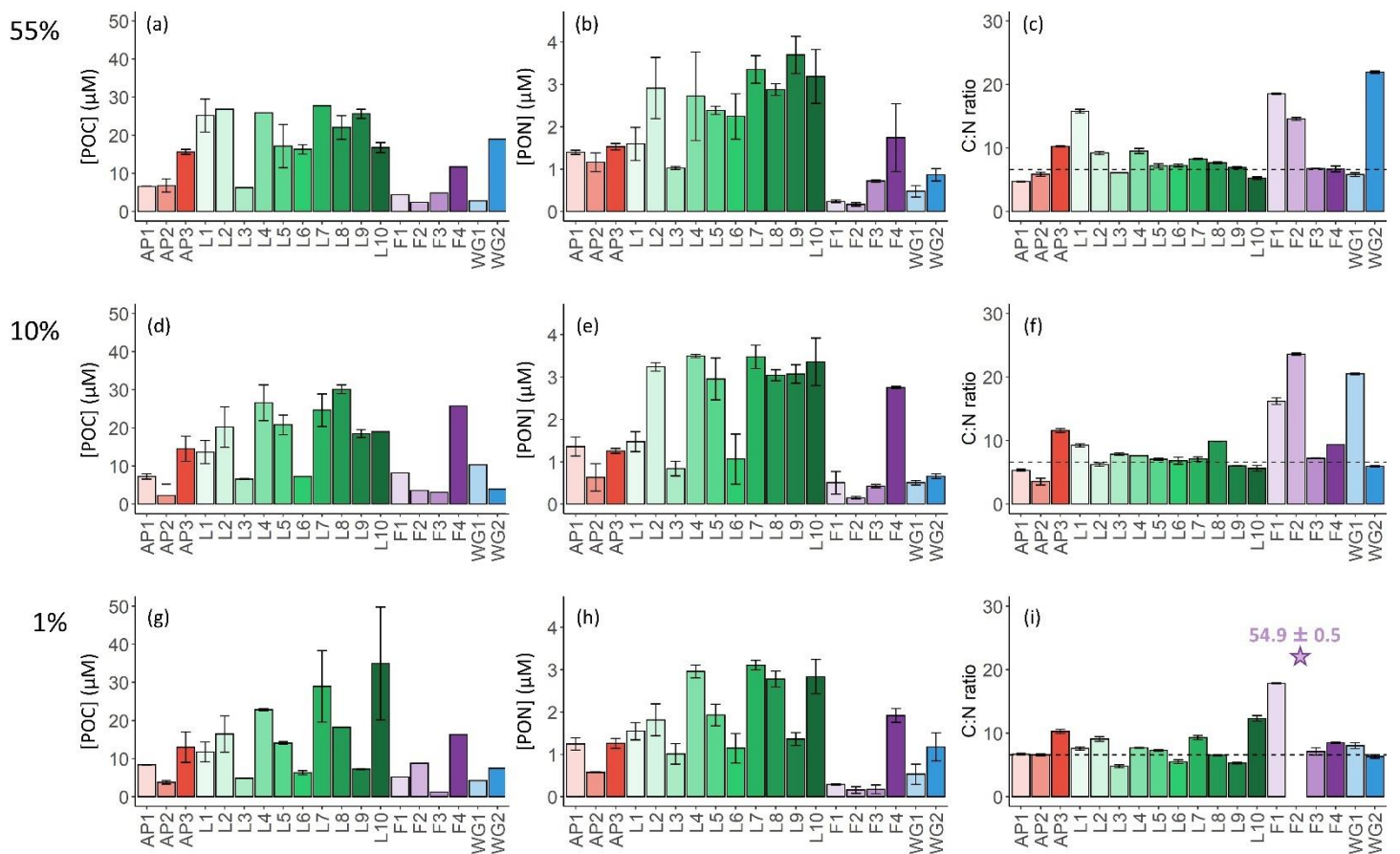


Figure 5. Bar plots of (a, d, g) POC concentrations, (b, e, h) PON concentrations, and (c, f, i) biomass C:N ratios measured at the 55% (a-c), 10% (d-f), and 1% light levels (g-i). The stations are labelled on the x-axis, and the general stations locations are indicated by the different colours: red shades – Antarctic Peninsula, green shades – Larsen C Ice Shelf, blue shade –Weddell Gyre, light purple shades – early summer Fimbul Ice Shelf, and dark purple – late summer Fimbul Ice Shelf. The dotted black horizontal line in panels (c), (f), and (i) shows the Redfield C:N ratio of 6.63. The purple star in panel (i) indicates the anomalously high C:N ratio estimated for the 1% PAR depth at station F2. The error bars represent \pm 1 SD of replicate samples (n = 2-6). Where applicable, the error has been propagated according to standard statistical practices.

3.3.2. Rates of NPP and N uptake

At all stations, NPP was generally highest at the surface (Figure 6a) and decreased towards Z_{eu} (Figure 6i). The highest depth-specific (as opposed to integrated) rates were observed at LCIS (except at station L10 where the

rates were very low), while the lowest rates occurred in early summer at FIS (with particularly low rates measured at station F1; Figure 6a, e and i). At the WG stations and at FIS in late summer, the rates of NPP were comparable to the lower end of the rates observed at LCIS, while NPP along the AP increased shoreward (i.e., the lowest rates were observed at AP1 and the highest at AP3) to values similar to those observed at LCIS. The highest euphotic zone-integrated rates of NPP were observed at AP3 ($65.0 \pm 0.1 \text{ mmol m}^{-2} \text{ d}^{-1}$) and L5 ($61.0 \pm 0.7 \text{ mmol m}^{-2} \text{ d}^{-1}$), while the lowest occurred at L10 ($1.8 \pm 0.04 \text{ mmol m}^{-2} \text{ d}^{-1}$) (Table 2).

As per NPP, the rates of ρNO_3^- decreased towards Z_{eu} at all stations (Figure 6b, f and j), as did the extent of NO_3^- depletion (Figure 4a). The depth-specific rates of ρNO_3^- were highest at LCIS and lowest in early summer at FIS. However, because the euphotic zone was generally shallower at LCIS than at the other stations, the euphotic zone-integrated rates of ρNO_3^- were fairly similar across the study region, with the largest variability observed at LCIS (Table 2). In late summer at FIS, integrated ρNO_3^- was on average higher than at LCIS ($3.9 \pm 0.03 \text{ mmol m}^{-2} \text{ d}^{-1}$ at F4 versus an average of $2.2 \pm 1.1 \text{ mmol m}^{-2} \text{ d}^{-1}$ at LCIS), with depth-specific rates that were double those measured at FIS in early summer. The sea-ice at FIS had completely melted by late summer, which likely contributed to the increase in ρNO_3^- later in the season. The highest euphotic zone-integrated rates of ρNO_3^- were observed at stations F3 and L5 ($4.8 \pm 0.07 \text{ mmol m}^{-2} \text{ d}^{-1}$ and $4.7 \pm 0.04 \text{ mmol m}^{-2} \text{ d}^{-1}$, respectively). At L5, this elevated rate coincided with low euphotic zone NO_3^- concentrations ($12.0 \pm 1.9 \text{ }\mu\text{M}$; Figure 3d) and a high degree of NO_3^- depletion ($10.9 \pm 2.3 \text{ }\mu\text{M}$; Figure 4a). The lowest euphotic zone-integrated rates of ρNO_3^- occurred at station L10 ($0.5 \pm 0.0 \text{ mmol m}^{-2} \text{ d}^{-1}$).

At all stations, rates of ρNH_4^+ increased with depth, reaching a maximum at Z_{eu} (Figure 6c, g and k). The highest depth-specific rates of ρNH_4^+ were observed at LCIS and the lowest at FIS in early summer. Euphotic zone-integrated rates of ρNH_4^+ at the AP stations were comparable to those observed at LCIS (regional average of $3.3 \pm 2.2 \text{ mmol m}^{-2} \text{ d}^{-1}$ and $2.5 \pm 1.3 \text{ mmol m}^{-2} \text{ d}^{-1}$, respectively), while the rates at the WG stations and at FIS in late summer were comparable to the lower end of the LCIS rates (average of $2.0 \pm 0.2 \text{ mmol m}^{-2} \text{ d}^{-1}$ at WG and $1.9 \pm 0.0 \text{ mmol m}^{-2} \text{ d}^{-1}$ at FIS). The early- to late-summer rise in the euphotic zone-integrated rates of ρNH_4^+ at FIS coincided with an increase in the average euphotic zone NH_4^+ concentration from below detection to $0.2 \pm 0.1 \text{ }\mu\text{M}$ (Figure 3a). At the AP, LCIS, and WG stations, the rates of ρNH_4^+ were similar to the coincident rates of ρNO_3^- , while at FIS, ρNH_4^+ was less than half of ρNO_3^- (Table 2). The highest euphotic zone-integrated rates of ρNH_4^+ were observed at station AP3 ($5.8 \pm 0.0 \text{ mmol m}^{-2} \text{ d}^{-1}$), coincident with a high average euphotic zone NH_4^+ concentration ($1.1 \pm 0 \text{ }\mu\text{M}$). The lowest integrated ρNH_4^+ occurred at station F1 ($0.4 \pm 0.0 \text{ mmol m}^{-2} \text{ d}^{-1}$) where the concentration of NH_4^+ in the euphotic zone was below detection.

Rates of purea were only measured at the LCIS stations and WG1 (Figure 6d, h and l; Table 2). A high degree of variability in purea was observed at LCIS, with euphotic zone-integrated rates ranging from 0.2 to $1.1 \text{ mmol m}^{-2} \text{ d}^{-1}$ (average of $0.6 \pm 0.3 \text{ mmol m}^{-2} \text{ d}^{-1}$). This variability appears to be related to the urea concentrations, with the highest rates of purea coinciding with the highest ambient urea concentrations (e.g., station L5), and vice versa (e.g., station L4) (Figure 3b). On average, the rates of purea in the WG were half the rates of ρNH_4^+ , and urea concentrations were low (Figure 3b; Table 2).

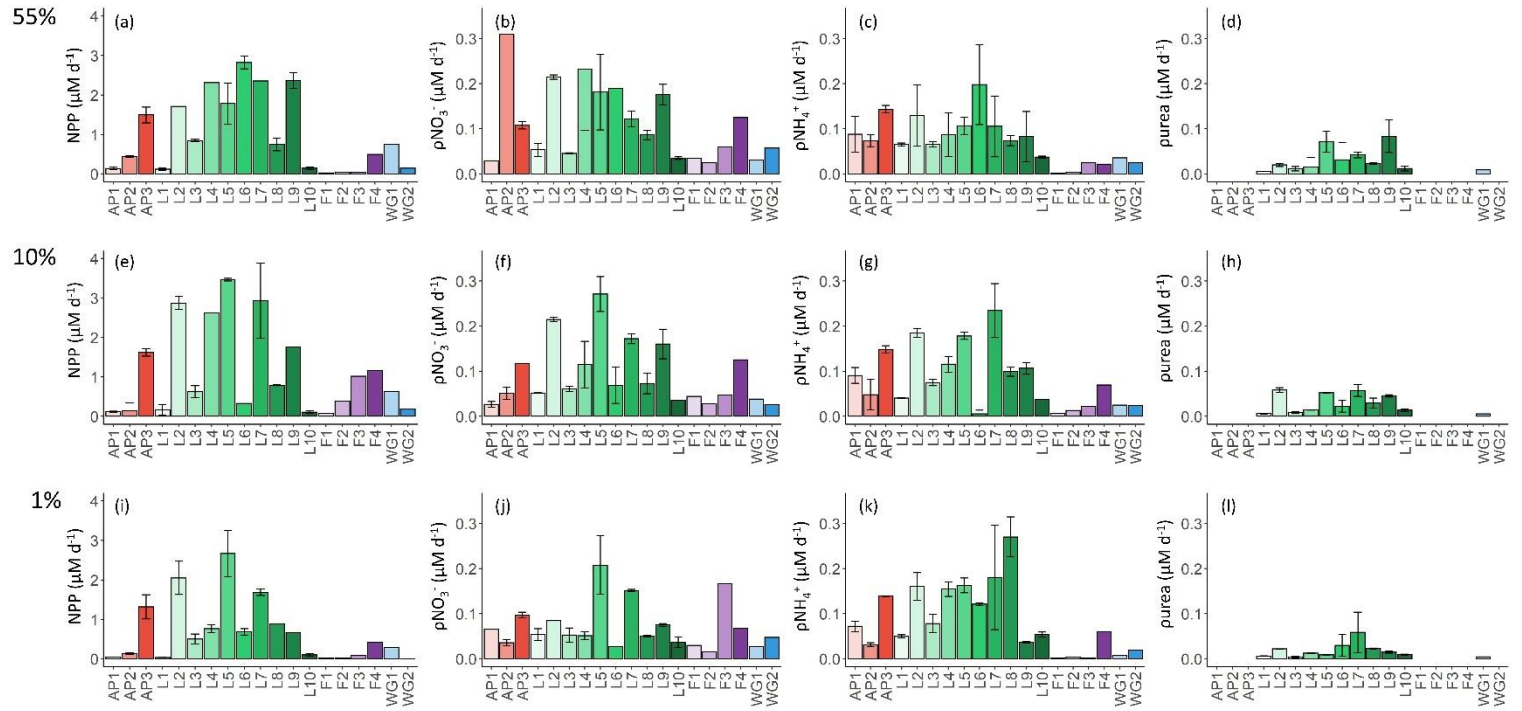


Figure 6. Daily rates of (a, e, i) NPP, (b, f, j) ρNO_3^- , (c, g, k) ρNH_4^+ , and (d, h, l) purea for the 55% (a-d), 10% (e-h), and 1% light levels (i-l). Where there are no bars in panels (d), (h) and (l), no data are available. The stations are labelled on the x-axis, and the general station locations are indicated by the different colours: red shades – Antarctic Peninsula, green shades – Larsen C Ice Shelf, blue shade – Weddell Gyre, light purple shades – early summer Fimbul Ice Shelf, and dark purple – late summer Fimbul Ice Shelf. The error bars represent ± 1 SE of replicate experiments ($n = 2$).

3.3.3. Rates of nitrite oxidation

Rates of $V_{\text{NO}_2^-}$ were low throughout the euphotic zone across the study region (average euphotic zone-integrated rates of $20.8 \pm 31.3 \mu\text{mol m}^{-2} \text{d}^{-1}$, equivalent to 0 to 3.6% (average of $0.7 \pm 1.1\%$) of ρNO_3^- , and increased rapidly below Z_{eu} (Figure 7). The highest euphotic zone rates were observed at WG1 (depth-specific average of $6.3 \pm 5.0 \text{ nM d}^{-1}$, integrated average of $113.6 \pm 4.3 \mu\text{mol m}^{-2} \text{d}^{-1}$), while the lowest rates occurred at the AP (depth-specific average of $0.0 \pm 0.04 \text{ nM d}^{-1}$, integrated average of $0.8 \pm 0.7 \mu\text{mol m}^{-2} \text{d}^{-1}$).

3.3.4. f-ratio estimates

At the stations where urea uptake was measured (LCIS stations and WG1; 11 out of 19 stations; Figure 6; Table 2), purea accounted for $8 \pm 6\%$ of total N uptake (i.e., $\rho\text{NO}_3^- + \rho\text{NH}_4^+ + \text{purea}$). Excluding urea uptake when calculating the f-ratio would therefore overestimate the fraction of potentially exportable carbon by $\sim 8\%$. We thus estimated urea uptake at the stations where it was not measured as:

$$\text{purea} = (\rho\text{NO}_3^- + \rho\text{NH}_4^+) \times 0.08 \quad (7)$$

Equation 7 may overestimate urea uptake at some of the stations, particularly where low urea concentrations were measured. Theoretically, ρ_{urea} can also be estimated by assuming that total N uptake should equal $NPP/6.63$, such that any difference between $\rho_{NO_3^-} + \rho_{NH_4^+}$ and $NPP/6.63$ is due to urea uptake. However, this approach underestimated urea uptake at all the stations where ρ_{urea} was directly measured, probably because the use of a C:N ratio of 6.63:1 assumes balanced phytoplankton growth. We therefore chose to use equation 7 to estimate urea uptake for the stations lacking ρ_{urea} measurements as this approach will yield a more conservative (i.e., lower) estimate of the fraction of potentially exportable carbon (section S3 in the Supplemental Information for more details). Figure 8 shows how including urea uptake affects the f-ratio throughout the sample region, with the white (no urea uptake measured) and hashed bars (urea uptake measured) indicating the amount by which the f-ratio decreased when urea uptake was included (i.e., equation 4b versus equation 4a).

The euphotic zone-integrated f-ratios were highest at FIS in early summer (average $f\text{-ratio}_{(excluding\ urea)}$ of 0.79 ± 0.1 and $f\text{-ratio}_{(including\ urea)}$ of 0.73 ± 0.09) and lowest at LCIS (average $f\text{-ratio}_{(excluding\ urea)}$ of 0.50 ± 0.09 and $f\text{-ratio}_{(including\ urea)}$ of 0.47 ± 0.08) (Figure 8; Table 2). The variability in the f-ratios among stations appears to be largely related to the availability of NH_4^+ . For example, at FIS in early summer there was no detectable NH_4^+ available to the phytoplankton and the highest f-ratios were observed (average $f\text{-ratio}_{(excluding\ urea)}$ of 0.82 ± 0.08 and $f\text{-ratio}_{(including\ urea)}$ of 0.76 ± 0.07), while in late summer, NH_4^+ concentrations were elevated ($0.2 \pm 0.1\ \mu M$) and the f-ratio declined ($f\text{-ratio}_{(excluding\ urea)}$ of 0.68 ± 0.16 and $f\text{-ratio}_{(including\ urea)}$ of 0.63 ± 0.15).

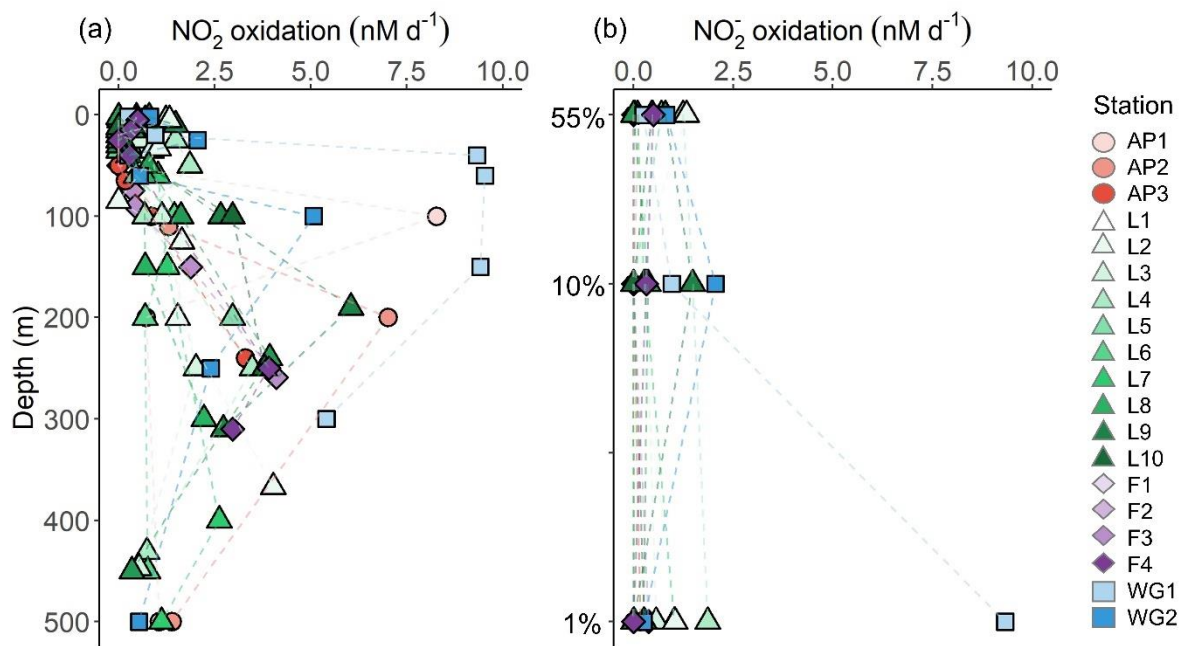


Figure 7. Depth profiles of NO_2^- oxidation rates measured at each station (a) between the surface and 500 m, and (b) within the euphotic zone.

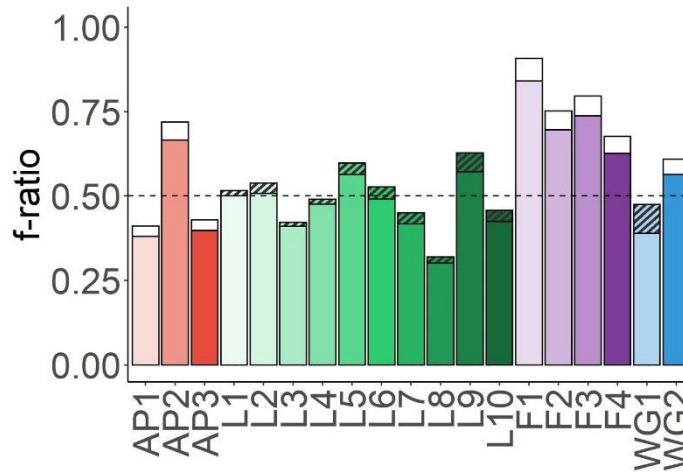


Figure 8. Euphotic zone-integrated f-ratios estimated for each station. The black-hashed and white bars show the difference between the $f\text{-ratio}_{(\text{excluding urea})}$ (higher value; equation 4a) and the $f\text{-ratio}_{(\text{including urea})}$ (lower value; equation 4b), with the black-hashed bars indicating the stations where urea uptake was measured and the white bars where it was estimated (see text for details).

3.3.5. Phytoplankton community composition

The flow cytometry data show that the phytoplankton community was numerically dominated by picoplankton at all stations, with *Synechococcus* emerging as the most abundant group ($59 \pm 19\%$ of the total phytoplankton cells counted), except at stations L5 and L6 where picoeukaryotes were dominant ($51 \pm 1\%$; Figure 9a-b). The microeukaryotes were the least abundant group at all stations (average abundance across the sampling region of $8 \pm 3\%$); however, due to their large biovolume, they contributed most to the biomass ($80 \pm 7\%$; Figure 9c). In the configuration used here, flow cytometry is best suited for enumerating small cells ($<15\ \mu\text{m}$; Dubelaar and Jonker 2000), such that the larger microplankton present at the time of sampling were likely underestimated via this technique. We thus take the phytoplankton net collections as more representative of the microplankton community and colonial nanoplankton groups.

From the samples collected using the phytoplankton net (i.e., single cells or colonies $>55\ \mu\text{m}$), the dominant phytoplankton species at LCIS was the prymnesiophyte, *P. antarctica* ($83 \pm 17\%$ of the total phytoplankton cells counted), while the phytoplankton community at the other stations was dominated by diatoms (mainly *Corethron pennatum*, *Chaetoceros* spp. (six species), *Cylindrotheca closterium*, *Fragilariopsis ritscheri*, *Fragilariopsis curta*, *Fragilariopsis kerguelensis*, *Fragilariopsis rhombica*, *Leptocylindrus mediterraneus*, *Odontella weisflogii*, *Pseudo-nitzschia alanata* and several *Thalassiosira* spp., constituting $92 \pm 6\%$ of the phytoplankton cells counted; Figure 9d-e). At LCIS, the stations sampled earlier in the season tended to be dominated by *P. antarctica* (e.g., station L3) while those sampled later hosted a more diatom-dominated community (e.g., station L8). In addition, the resident diatoms at LCIS (mainly *F. ritscheri*, *O. weisflogii*, and *Thalassiosira* spp.) were much larger than the numerically dominant *P. antarctica*. For example, at station L8, the 32 diatom species present ($1.6\ \text{cells mL}^{-1}$) contributed $1.80 \times 10^{-3}\ \text{pg C mL}^{-1}$ (Leblanc et al., 2012) compared to $0.14 \times 10^{-3}\ \text{pg C mL}^{-1}$ resulting from the $7.8\ \text{cells mL}^{-1}$ of *P. antarctica* (Mathot et al. 2000). The LCIS stations with the highest relative abundance of diatoms (e.g., station L8) were characterized by some of the highest rates of ρNO_3^- and greatest extent of NO_3^- depletion. More broadly, the LCIS stations with the lowest sea surface temperatures (SSTs) and nutrient uptake

rates (i.e., stations L1 and L3) had the lowest phytoplankton counts, while those with the highest SSTs and nutrient uptake rates (i.e., station L5 and L7) had the highest phytoplankton counts (Figure 9a and d; Table 1).

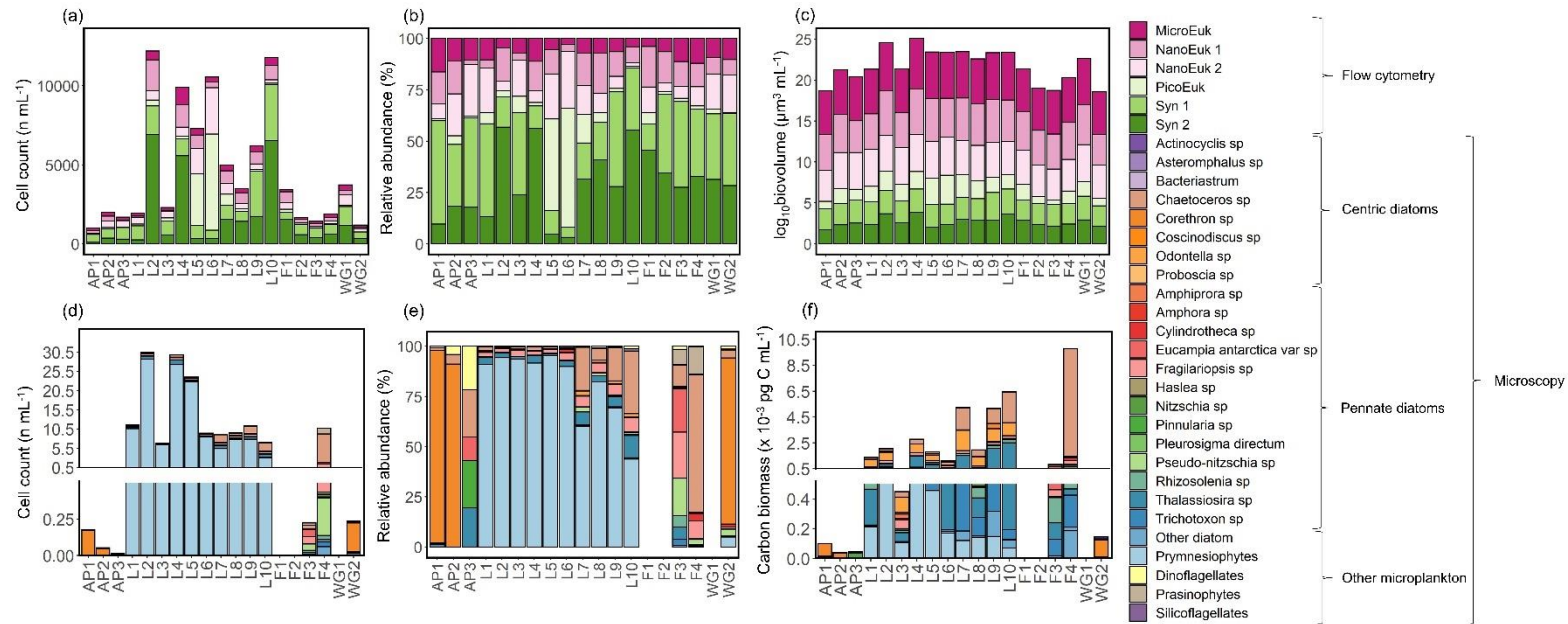


Figure 9. The (a, d) cell counts, (b, e) relative cell abundances, (c) log-transformed biovolume, and (f) carbon biomass of all phytoplankton groups identified from (a-c) surface flow cytometry samples and (d-f) plankton net-tow samples. The stations are labelled on the x-axis. Where there are no bars in panels (d), (e), and (f), no data are available. Carbon biomass estimates in panel (f) are shown only for the prymnesiophyte, *P. antarctica*, and the diatom species.

Table 1. Euphotic zone-averaged N nutrient concentrations, nutrient depletions, and nutrient depletion ratios at each station occupied in the Weddell Sea in January/February 2019. Values shown are averages \pm 1 SD ($n \geq 2$), with error propagated according to standard statistical practices where appropriate. “_” indicates no available data.

Station position	Station	Sampling date	Bottom depth (m)	MLD (m)	Z_{eu} (m)	NH_4^+ (μ M)	Urea-N (μ M)	NO_3^- (μ M)	NO_3^- depletion (μ M)	Si(OH) ₄ depletion (μ M)	PO_4^{3-} depletion (μ M)	Si(OH) ₄ : NO_3^- depletion (μ M: μ M)	NO_3^- : PO_4^{3-} depletion (μ M: μ M)
EIS Average	FIS		206 \pm 83	82 \pm 51	79 \pm 28	0.1 \pm 0.1	0.1 \pm 0.1	25.0 \pm 2.8	0.7 \pm 1.4	1.6 \pm 3.0	0.1 \pm 0.1	2.0 \pm 1.1	26.4 \pm 19.8
Fimbul	F1	01/01/19	130	135	100	0.0 \pm 0.0	-	26.4 \pm 0.5	0.2 \pm 0.5	0.5 \pm 1.6	0.0 \pm 0.0	3.2 \pm 3.9	-
Fimbul	F2	02/01/19	140	110	100	0.0 \pm 0.0	-	26.5 \pm 0.1	0.1 \pm 0.1	0.0 \pm 0.1	0.0 \pm 0.0	0.5 \pm 2.1	48.6 \pm 11.5
Fimbul	F3	03/01/19	281	63	75	0.0 \pm 0.0	0.0 \pm 0.0	26.0 \pm 0.3	0.7 \pm 0.3	1.2 \pm 0.5	0.0 \pm 0.0	1.8 \pm 0.6	18.8 \pm 1.1
Fimbul	F4	20/02/19	274	20	40	0.2 \pm 0.2	0.2 \pm 0.1	20.2 \pm 1.9	3.7 \pm 2.0	8.7 \pm 0.6	0.3 \pm 0.1	2.3 \pm 0.5	11.7 \pm 0.6
AP Average	AP		1451 \pm 847	23 \pm 8	45 \pm 9	0.8 \pm 0.2	0.3 \pm 0.1	24.9 \pm 0.6	2.5 \pm 1.7	1.1 \pm 0.8	0.1 \pm 0.1	0.6 \pm 0.2	19.8 \pm 16.5
Antarctic Peninsula	AP1	09/01/19	2155	23	35	0.6 \pm 0.1	0.2 \pm 0.1	25.6 \pm 1.4	2.6 \pm 0.7	1.4 \pm 0.4	0.2 \pm 0.1	0.5 \pm 0.4	14.1 \pm 0.4
Antarctic Peninsula	AP2	09/01/19	1686	30	50	0.7 \pm 0.1	0.2 \pm 0.1	25.9 \pm 1.0	1.0 \pm 1.1	0.8 \pm 0.2	0.1 \pm 0.0	0.8 \pm 1.1	6.8 \pm 1.1
Antarctic Peninsula	AP3	09/01/19	511	15	50	1.1 \pm 0.0	0.3 \pm 0.1	24.7 \pm 0.3	3.2 \pm 2.5	1.4 \pm 1.5	0.1 \pm 0.1	0.4 \pm 1.4	38.4 \pm 1.2
LCIS Average	LCIS		434 \pm 62	14 \pm 6	29 \pm 9	0.7 \pm 0.4	0.2 \pm 0.1	16.4 \pm 4.7	8.2 \pm 4.9	8.1 \pm 4.9	0.6 \pm 0.3	1.0 \pm 0.2	14.7 \pm 2.9
Larsen C	L1	22/01/19	376	8.5	33	1.3 \pm 0.1	0.4 \pm 0.1	21.8 \pm 0.1	2.0 \pm 0.1	2.3 \pm 0.3	0.2 \pm 0.1	1.2 \pm 0.1	11.2 \pm 0.3
Larsen C	L2	20/01/19	451	14	25	0.4 \pm 0.3	0.2 \pm 0.2	13.7 \pm 5.0	8.6 \pm 4.8	7.8 \pm 4.7	0.6 \pm 0.4	0.9 \pm 0.8	15.2 \pm 1.0
Larsen C	L3	11/01/19	431	7	50	0.9 \pm 0.1	0.2 \pm 0.1	23.1 \pm 0.2	2.2 \pm 0.1	1.3 \pm 0.8	0.1 \pm 0.1	0.6 \pm 0.6	17.7 \pm 0.3
Larsen C	L4	14/01/19	368	24	22	0.5 \pm 0.5	0.1 \pm 0.1	12.1 \pm 2.5	12.8 \pm 2.1	10.9 \pm 2.2	0.9 \pm 0.2	0.9 \pm 0.3	13.9 \pm 0.2
Larsen C	L5	15/01/19	451	10	25	0.1 \pm 0.0	0.4 \pm 0.2	12.0 \pm 1.9	10.9 \pm 2.3	9.6 \pm 1.7	0.8 \pm 0.1	0.9 \pm 0.3	13.7 \pm 0.2
Larsen C	L6	13/01/19	475	17.5	30	0.7 \pm 0.5	0.2 \pm 0.1	15.1 \pm 2.1	8.4 \pm 2.1	8.0 \pm 1.9	0.4 \pm 0.1	1.0 \pm 0.3	20.4 \pm 0.3
Larsen C	L7	22/01/19	506	8.5	25	1.0 \pm 1.1	0.2 \pm 0.1	14.7 \pm 4.1	11.1 \pm 1.8	13.5 \pm 3.4	0.8 \pm 0.2	1.2 \pm 0.3	14.8 \pm 0.3
Larsen C	L8	23/01/19	450	22.5	35	0.3 \pm 0.0	0.2 \pm 0.0	12.2 \pm 2.2	12.9 \pm 4.5	12.4 \pm 3.2	0.8 \pm 0.3	1.0 \pm 0.4	16.0 \pm 0.5
Larsen C	L9	19/01/19	318	12.5	20	0.5 \pm 0.4	0.2 \pm 0.1	20.2 \pm 4.3	5.8 \pm 3.3	6.6 \pm 5.1	0.5 \pm 0.3	1.1 \pm 1.0	11.0 \pm 0.9
Larsen C	L10	24/01/19	510	14	20	0.7 \pm 0.3	0.2 \pm 0.1	18.2 \pm 5.4	8.7 \pm 3.7	10.6 \pm 4.9	0.7 \pm 0.3	1.2 \pm 0.6	13.0 \pm 0.6
WG Average	WG		3565 \pm 379	20 \pm 0	90 \pm 14	0.2 \pm 0.2	0.1 \pm 0.1	28.8 \pm 2.4	0.4 \pm 0.3	2.0 \pm 0.9	0.1 \pm 0.0	5.6 \pm 0.7	4.1 \pm 0.6
Weddell Gyre	WG1	14/02/19	3297	20	100	0.2 \pm 0.2	0.1 \pm 0.1	26.7 \pm 0.5	0.4 \pm 0.3	2.3 \pm 0.8	0.1 \pm 0.0	5.1 \pm 0.7	4.5 \pm 0.7
Weddell Gyre	WG2	15/02/19	3833	20	80	0.4 \pm 0.1	0.1 \pm 0.1	30.2 \pm 0.8	0.3 \pm 0.4	2.0 \pm 1.0	0.1 \pm 0.1	6.1 \pm 1.3	3.7 \pm 1.5

Table 2. Euphotic zone-integrated and averaged rates at each station occupied in the Weddell Sea in January/February 2019. Values shown are averages \pm 1 SD ($n \geq 2$), with error propagated according to standard statistical practices where appropriate. “–” indicates no available data. The values shown in italics (i.e., purea) were estimated rather than measured (see text for details).

Station position	Station	[POC] (μM)	[PON] (μM)	C:N ratio	NPP ($\text{mmol m}^{-2} \text{d}^{-1}$)	ρNO_3^- ($\text{mmol m}^{-2} \text{d}^{-1}$)	ρNH_4^+ ($\text{mmol m}^{-2} \text{d}^{-1}$)	purea ($\text{mmol m}^{-2} \text{d}^{-1}$)	$V\text{NO}_3^-$ ($\mu\text{mol m}^{-2} \text{d}^{-1}$)	f-ratio _(excluding urea)	f-ratio _(including urea)
FIS Average	FIS	8.0 \pm 8.4	0.8 \pm 0.9	16.5 \pm 8.8	27.5 \pm 26.6	3.7 \pm 1.0	0.8 \pm 0.4	0.5 \pm 0.4	5.2 \pm 0.7	0.80 \pm 0.10	0.73 \pm 0.09
Fimbul	F1	5.9 \pm 2.0	0.3 \pm 0.2	21.6 \pm 3.7	4.9 \pm 0.0	3.8 \pm 0.0	0.4 \pm 0.0	0.3 \pm 0.0	–	0.91	0.84
Fimbul	F2	4.9 \pm 3.4	0.2 \pm 0.0	26.3 \pm 12.6	20.8 \pm 0.2	2.4 \pm 0.0	0.8 \pm 0.0	0.07 \pm 0.0	–	0.75	0.70
Fimbul	F3	3.1 \pm 1.8	0.4 \pm 0.2	8.8 \pm 3.0	56.9 \pm 0.6	4.8 \pm 0.1	1.2 \pm 0.0	0.5 \pm 0.0	4.7 \pm 1.6	0.80	0.74
Fimbul	F4	17.9 \pm 7.2	2.1 \pm 0.6	9.4 \pm 0.5	28.3 \pm 0.4	3.9 \pm 0.0	1.9 \pm 0.0	0.9 \pm 0.0	5.7 \pm 1.7	0.68	0.63
AP Average	AP	8.7 \pm 6.3	1.1 \pm 0.3	8.3 \pm 2.5	26.6 \pm 33.5	3.4 \pm 1.4	3.8 \pm 2.0	0.5 \pm 0.2	0.8 \pm 0.7	0.52 \pm 0.17	0.48 \pm 0.16
Antarctic Peninsula	AP1	7.4 \pm 0.7	1.3 \pm 0.1	6.1 \pm 1.4	3.1 \pm 0.1	1.8 \pm 0.1	2.6 \pm 0.0	0.4 \pm 0.0	0.0 \pm 3.3	0.41	0.38
Antarctic Peninsula	AP2	4.3 \pm 3.5	0.8 \pm 0.3	7.8 \pm 2.7	11.8 \pm 0.2	4.0 \pm 0.2	2.1 \pm 0.0	0.4 \pm 0.0	1.0 \pm 2.7	0.72	0.67
Antarctic Peninsula	AP3	14.4 \pm 5.2	1.3 \pm 0.2	11.0 \pm 2.1	65.0 \pm 0.1	4.4 \pm 0.0	5.8 \pm 0.0	0.8 \pm 0.0	1.3 \pm 1.3	0.43	0.40
LCIS Average	LCIS	18.8 \pm 22.1	2.4 \pm 0.8	7.4 \pm 1.9	28.6 \pm 21.3	2.2 \pm 1.1	2.6 \pm 1.3	0.6 \pm 0.3	17.3 \pm 20.6	0.50 \pm 0.09	0.47 \pm 0.08
Larsen C	L1	16.9 \pm 5.9	1.5 \pm 0.3	10.0 \pm 3.4	2.2 \pm 0.1	1.5 \pm 0.0	1.4 \pm 0.0	0.2 \pm 0.0	16.7 \pm 0.7	0.52	0.50
Larsen C	L2	21.2 \pm 7.1	3.1 \pm 0.5	6.3 \pm 1.7	47.8 \pm 0.5	1.5 \pm 0.1	3.3 \pm 0.0	0.8 \pm 0.0	9.4 \pm 0.6	0.54	0.51
Larsen C	L3	5.9 \pm 0.1	2.6 \pm 0.8	5.8 \pm 1.4	32.0 \pm 0.1	2.5 \pm 0.0	3.3 \pm 0.0	0.3 \pm 0.0	–	0.42	0.41
Larsen C	L4	25.1 \pm 4.7	1.0 \pm 0.2	8.0 \pm 0.5	32.2 \pm 1.0	1.9 \pm 0.1	2.1 \pm 0.0	0.2 \pm 0.0	69.0 \pm 1.0	0.49	0.48
Larsen C	L5	17.3 \pm 6.3	3.1 \pm 0.6	7.4 \pm 1.9	61.0 \pm 0.7	4.7 \pm 0.0	3.1 \pm 0.0	0.9 \pm 0.0	7.0 \pm 0.5	0.60	0.56
Larsen C	L6	10.0 \pm 1.3	2.4 \pm 0.5	9.2 \pm 5.3	25.9 \pm 1.5	2.4 \pm 0.1	2.2 \pm 0.1	0.7 \pm 0.0	23.0 \pm 0.9	0.53	0.49
Larsen C	L7	27.1 \pm 10.3	1.5 \pm 0.7	8.2 \pm 1.1	55.9 \pm 1.0	3.1 \pm 0.0	3.8 \pm 0.1	1.1 \pm 0.0	0.2 \pm 0.9	0.45	0.42
Larsen C	L8	23.5 \pm 3.3	3.3 \pm 0.3	8.2 \pm 1.3	17.3 \pm 0.4	2.3 \pm 0.0	4.8 \pm 0.1	0.9 \pm 0.0	8.7 \pm 1.5	0.32	0.30
Larsen C	L9	17.1 \pm 1.6	2.9 \pm 0.2	3.4 \pm 4.1	9.7 \pm 1.3	2.0 \pm 0.1	1.2 \pm 0.0	0.6 \pm 0.0	16.5 \pm 2.3	0.63	0.57
Larsen C	L10	23.6 \pm 14.9	2.7 \pm 1.1	7.1 \pm 0.4	1.8 \pm 0.0	0.5 \pm 0.0	0.6 \pm 0.0	0.2 \pm 0.0	5.2 \pm 1.6	0.46	0.42
WG Average	WG	8.0 \pm 8.9	0.7 \pm 0.3	12.3 \pm 1.8	31.6 \pm 31.3	3.2 \pm 0.1	2.0 \pm 0.2	0.5 \pm 0.1	81.9 \pm 44.7	0.54 \pm 0.10	0.48 \pm 0.12
Weddell Gyre	WG1	5.8 \pm 4.0	0.5 \pm 0.2	13.6 \pm 7.7	53.7 \pm 0.2	3.3 \pm 0.0	2.1 \pm 0.0	0.6 \pm 0.0	113.6 \pm 4.3	0.47	0.39
Weddell Gyre	WG2	10.1 \pm 7.9	0.9 \pm 0.3	11.0 \pm 7.5	9.5 \pm 0.4	3.1 \pm 0.0	1.8 \pm 0.0	0.4 \pm 0.0	50.3 \pm 1.8	0.61	0.56

4. Discussion

For the regions of the Weddell Sea that we sampled in summer 2019, the euphotic zone-integrated rates of NPP and N uptake were generally lower at the OOOZ stations than the CCSZ stations, with the highest depth-specific uptake rates observed in surface waters at LCIS (Figure 6a-d; Table 2). The few studies that have previously measured summertime rates of NPP and N uptake in the Weddell Sea report similar results, with rates in the marginal ice zone (MIZ) and CCSZ that were up to five-times higher than in the OOOZ (El-Sayed and Taguchi, 1981; Smith and Nelson, 1990; Park et al., 1999). The summertime CCSZ of the Weddell Sea can thus be broadly characterised as a highly productive region with elevated biomass accumulation driven by increased water-column stratification and iron-replete conditions, both the result of sea-ice melt (Semeneh et al., 1998; Lannuzel et al., 2008; Klunder et al., 2011). That said, we observed considerable variability in the biogeochemical rates measured in each region of the Weddell Sea, particularly at LCIS; we examine the possible drivers of and controls on the inter- and intra-regional differences below.

4.1. Drivers of NPP and N uptake in the Weddell Sea

Light and water column stability: Surface waters throughout the study region were generally well stratified, with MLDs ranging from 7 to 30 m, except at the early-summer FIS stations where the MLD ranged from 63 to 135 m (Table 1). These deep MLDs coincided with elevated sea-ice concentrations, while the shallowest MLDs at LCIS occurred in relatively ice-free waters (Table 1). Average euphotic zone rates of NPP typically increased with increasing SST and POC concentration (Figure 10a and c), implicating water column stratification and biomass (which affects light penetration in addition to carbon production rate) as controls on NPP. By contrast, average euphotic zone rates of ρNO_3^- generally varied with MLD and Z_{eu} – they were highest (lowest) at the stations where Z_{eu} was shallowest (deepest) (Figure 10b) – implicating light as a control on ρNO_3^- . At LCIS, the euphotic zone was shallow at all stations (<50 m, with an average Z_{eu} of 28.5 ± 9 m), yet ρNO_3^- varied by over an order of magnitude (Table 2). Here, we observed a positive relationship between the rates and SST, with ρNO_3^- increasing at higher SSTs, the latter indicative of increased water column stratification (Figures 10a and S4b; see below).

Throughout the sampling region, the average euphotic zone rates of ρNH_4^+ and purea also varied with Z_{eu} which could be taken to indicate that these processes were also light dependent. However, such a finding would be unexpected, as the energy requirement associated with NH_4^+ and urea assimilation is low (El-Sayed and Taguchi 1981; Dortch 1990; Priddle et al. 1998). The observed relationship is more likely due to the *in situ* biomass, which i) attenuates light and ii) provides a source of organic matter for the production of NH_4^+ and dissolved organic N, including urea. Indeed, the stations with the deepest Z_{eu} were characterized by low concentrations of particulate organic matter and regenerated N (Figures 3a-b and 5), leading us to conclude that ρNH_4^+ and purea were predominantly controlled by the availability of regenerated N (Figures 10d-e and S3b; section S4 in the Supplemental Information). This conclusion is supported by the positive relationship observed between ρNH_4^+ or purea and the coincident NH_4^+ or urea concentrations (Figure 10d-e).

The lowest regenerated N concentrations occurred at the stations with the lowest rates of NPP and ρNO_3^- , and the highest NO_3^- concentrations (e.g., station F1). This is probably because NH_4^+ and urea tend to accumulate only when biomass (and productivity) is sufficiently high to support elevated rates of heterotrophic activity (Semeneh

et al., 1998). At the stations with low POC and PON concentrations, remineralisation rates were likely also low, limiting the flux of NH_4^+ and urea (Figure 10f) and driving low rates of pNH_4^+ and purea (Figure 10d-e). At the stations where NH_4^+ and urea concentrations were elevated, rates of pNH_4^+ and purea increased with depth, along with a decrease in NPP and pNO_3^- (e.g., station L8). These observations further demonstrate the control of biomass on NPP, light on pNO_3^- , and substrate availability on pNH_4^+ and purea. That said, it is unlikely that the variability in NPP and N uptake among the stations was driven by biomass, light, and nutrient availability alone, and we hypothesize that hydrography, iron availability, and phytoplankton community composition also played a role.

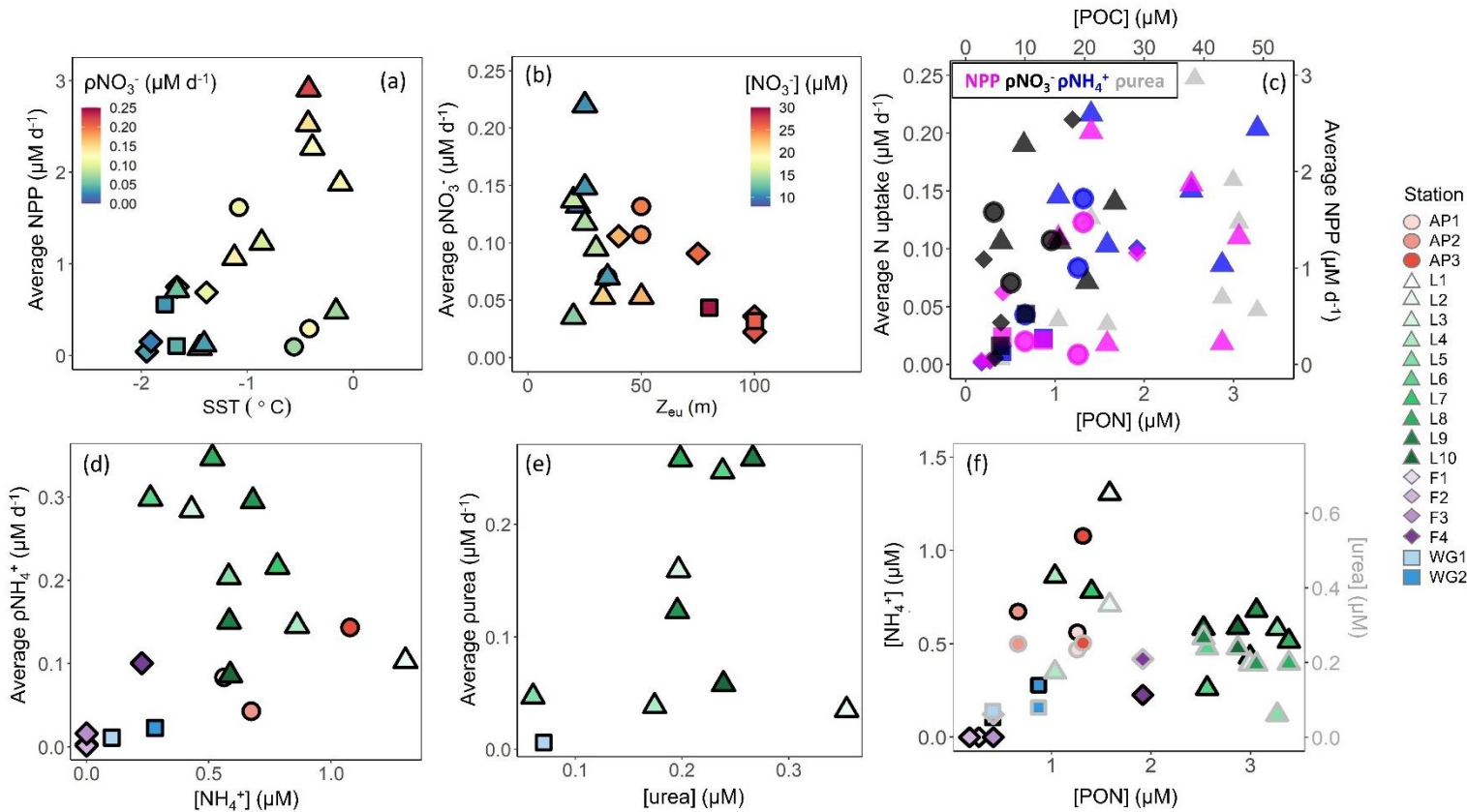


Figure 10. Euphotic zone-averaged rates of (a) NPP versus SST, (b) pNO_3^- versus euphotic zone depth (Z_{eu}), (c) N uptake (left y-axis) versus PON (bottom x-axis) and NPP (right y-axis) versus POC (top x-axis), (d) pNH_4^+ versus NH_4^+ concentration, and (e) purea versus urea concentration, as well as (f) the concentrations of NH_4^+ (black outlined symbols; left y-axis) and urea (grey outlined symbols; right y-axis) versus PON at each station. The symbols in panel (a) are coloured by pNO_3^- , in panel (b) by NO_3^- concentration, and in panel (c) by NPP (pink), pNO_3^- (black), pNH_4^+ (blue), and purea (grey).

At LCIS, the stations closest to the ice shelf were characterised by low SSTs and low rates of NPP and N uptake (stations L1 and L3; Figures 1, S4 and S5a; Table 2). The low SSTs can be attributed either to the formation of sea-ice or to the upwelling of WW along the ice shelf. Sea-ice formation, in addition to decreasing SST, also increases the salinity of ASW due to brine rejection (Gill 1973). While the salinity of ASW at the low-SST stations was indeed elevated, the oxygen concentrations were relatively low ($\leq 300 \mu\text{M}$, which is below saturation; Figure S5b-d). In surface waters and sea-ice, oxygen is typically saturated as it rapidly equilibrates with the atmosphere (Gleitz et al., 1995) and is produced by photosynthesizing phytoplankton and sea-ice algae. Sea-ice formation should not, therefore, drive a decrease in the oxygen content of ASW. The low oxygen concentrations at stations

L1 and L3 were contiguous with those in the underlying WW (Figure S5d), leading us to conclude that the cool, saline waters along the ice-shelf indicate recent upwelling of WW. Such upwelling could temporarily inhibit productivity by decreasing the stability of the water column and mixing phytoplankton below the euphotic zone. This mechanism can explain the low uptake rates and weak nutrient depletions observed at the low-SST stations.

Relatively cold, saline surface waters have previously been observed at the ice-edge off Larsen A and B Ice Shelves and shown to hinder NPP (Cape et al., 2014). In that case, the dense surface waters were surmised to result either from offshore wind stress at the inshore region that induced localised mixing, or from the advection of surface waters offshore by coastal upwelling. Both mechanisms would decrease water column stability, and by extension, productivity. Cape et al. (2014) observed an increase in NPP with distance from the coast at Larsen A and B, a trend that we did not observe, likely because of the proximity of our LCIS stations to the ice shelf (within 75 km for all stations). Instead, our rates of NPP and N uptake were positively coupled with SST at the ice-edge (Figures S4 and S5). We propose that surface SST at LCIS can be used as an indicator of water-mass age, with cooler SSTs indicating newly-upwelled WW and warmer SSTs designating older surface waters that have had time to absorb heat from the atmosphere. The higher rates of NPP and N uptake in the warmer surface waters occur because phytoplankton experience favourable growing conditions for an extended period, resulting in biomass accumulation. By contrast, persistent localised upwelling along LCIS inhibits productivity in the adjacent surface waters, with implications for the spatial distribution of biomass and the potential for organic carbon export.

Nutrient and inferred iron conditions in Weddell Sea surface waters: Across our sampling region, ASW was depleted in NO_3^- , Si(OH)_4 , and PO_4^{3-} relative to the underlying WW, with the greatest nutrient depletion occurring at LCIS and at FIS in late summer (Figure 4a-c). Because diatoms and/or *P. antarctica* were the dominant phytoplankton at all stations (Figure 9d-f), we can use the Si:N:P depletion ratios (here used as shorthand for the $\text{Si(OH)}_4\text{:NO}_3\text{:PO}_4^{3-}$ depletion ratios) to assess the iron conditions and N nutrition of these two phytoplankton groups. Under iron-replete conditions, diatoms consume Si:N:P in an approximate ratio of 1:1:0.07 (Ragueneau et al. 2000; Hutchins and Bruland 1998; Takeda 1998; Mosseri et al. 2008), while under iron-limitation, they increase their uptake of Si and decrease that of P relative to N, consuming nutrients in a ratio of $\geq 2\text{:}1\text{:}0.09$ (Arrigo et al., 1999; Finkel et al., 2006; Green and Sambrotto, 2006; Mosseri et al., 2008; Weber and Deutsch, 2010; Martiny et al., 2013), with Si:N uptake ratios as high as 8:1 observed under conditions of extreme iron depletion (Franck et al., 2000; Brzezinski et al., 2003). At a first approximation, the Si:N:P depletion ratios estimated in our study suggest that the AP and LCIS stations were characterised by iron-replete conditions (ratio of 0.9:1:0.06) while phytoplankton community at the FIS and WG stations experienced iron limitation (ratios of 3.6:1:0.15; Figure 4d-e; Table 1).

High iron concentrations have previously been measured in surface waters in the CCSZ and northern Weddell Sea (as high as 7 nM; Lannuzel et al. 2008; De Jong et al. 2012). Iron is supplied to the mixed layer in these regions via sea-ice melt, ice shelf melt, continental runoff, vertical and lateral advection, and resuspension of continental shelf sediments (Lannuzel et al., 2008; De Jong et al., 2012; Klunder et al., 2014). In contrast, the central WG is iron-limited as iron is supplied to surface waters mainly by wind-induced vertical mixing (Hoppema et al. 2015). During our sampling, sea-ice concentrations were high at the WG stations, which would have dampened the effect

of wind stress on surface waters and thus hindered vertical mixing. At FIS in early summer, iron should have been replete as phytoplankton would not have had sufficient time to exhaust the surface reservoir. Here, the sea-ice concentrations were elevated, and the mixed layers were deep such that light, rather than iron, likely limited phytoplankton growth. Indeed, light-limited diatoms have been observed to consume Si:N:P in a ratio similar to that reported for conditions of iron depletion (Brzezinski, 1985). By late summer at FIS, the sea-ice had completely melted, which should have further alleviated iron limitation, yet the Si:N depletion ratios were high (average of 2.3 ± 0.5). These elevated ratios may be the result of only considering NO_3^- uptake and not accounting for regenerated N consumption. At FIS in late summer, NH_4^+ supported 32% of N uptake; accounting for this N source decreases the Si:N depletion ratio to 1.4:1, which is closer to expectations for iron-replete diatoms. Some diatom growth was likely also supported by urea, which would further decrease the Si:N depletion ratio. Additionally, it is plausible that the diatoms at station F4 were beginning to experience iron-limitation as sampling occurred late in the season.

Accounting for regenerated N uptake greatly alters the Si:N depletion ratios, particularly at LCIS, and provides insights into the behaviour of the dominant phytoplankton groups that were active in the mixed layer, both prior to and at the time of sampling. At the stations where diatoms dominated, the Si: NO_3^- depletion ratios were elevated and ρNO_3^- was high (Figure 11a and c). In contrast, at the stations where *P. antarctica* was dominant, the Si: NO_3^- depletion ratios were low (generally <1) and regenerated N uptake was high relative to the other stations (Figure 11a and d). Under favourable nutrient and light conditions, diatoms will typically consume NO_3^- over NH_4^+ as i) NO_3^- is usually present in substantially higher concentrations than NH_4^+ and ii) the lower surface area-to-volume ratio of (larger) diatoms makes it harder for them to compete with smaller cells for a less abundant resource (i.e., NH_4^+) (Probyn and Painting, 1985; Koike et al., 1986; Lomas and Glibert, 1999; Karsh et al., 2003). The average Si: NO_3^- depletion ratio of 1.0 ± 0.2 at LCIS can therefore be attributed almost entirely to diatoms. When total N uptake is considered, the Si:N depletion ratios decrease to 0.3 ± 0.1 , indicating the consumption of three-times more N than Si(OH)_4 . We attribute this decline to regenerated N uptake by *P. antarctica*, a phytoplankton group that is known to preferentially consume NH_4^+ when it is available due to the lower energy and iron requirements of NH_4^+ assimilation (El-Sayed and Taguchi, 1981; Dortch, 1990; Jacques, 1991; Goeyens et al., 1995; Priddle et al., 1998; Stefels and Van Leeuwe, 1998).

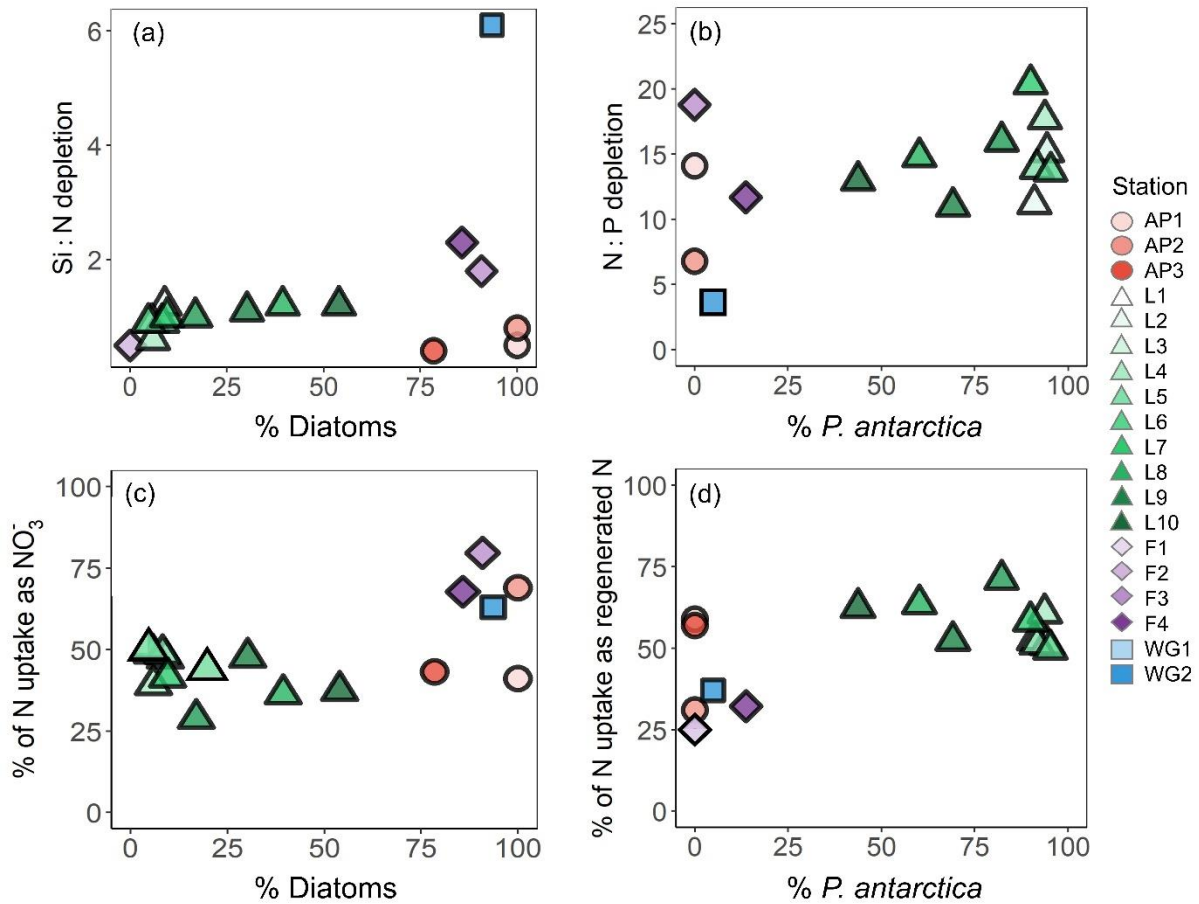


Figure 11. Scatterplots of (a) the Si:N depletion ratio (i.e., Si(OH)_4 -to-total N depletion) versus the % diatom abundance, (b) N:P depletion ratio (i.e., total N-to- PO_4^{3-} depletion) versus the % *P. antarctica* abundance, (c) % of total N (i.e., $\text{NO}_3^- + \text{NH}_4^+ + \text{urea}$) assimilated as NO_3^- versus the % diatom abundance, and (d) % of total N assimilated as regenerated N (i.e., $\text{NH}_4^+ + \text{urea}$) versus the % *P. antarctica* abundance at each station.

We can also use the $\text{NO}_3^-:\text{PO}_4^{3-}$ depletion ratios to better understand the iron conditions and relative importance of *P. antarctica* versus diatoms in generating the observed nutrient depletion ratios. *P. antarctica* are known to consume NO_3^- and PO_4^{3-} in a ratio of $\sim 20:1$, while for iron-replete diatoms, this ratio is $<14:1$ (Arrigo et al. 1999; Smith and Asper 2001; Garcia et al. 2018). At LCIS, the $\text{NO}_3^-:\text{PO}_4^{3-}$ depletion ratio averaged 14.7 ± 2.9 , consistent with a dominant role for iron-replete diatoms. However, variability in the $\text{NO}_3^-:\text{PO}_4^{3-}$ depletion ratios was observed among the LCIS stations (with ratios ranging from 11 to 20), which can be explained by local variations in phytoplankton community composition. At stations where large diatoms were dominant (e.g., L10, where diatoms contributed $6.47 \times 10^{-3} \text{ pg C mL}^{-1}$ to biomass while *P. antarctica* only contributed $0.07 \times 10^{-3} \text{ pg C mL}^{-1}$), the $\text{NO}_3^-:\text{PO}_4^{3-}$ depletion ratios were low (13.0 ± 0.6 ; Figure 11b). In contrast, at the stations where *P. antarctica* were numerically dominant (e.g., L6; where *P. antarctica* constituted 90% of the microphytoplankton) and contributed more to biomass ($0.17 \times 10^{-3} \text{ pg C mL}^{-1}$), elevated $\text{NO}_3^-:\text{PO}_4^{3-}$ depletion ratios were measured (20.4 ± 0.3 ; Figure 11b; Table 1). Furthermore, high rates of NH_4^+ uptake were measured at LCIS, equivalent to and at times greater than the coincident NO_3^- uptake rates (Figure 6; Table 2), particularly at the stations with the highest relative abundance of *P. antarctica*. In general, the relative contribution of diatoms versus *P. antarctica* therefore appears to control the nutrient depletion ratios on a variety of scales in the Weddell Sea.

Drivers of phytoplankton community composition: Phytoplankton community composition and the variations therein have implications for the biological carbon pump, both directly (diatoms sink more rapidly than smaller and/or non-ballasted phytoplankton; Treguer and Jacques 1992; De Baar et al. 2005; Boyd et al. 2007) and indirectly (NO_3^- consumption is quantitatively related to carbon export; Dugdale and Goering 1967; Eppley and Peterson 1979). Above, we have discussed the role of phytoplankton community composition in controlling productivity and upper ocean nutrient cycling. Below, we discuss the processes that may have caused *P. antarctica* to dominate over diatoms at LCIS, and vice versa at the other Weddell Sea stations.

At LCIS, a coastal sensible heat polynya persisted throughout the sampling period. The opening of such polynyas along the eastern AP is linked to the occurrence of warm, föhn winds that originate over the continent and blow over the AP, influencing the coastal north-western Weddell Sea (Cape et al., 2014). Föhn winds drive the offshore movement of sea-ice, which initiates the opening of polynyas that persist because the winds are warm, thus hindering the formation of new sea-ice (Cape et al., 2014). The development of coastal sensible heat polynyas results in relatively deep mixed layers and a weakly stratified water column. The polynya at LCIS opened in late November, approximately two months prior to our sampling. At this time (i.e., the beginning of the growing season), motile *P. antarctica* cells likely dominated the phytoplankton community as *P. antarctica* are low-light specialists compared to other Antarctic phytoplankton (Goffart et al., 2000; Alderkamp et al., 2012; Delmont et al., 2014). This notion is supported by the generally low phytoplankton cell counts (for both flow cytometry and net-tow samples) and high relative abundance of *P. antarctica* compared to diatoms at the stations along the ice shelf where WW had recently upwelled (e.g., L3; Figures 9a, d, e and S5). As the mixed layer shoaled into the summer and light limitation was alleviated, a diatom bloom would have been initiated and *P. antarctica* would have formed colonies (Schoemann et al., 2005) – indeed, the presence of *P. antarctica* colonies and diatom chains at the time of our sampling in January is evidence that the water column was well stratified (Goffart et al. 2000). As the season progressed, diatoms would have outcompeted *P. antarctica* and come to dominate the phytoplankton community. At the stations sampled later in the season (e.g., L10; Figure 9e), the relative abundance of diatoms versus *P. antarctica* was higher than at the stations occupied two weeks earlier (e.g., L5; Figure 9e). Diatoms have a lower iron and higher light requirement than *P. antarctica* and thus tend to thrive once the *P. antarctica* bloom declines, when the water column has stratified and they can access the lower concentrations of residual iron (Strzepek et al., 2011). That said, iron is likely perennially high at LCIS in summer as it is near-continuously supplied to surface waters by sea-ice melt and upwelling of WW along the ice shelf (Klunder et al., 2014). The elevated iron concentrations would allow the diatoms to grow rapidly on the available NO_3^- once the mixed layer had shoaled enough to alleviate light limitation, contributing to their capacity to outcompete other phytoplankton.

At the other (non-LCIS) sampling sites, diatoms dominated the phytoplankton community. We hypothesize that at the beginning of the growing season, melting sea-ice alleviated light- and, to a lesser extent, iron limitation, providing favourable conditions for diatom growth. At the same time, the generally lower iron concentrations characteristic of open Weddell Sea surface waters may have selected against *P. antarctica* (Strzepek et al., 2011). Previous studies conducted in the Ross Sea observed large diatom blooms associated with the receding ice-edge and concluded that bloom formation was favoured by the rapid stabilization of the water column from meltwater

inputs (Goffart et al. 2000; Sedwick et al. 2000). Regions of the Weddell Sea that undergo rapid stratification due to sea-ice melt will likely also experience large diatom blooms. We thus conclude that the dominance of diatoms over *P. antarctica* at the non-LCIS stations was influenced by local hydrodynamic processes that rapidly induce water column stability, and increase light availability (e.g., in areas of recent sea-ice melt). By contrast, *P. antarctica* dominates under low-light, such as in the deep mixed layers that initially characterize coastal polynyas. Eventually, diatoms will succeed *P. antarctica* in these polynyas as conditions become favourable for their growth.

4.2. Carbon export potential across the Weddell Sea

Previous f-ratio estimates for the summertime Weddell Sea range from 0.18 to 0.83 (Koike et al. 1986; Rönner et al. 1983; Nelson et al. 1987; Smith and Nelson 1990; Goeyens 1991; Goeyens et al. 1995). Using equations 4a and 4b, we calculate euphotic zone-integrated f-ratios that range from 0.32 to 0.91 (excluding urea uptake) and 0.30 to 0.84 (including urea uptake). The lowest f-ratios occurred at LCIS ($f\text{-ratio}_{(\text{excluding urea})} = 0.50 \pm 0.09$ and $f\text{-ratio}_{(\text{including urea})} = 0.47 \pm 0.08$) and the highest at FIS ($f\text{-ratio}_{(\text{excluding urea})} = 0.78 \pm 0.1$ and $f\text{-ratio}_{(\text{including urea})} = 0.73 \pm 0.09$) (Figure 8; Table 2). We note that urea uptake may have been stimulated at the stations where it was measured given the quantity of ^{15}N -urea added ($0.1 \mu\text{M}$) relative to the ambient urea concentrations (average of $0.2 \pm 0.1 \mu\text{M}$; Figure S2; section S3 in the Supplemental Information); if so, regenerated production could be overestimated at all stations since we extrapolated the average measured contribution of urea-to-total-N uptake ($8 \pm 6\%$) to the stations at which purea was not measured (equation 7). The f-ratio estimates excluding and including urea uptake thus represent an upper and lower bound, respectively, on the fraction of potentially exportable carbon. That said, accounting for urea uptake decreased the average f-ratio by very little, from 0.57 ± 0.15 to 0.52 ± 0.14 .

Estimates of the f-ratio and carbon export potential can be complicated by euphotic zone nitrification, which supplies regenerated rather than new NO_3^- to phytoplankton. Failing to account for this regenerated N flux can lead to an overestimation of carbon export potential (Yool et al. 2007; Mdutyana et al. 2020). At all stations, the euphotic zone rates of $V_{\text{NO}_2^-}$ were low (undetectable to 9.5 nM d^{-1} , average of $0.6 \pm 1.4 \text{ nM d}^{-1}$; Figure 7b) and correcting the f-ratio for these rates (equation 4) had a minimal effect (average decrease of $2 \pm 6\%$). The largest decrease was observed at WG1 where the highest euphotic zone-integrated rates of $V_{\text{NO}_2^-}$ were measured ($f\text{-ratio}_{(\text{excluding urea})}$ decreased from 0.60 to 0.47 and $f\text{-ratio}_{(\text{including urea})}$ decreased from 0.49 to 0.39; Table 2).

The low rates of euphotic zone nitrification are consistent with the previous (limited) data available for the summertime OÖZ and CCSZ of the Southern Ocean. For example, Mdutyana et al. (2020) measured euphotic zone rates of NO_2^- and NH_4^+ oxidation in summer at FIS and in the OÖZ just north of the WG ($56^\circ\text{S } 0^\circ\text{E}$) that were below detection. Summertime studies of euphotic zone NH_4^+ oxidation in the Ross and Scotia Seas also report low rates, of $6\text{--}8.9 \text{ nM d}^{-1}$ and $0.4\text{--}5.8 \text{ nM d}^{-1}$, respectively (Olson, 1981). We conclude that, as expected, the high-light and generally low- NH_4^+ conditions of the summertime Weddell Sea inhibited euphotic zone nitrification, and that the slow growing-nitrifiers were probably also outcompeted by phytoplankton for NH_4^+ (Ward 1985; 2005; Smith et al. 2014; Zakem et al. 2018). Classifying NO_3^- uptake as new production and equating it to carbon export potential is thus reasonable for the summertime Weddell Sea.

Although the highest f-ratios were estimated for the FIS stations, the highest rates of ρNO_3^- were observed at LCIS and along the AP (Figure 8; Table 2). FIS was thus characterised by the highest carbon export potential relative to NPP, while the N cycle data imply that the absolute potential carbon export flux was highest at LCIS and the AP. The maximum extent of nutrient depletion was also observed at LCIS (NO_3^- depletion of 57-428 mmol m^{-2} and PO_4^{3-} depletion of 5.8-18.7 mmol m^{-2}). Assuming Redfield C:N and C:P stoichiometry of 6.63:1 and 106:1, respectively, the seasonal NO_3^- depletion equates to a carbon export flux of 0.4-2.8 mol C m^{-2} and the PO_4^{3-} depletion to 0.6-2.0 mol C m^{-2} . Alternately, multiplying ρNO_3^- by the length of time that the coastal polynya had been open (30 November until the date of sampling; Table 1) yields an estimate for net seasonal NO_3^- uptake of 59-428 mmol m^{-2} and carbon export flux of 0.4-2.8 mol C m^{-2} at LCIS, remarkably similar to the estimates derived from seasonal NO_3^- depletion. Our estimates of carbon export potential are, however, on the low end of those reported previously for the CCSZ and MIZ of the Weddell Sea (e.g., estimates for January/February range from 2.4-4.9 mol C m^{-2} ; R  nner et al. 1983; Hoppema et al. 2000; 2007). Given the high-light and nutrient- and iron-replete conditions encountered at LCIS, one might thus have expected higher f-ratios and estimates of carbon export potential (i.e., NO_3^- depletion), raising the question of the possible limitations thereon.

Throughout the Weddell Sea, NH_4^+ and urea uptake were coupled with substrate availability, while NO_3^- uptake was not. Instead, NO_3^- uptake appeared to vary with light (see above) and as a function of the ambient NH_4^+ concentration (Figure 12a). At LCIS where NH_4^+ was elevated throughout the mixed layer at all stations, NO_3^- uptake and NO_3^- depletion decreased with increasing NH_4^+ (Figure 12), which we attribute to NH_4^+ inhibition of NO_3^- uptake (Goeyens et al., 1995). By contrast, at the non-LCIS stations, NO_3^- depletion and ambient NH_4^+ concentration showed a positive relationship, consistent with NO_3^- -fuelled phytoplankton growth being followed by intense remineralization and grazing, both of which can yield elevated NH_4^+ (R  nner et al. 1983; El-Sayed 1984; Semeneh et al. 1998).

Previous studies conducted in MIZ and CCSZ of the Weddell Sea have shown that NH_4^+ concentrations $\geq 0.5 \mu\text{M}$ can inhibit NO_3^- uptake, particularly by diatoms, resulting in phytoplankton (including diatoms) preferentially consuming NH_4^+ over NO_3^- . For example, Goeyens et al. (1995) observed a Weddell Sea phytoplankton community dominated by diatoms prior to NH_4^+ accumulation, but once surface waters became enriched in NH_4^+ , diatom dominance ceased. The authors concluded that diatoms were unable to bloom despite the elevated NO_3^- concentrations because of the inhibitory effect of NH_4^+ , while non-siliceous, smaller phytoplankton species flourished because their preferred N source is NH_4^+ . In our study, although NH_4^+ inhibition of ρNO_3^- apparently occurred at LCIS (Figure 12), ρNO_3^- was on average as high as ρNH_4^+ and was never zero (Table 2) – in other words, the elevated ambient NH_4^+ concentrations did not prevent NO_3^- uptake even though it appears to have slowed it. We propose that the mixed community of diatoms and *P. antarctica* present at the time of our sampling meant that diatoms were able to assimilate mainly NO_3^- while *P. antarctica* consumed the NH_4^+ , preventing this reduced N form from accumulating to fully inhibitory concentrations. While the reliance of *P. antarctica* on NH_4^+ over NO_3^- represents a missed opportunity for carbon export given that these phytoplankton are known to fix up to 50% more carbon than diatoms per mole of PO_4^{3-} consumed (Arrigo et al., 1999), that the diatoms were able to proliferate in the face of elevated NH_4^+ may have partly compensated for this. Earlier in the season when NH_4^+ concentrations were negligible, it is likely that the f-ratios at LCIS were >0.5 and comparable to those estimated

for the FIS stations, as observed at Larsen A and B in early summer (Goeyens et al., 1995; Cape et al., 2014). We conclude that elevated NH_4^+ may have weakened carbon export potential at LCIS in January/February 2019 through its effect on whole-community NO_3^- uptake. Carbon export may have been further inhibited later in the season as NH_4^+ concentrations continued to increase following remineralisation of the phytoplankton bloom, coupled with the seasonal decrease in daylight that is expected to shift the phytoplankton community to proportionally higher NH_4^+ dependence (Lourey et al., 2003; Philibert et al., 2015; Glibert et al., 2016; Deary, 2020; Smart et al., 2020).

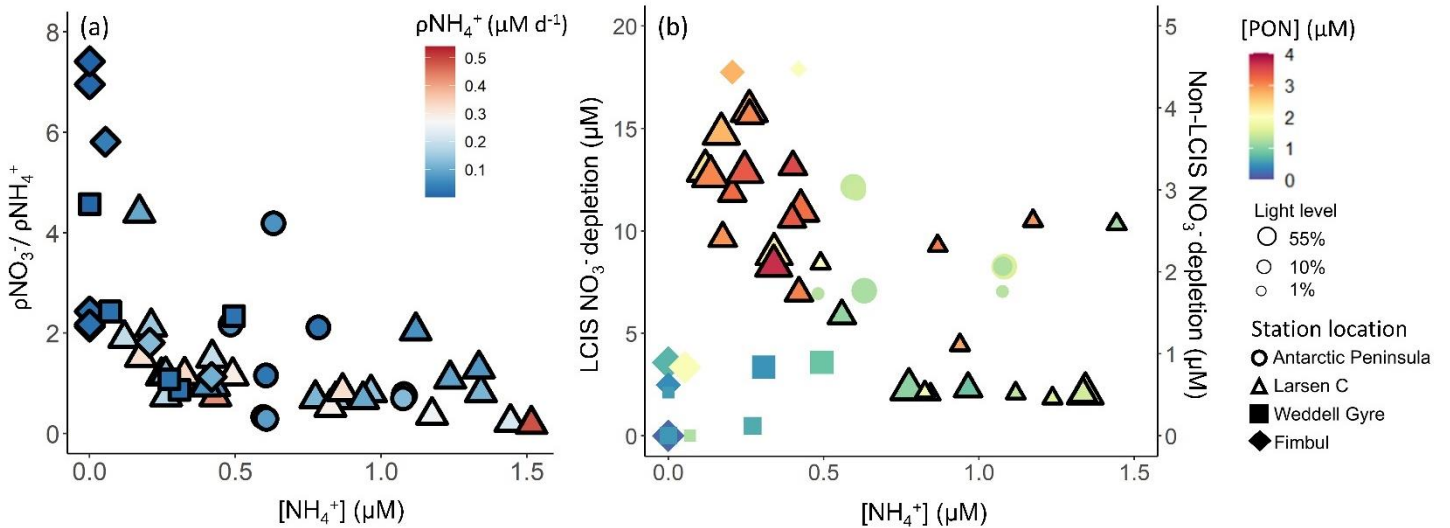


Figure 12. (a) NO_3^- uptake normalised to NH_4^+ uptake as a function of NH_4^+ concentration and b) NO_3^- depletion versus NH_4^+ concentration. The symbols in panel (a) are coloured by NH_4^+ uptake rate (ρNH_4^+) and in panel (b) by PON concentration. In panel (b), the symbol size indicates the incubation light level, NO_3^- depletion at LCIS corresponds with the left y-axis, and NO_3^- depletion at all other (“non-LCIS”) stations corresponds with the right y-axis.

4.3. Broader biogeochemical implications at LCIS

LCIS is a region of deep-water formation, such that the biogeochemical properties of ASW influence those of MWDW and the bottom waters. Our data indicate significant net depletion of nutrients from ASW over the summer growing season. These nutrients would have been converted to organic matter that was either consumed by zooplankton or exported from the euphotic zone to be decomposed by heterotrophic bacteria, in the water column or on the shelf, or consumed by the benthic community. The subsurface remineralisation of organic matter acts to increase the CO_2 and nutrient reservoir of WW and shelf waters (ISW and HSSW; both precursors of CDW). Some portion of this CO_2 is effluxed to the atmosphere when WW upwells along the front of the ice shelf, while the remainder will be mixed into MWDW and eventually transferred to the bottom waters where it will be stored for hundreds of years (Ito et al. 2010). Exported organic matter that escapes water-column and on-shelf remineralization settles on the seafloor where a small fraction is buried and thus removed from the ocean-atmosphere system, while the bulk of the organic matter is consumed by the benthic community and ultimately converted back to CO_2 (Isla et al., 2006, 2011; Pineda-Metz et al., 2019). The CO_2 and nutrients recycled by the benthos may be resupplied to the surface during upwelling, whereupon remineralized CO_2 can escape to the atmosphere. Biological activity and nutrient drawdown at LCIS, and the limitations thereon, thus affect the CO_2 and nutrient content of the bottom waters, as well as the energy supply to the benthos and the extent to which CO_2

is removed from the atmosphere on climate-relevant timescales. The $\text{Si(OH)}_4\text{:NO}_3\text{:PO}_4^{3-}$ ratio at depth at LCIS (average of 2:1:0.07 below 150 m) implicates diatoms as the main biological driver of nutrient conditions in MWDW, and by extension the bottom waters, throughout the Weddell Sea. Although the dominance of *P. antarctica* in early and mid-summer does not appear to affect the nutrient properties of MWDW, it may influence its CO_2 content. *P. antarctica* consume approximately twice as much carbon per mole of PO_4^{3-} as diatoms, and the colonial forms have been observed to rapidly sink out of the water column, thereby transporting large quantities of carbon to depth (Arrigo et al., 2000; Ditullio et al., 2000). The dominance of *P. antarctica* at LCIS may thus be important for carbon storage in MWDW and the bottom waters, as well as for the transport of organic matter to the benthos.

As SSTs rise and sea-ice melts, a shift from *P. antarctica*- to diatom-dominated phytoplankton blooms is expected because diatoms flourish in areas of recent sea-ice melt (Boyd and Doney 2002; Arrigo and van Dijken 2003; Petrou et al. 2016; Ferreira et al. 2020). Our results are consistent with this floristic shift hypothesis. For example, at L10 where recent sea-ice melt (Figure 2a and c) had increased water column stratification, a different phytoplankton community was observed compared to the other LCIS stations, with diatoms dominating over *P. antarctica* (Figure 9). By contrast, at other LCIS stations, *P. antarctica* dominated the biomass due to the low light conditions caused by the deep MLDs that initially characterize coastal polynyas. Given the anomalously high carbon-to-nutrient content of *P. antarctica*, a shift to diatom-dominated phytoplankton blooms may negatively affect the export and storage of carbon in MWDW and the bottom waters. However, rising SSTs will also lead to increased glacial and ice shelf melt, further stratifying the adjacent water column and increasing the iron supply (Petrou et al., 2016). It is projected that these conditions will favour blooms of heavily-silicified diatom species that are known to sink rapidly out of the mixed layer or, if consumed, their frustules are expected to survive the gut passages of copepods, potentially resulting in increased carbon export (Assmy et al., 2013). However, this increase is unlikely to be two-fold that presently contributed by *P. antarctica*. Additionally, the sinking shells of heavily-silicified diatoms have at times been observed to be devoid of organic carbon (Smetacek, 2000; Assmy et al., 2013), which would further decrease the carbon export potential of diatoms compared to colonial *P. antarctica*. In net, the expected floristic shift may lead to decreased carbon export at the ice shelves, subsequently decreasing the carbon content of the MWDW formed at LCIS and/or the food supply to the benthos. Further investigation of the drivers of phytoplankton community composition is required to validate these hypotheses, particularly with regards to the response of Antarctic phytoplankton to warming, as well as to how changes in the surface ecosystem are transferred to and reflected in the biogeochemistry of bottom waters and benthic ecosystem functioning.

5. Conclusions

We investigated the summertime productivity of understudied regions of the Weddell Sea, including LCIS, along with the potential importance of different phytoplankton groups for biomass production, nutrient consumption, and carbon export potential. Our data show that mixed-layer nutrient depletion ratios are determined by the dominant phytoplankton group. The lowest Si:N and highest N:P depletion ratios were observed at LCIS where *P. antarctica* was dominant, while the highest Si:N and lowest N:P depletion ratios occurred at FIS and in the WG where diatoms dominated. The variability in phytoplankton community composition appears to have been largely driven by mechanisms controlling water column stratification. *P. antarctica* are low-light specialists and

proliferated at LCIS due to the deep mixed layers that occurred early in the season, while diatoms succeeded at stations where the mixed layer was shallow, induced by sea-ice melt. Not only does the observed relationship between phytoplankton community composition and the nutrient depletion ratios have implications for the stoichiometry of the deep-water nutrient reservoir, but it likely also has consequences for carbon export and storage (Brzezinski et al. 2003; Weber and Deutsch 2010).

Although the waters adjacent to LCIS were characterized by the highest NO_3^- uptake rates, they also yielded the lowest f-ratios. We attribute these f-ratios to a degree of NH_4^+ inhibition of NO_3^- uptake, which translates to a missed opportunity for carbon export (Cochlan and Bronk, 2003) and potentially, decreased long-term storage in bottom waters, particularly since neither NO_3^- nor iron appeared to be limiting at the time of our sampling. Additional investigation is required to ascertain the persistence of NH_4^+ inhibition in the Antarctic CCSZ, particularly in regions of deep-water formation (e.g., at FRIS). Furthermore, given the prediction that the Weddell Sea's upper water column will become more stratified with climate change (Pörtner et al., 2014; Sallée et al., 2013; Stammerjohn et al., 2012), it is essential that we improve our understanding of the physical and chemical drivers of phytoplankton community composition and function if we are to better predict changes to ocean carbon cycling and drawdown via the biological carbon pump.

6. Figure and table captions

Figure 1. Maps of the Weddell Sea, Larsen C Ice Shelf (LCIS; insert a) and Fimbul Ice Shelf (FIS; insert b) showing the position of the stations where rate experiments were conducted during the Weddell Sea Expedition in January/February 2019. The symbols represent the different regions of the Weddell Sea sampled during the expedition (circle – Antarctic Peninsula (AP); diamond – FIS; triangle – LCIS; square – Weddell Gyre (WG)). The general cyclonic circulation of the Weddell Gyre (dashed blue arrow) is illustrated on the central map, with the dashed black arrows indicating the input of modified water masses from Filchner-Ronne Ice shelf (FRIS) and LCIS (Gordon et al. 1993; Schröder et al. 2002; Schodlok et al. 2002). The hypothesized circulation at LCIS (Nicholls et al. 2004; Hutchinson et al. 2020) is shown by the dashed light-blue arrow in insert (a). The 3.125 km sea-ice concentration data from 31 January 2020 shown in the central panel were taken from <ftp://ftp-projects.cen.uni-hamburg.de/seaice/AMSR2/3.125km> and the bathymetry data (inserts a and b) were taken from ETOPO1 (NOAA National Geophysical Data Center 2009).

Figure 2. Depth profiles of (a) potential density (σ_θ), (b) potential temperature, (c) absolute salinity, and (d) photosynthetically active radiation (PAR) in the upper 150 m and (e) σ_θ , (f) potential temperature, and (g) absolute salinity in the upper 1500 m at all stations. The water masses present at each station, identified by their temperature and salinity characteristics, are denoted in panels (e-g) as follows: WSBW – Weddell Sea Bottom Water, WSDW – Weddell Sea Deep Water, WDW – Warm Deep Water, MWDW – Modified Warm Deep Water, ISW – Ice Shelf Water, HSSW – High Salinity Shelf Water, WW – Winter Water, ASW – Antarctic Surface Water. In panel (f), the dark yellow rectangle indicates HSSW. The general station locations are indicated by the different marker colours: red shades – Antarctic Peninsula, green shades – Larsen C Ice Shelf, blue shade – Weddell Gyre, light purple shades – early summer Fimbul Ice Shelf, and dark purple – late summer Fimbul Ice Shelf.

Figure 3. Depth profiles (0-500 m) of (a) NH_4^+ , (b) urea-N, (c) NO_2^- , (d) NO_3^- , (e) Si(OH)_4 , and (f) PO_4^{3-} concentrations. For all panels, the error bars represent ± 1 SD of replicate samples ($n = 2-3$). For NO_3^- , which was calculated as $\text{NO}_3^- + \text{NO}_2^- - \text{NO}_2^-$, error has been propagated according to standard statistical practices. Note that the x-axis scales in panels (d-f) do not start at zero.

Figure 4. Depth profiles (0-150 m) of (a) NO_3^- depletion, (b) Si(OH)_4 depletion, and (c) PO_4^{3-} depletion at each station. Also shown are scatterplots of (d) Si(OH)_4 depletion versus total N depletion (coloured symbols; see text for details) and Si(OH)_4 depletion versus NO_3^- depletion (grey symbols) and (e) PO_4^{3-} depletion versus total N depletion (coloured symbols) and PO_4^{3-} depletion versus NO_3^- depletion (grey symbols) at each station. The dashed line in panel (d) represents the 1:1 Si:N depletion ratio, expected for iron-replete diatoms (Ragueneau et al. 2000; Hutchins and Bruland 1998; Takeda 1998; Mosseri et al. 2008), while the dotted lines represent the 2:1 Si:N ratio, expected for iron-limited diatoms (Arrigo et al., 1999; Franck et al., 2000; Brzezinski et al., 2003; Green and Sambrotto, 2006; Mosseri et al., 2008; Weber and Deutsch, 2010a; Martiny et al., 2013), and the 1:2 Si:N ratio, indicative of enhanced activity of non-siliceous phytoplankton. The dashed line in panel (e) represents the 16:1 N:P depletion ratio (the Redfield ratio), while the dotted lines represent the 20:1 N:P ratio, expected for *P. antarctica*, and the 14:1 N:P ratio, expected for iron-replete diatoms (Hutchins and Bruland 1998; Takeda 1998; Arrigo et al. 1999; Ragueneau et al. 2000; Mosseri et al. 2008).

Figure 5. Bar plots of (a, d, g) POC concentrations, (b, e, h) PON concentrations, and (c, f, i) biomass C:N ratios measured at the 55% (a-c), 10% (d-f), and 1% light levels (g-i). The stations are labelled on the x-axis, and the general stations locations are indicated by the different colours: red shades – Antarctic Peninsula, green shades – Larsen C Ice Shelf, blue shade – Weddell Gyre, light purple shades – early summer Fimbul Ice Shelf, and dark purple – late summer Fimbul Ice Shelf. The dotted black horizontal line in panels (c), (f), and (i) shows the Redfield C:N ratio of 6.63. The purple star in panel (i) indicates the anomalously high C:N ratio estimated for the 1% PAR depth at station F2. The error bars represent ± 1 SD of replicate samples ($n = 2-6$). Where applicable, the error has been propagated according to standard statistical practices.

Figure 6. Daily rates of (a, e, i) NPP, (b, f, j) ρNO_3^- , (c, g, k) ρNH_4^+ , and (d, h, l) purea for the 55% (a-d), 10% (e-h), and 1% light levels (i-l). Where there are no bars in panels (d), (h) and (l), no data are available. The stations are labelled on the x-axis, and the general station locations are indicated by the different colours: red shades – Antarctic Peninsula, green shades – Larsen C Ice Shelf, blue shade – Weddell Gyre, light purple shades – early summer Fimbul Ice Shelf, and dark purple – late summer Fimbul Ice Shelf. The error bars represent ± 1 SE of replicate experiments ($n = 2$).

Figure 7. Depth profiles of NO_2^- oxidation rates measured at each station (a) between the surface and 500 m, and (b) within the euphotic zone.

Figure 8. Euphotic zone-integrated f-ratios estimated for each station. The black-hashed and white bars show the difference between the $f\text{-ratio}_{(\text{excluding urea})}$ (higher value; equation 4a) and the $f\text{-ratio}_{(\text{including urea})}$ (lower value;

equation 4b), with the black-hashed bars indicating the stations where urea uptake was measured and the white bars where it was estimated (see text for details).

Figure 9. The (a, d) cell counts, (b, e) relative cell abundances, (c) log-transformed biovolume, and (f) carbon biomass of all phytoplankton groups identified from (a-c) surface flow cytometry samples and (d-f) plankton net-tow samples. The stations are labelled on the x-axis. Where there are no bars in panels (d), (e), and (f), no data are available. Carbon biomass estimates in panel (f) are shown only for the prymnesiophyte, *P. antarctica*, and the diatom species.

Figure 10. Euphotic zone-averaged rates of (a) NPP versus SST, (b) ρNO_3^- versus euphotic zone depth (Z_{eu}), (c) N uptake (left y-axis) versus PON (bottom x-axis) and NPP (right y-axis) versus POC (top x-axis), (d) ρNH_4^+ versus NH_4^+ concentration, and (e) purea versus urea concentration, as well as (f) the concentrations of NH_4^+ (black outlined symbols; left y-axis) and urea (grey outlined symbols; right y-axis) versus PON at each station. The symbols in panel (a) are coloured by ρNO_3^- , in panel (b) by NO_3^- concentration, and in panel (c) by NPP (pink), ρNO_3^- (black), ρNH_4^+ (blue), and purea (grey).

Figure 11. Scatterplots of (a) the Si:N depletion ratio (i.e., Si(OH)_4 -to-total N depletion) versus the % diatom abundance, (b) N:P depletion ratio (i.e., total N-to- PO_4^{3-} depletion) versus the % *P. antarctica* abundance, (c) % of total N (i.e., $\text{NO}_3^- + \text{NH}_4^+ + \text{urea}$) assimilated as NO_3^- versus the % diatom abundance, and (d) % of total N assimilated as regenerated N (i.e., $\text{NH}_4^+ + \text{urea}$) versus the % *P. antarctica* abundance at each station.

Figure 12. (a) NO_3^- uptake normalised to NH_4^+ uptake as a function of NH_4^+ concentration and b) NO_3^- depletion versus NH_4^+ concentration. The symbols in panel (a) are coloured by NH_4^+ uptake rate (ρNH_4^+) and in panel (b) by PON concentration. In panel (b), the symbol size indicates the incubation light level, NO_3^- depletion at LCIS corresponds with the left y-axis, and NO_3^- depletion at all other (“non-LCIS”) stations corresponds with the right y-axis.

Table 1. Euphotic zone-averaged N nutrient concentrations, nutrient depletions, and nutrient depletion ratios at each station occupied in the Weddell Sea in January/February 2019. Values shown are averages ± 1 SD ($n \geq 2$), with error propagated according to standard statistical practices where appropriate. “—” indicates no available data.

Table 2. Euphotic zone-integrated and averaged rates at each station occupied in the Weddell Sea in January/February 2019. Values shown are averages ± 1 SD ($n \geq 2$), with error propagated according to standard statistical practices where appropriate. “—” indicates no available data. The values shown in italics (i.e., purea) were estimated rather than measured (see text for details).

7. Author contributions

RF led the study and writing of the manuscript. SF contributed substantially to writing the manuscript, and designed the experiments with RF and TB. RF and JB carried out the experiments. JB, TB, SF, KS, and SS assisted with sampling and data generation, and contributed to writing the manuscript.

8. Acknowledgements

We thank Captain Knowledge Bengu, Captain Freddie Ligthelm, and the exceptional crew of the RV *SA Agulhas II*, as well as the Weddell Sea Expedition 2019. We also thank R. Audh, T. Henry, K. Hutchinson, and H. Luyt for assistance at sea, R. Roman for help with nutrient analyses, the University of Cape Town (UCT) Marine Biogeochemistry Lab, the High-Resolution Transmission Electron Microscopy Unit of the Nelson Mandela University, I. Newton and J. Luyt at the UCT Stable Light Isotope Laboratory, K. Pecsok Ewert at the UC Davis Stable Isotope Facility, and T. Reid and L. Haraguchi for assistance with flow cytometry analyses. We are grateful to S. Moreau and an anonymous reviewer for their insightful comments that improved this manuscript. This research was supported by the Flotilla Foundation through a grant to S.E.F. and T.B.; the South African National Antarctic Program through grants 105539, 117035, and 129232 to S.E.F.; the South African National Research Foundation through postgraduate fellowships to R.F.F., J.M.B., S.S. and K.A.M.S.; UCT through a Science Faculty Fellowship to R.F.F., Vice-Chancellor Doctoral Research Scholarships and Postgraduate Merit Awards to R.F.F., J.M.B. and S.S., and a Vice-Chancellor Future Leaders 2030 award to S.E.F.; and the African Academy of Sciences/Royal Society through a FLAIR Fellowship to S.E.F. The authors also acknowledge the South African Department of Science and Innovation's Biogeochemistry Research Infrastructure Platform (BIOGRIP) and Shallow Marine and Coastal Research Infrastructure (SMCRI). The data discussed in this manuscript are available in the Zenodo database and can be found at <https://doi.org/10.5281/zenodo.5567017>.

9. References

- Alderkamp, A.-C., Kulk, G., Buma, A. G. J., Visser, R. J. W., Dijken, G. L. Van, Mills, M. M., and Arrigo, K. R.: The effect of iron limitation on the photophysiology of *Phaeocystis Antarctica* (Prymnesiophyceae) and *Fragilariopsis cylindrus* (Bacillariophyceae) under dynamic irradiance, *J. Phycol.*, 48, 45–59, <https://doi.org/10.1111/J.1529-8817.2011.01098.X>, 2012.
- Altabet, M. A. and Francois, R.: Nitrogen isotope biogeochemistry of the Antarctic polar frontal zone at 170°W, *Deep. Res. Part II Top. Stud. Oceanogr.*, 48, 4247–4273, [https://doi.org/10.1016/S0967-0645\(01\)00088-1](https://doi.org/10.1016/S0967-0645(01)00088-1), 2001.
- Arrigo, K. R., Robinson, D. H., Worthen, D. L., Dunbar, R. B., DiTullio, G. R., VanWoert, M., and Lizotte, M. P.: Phytoplankton community structure and the drawdown of nutrients and CO₂ in the Southern Ocean, *Science* (80-.), 283, 365–367, <https://doi.org/10.1126/science.283.5400.365>, 1999.
- Arrigo, K. R., DiTullio, G. R., Dunbar, R. B., Robinson, D. H., VanWoert, M., Worthen, D. L., and Lizotte, M. P.: Phytoplankton taxonomic variability in nutrient utilization and primary production in the Ross Sea, *J. Geophys. Res. Ocean.*, 105, 8827–8846, <https://doi.org/10.1029/1998jc000289>, 2000.
- Arrigo, K. R. and van Dijken, G. L.: Phytoplankton dynamics within 37 Antarctic coastal polynya systems, *J. Geophys. Res. Ocean.*, 108, <https://doi.org/10.1029/2002jc001739>, 2003.
- Arrigo, K. R., van Dijken, G., and Long, M.: Coastal Southern Ocean: A strong anthropogenic CO₂ sink, *Geophys. Res. Lett.*, 35, 1–6, <https://doi.org/10.1029/2008GL035624>, 2008.
- Arteaga, L. A., Boss, E., Behrenfeld, M. J., Westberry, T. K., and Sarmiento, J. L.: Seasonal modulation of phytoplankton biomass in the Southern Ocean, *Nat. Commun.* 2020 111, 11, 1–10, <https://doi.org/10.1038/s41467-020-19157-2>, 2020.
- Assmy, P., Smetacek, V., Montresor, M., Klaas, C., Henjes, J., Strass, V. H., Arrieta, J. M., Bathmann, U., Berg,

1152 G. M., Breitbarth, E., Cisewski, B., Friedrichs, L., Fuchs, N., Herndl, G. J., Jansen, S., Krägel, S., Latasa,
 1153 M., Peeken, I., Röttgers, R., Scharek, R., Schüller, S. E., Steigenberger, S., Webb, A., and Wolf-Gladrow, D.:
 1154 Thick-shelled, grazer-protected diatoms decouple ocean carbon and silicon cycles in the iron-limited Antarctic
 1155 Circumpolar Current., *Proc. Natl. Acad. Sci. U. S. A.*, 110, 20633–8, <https://doi.org/10.1073/pnas.1309345110>,
 1156 2013.
 1157 Bendschneider, K., Robinson, R. J., Margeson, J. H., Suggs, J. C., Midgett, M. R., Method, C. R., Dussin, R.,
 1158 Curchitser, E. N., Stock, C. A., Van Oostende, N., Galán, A., Zirbel, M. J., Saldías, G. S., Chan, F., Letelier, R.,
 1159 Najjar, G., Sarmiento, J. L., Xi, S., Scientific, T., Berelson, W. M., McManus, J., Coale, K. H., Johnson, K. S.,
 1160 Kilgore, T., Burdige, D., Pilskaln, C., Flohr, A., Van Der Plas, A. K., Emeis, K. C., Mohrholz, V., and Rixen,
 1161 T.: A New Spectrophotometric Method for the Determination of Nitrite in Sea Water, *J. Mar. Res.*, 11, 0–1,
 1162 <https://doi.org/10.1357/0022240963213673>, 2020.
 1163 Berges, J. A. and Mulholland, M. R.: Enzymes and Nitrogen Cycling, 1385–1444 pp.,
 1164 <https://doi.org/10.1016/B978-0-12-372522-6.00032-3>, 2008.
 1165 Böhlke, J. K. and Coplen, T. B.: Interlaboratory comparison of reference materials for nitrogenisotope- ratio
 1166 measurements, 1995.
 1167 Böhlke, J. K., Mroczkowski, S. J., and Coplen, T. B.: Oxygen isotopes in nitrate: New reference materials for
 1168 ^{18}O : ^{17}O : ^{16}O measurements and observations on nitrate-water equilibration., *Rapid Commun. Mass*
 1169 *Spectrom.*, 17, 1835–1846, 2003.
 1170 Boyd, P. W. and Doney, S. C.: Modelling regional responses by marine pelagic ecosystems to global climate
 1171 change, *Geophys. Res. Lett.*, 29, 53-1-53–4, <https://doi.org/10.1029/2001gl014130>, 2002.
 1172 Boyd, P. W.: Ironing out algal issues in the Southern Ocean, *Nature*, 304, 396–397, 2004.
 1173 Boyd, P. W., Jickells, T., Law, C. S., Blain, S., Boyle, E. A., Buesseler, K. O., Coale, K. H., Cullen, J. J., De
 1174 Baar, H. J. W., Follows, M., Harvey, M., Lancelot, C., Levasseur, M., Owens, N. P. J., Pollard, R., Rivkin, R.
 1175 B., Sarmiento, J., Schoemann, V., Smetacek, V., Takeda, S., Tsuda, A., Turner, S., and Watson, A. J.:
 1176 Mesoscale iron enrichment experiments 1993-2005: Synthesis and future directions, *Science* (80-.), 315, 612–
 1177 617, <https://doi.org/10.1126/science.1131669>, 2007.
 1178 Boyd, P. W., Doney, S. C., Strzepek, R., Dusenberry, J., Lindsay, K., and Fung, I.: Climate-mediated changes to
 1179 mixed-layer properties in the Southern Ocean: assessing the phytoplankton response, 5, 847–864,
 1180 <https://doi.org/10.5194/bg-5-847-2008>, 2008.
 1181 Boyd, P. W. and Ellwood, M. J.: The biogeochemical cycle of iron in the ocean, *Nat. Geosci.*, 3, 675–682,
 1182 <https://doi.org/10.1038/ngeo964>, 2010.
 1183 Brennecke, W.: Die ozeanographischen Arbeiten der Deutschen Antarktischen Expedition 1911-12, Aus dem
 1184 *Arciv der Deuten Seewarte*, 39, 1–216, 1921.
 1185 Brzezinski, M. A., Dickson, M. L., Nelson, D. M., and Sambrotto, R.: Ratios of Si, C and N uptake by
 1186 microplankton in the Southern Ocean, *Deep. Res. Part II Top. Stud. Oceanogr.*, 50, 619–633,
 1187 [https://doi.org/10.1016/S0967-0645\(02\)00587-8](https://doi.org/10.1016/S0967-0645(02)00587-8), 2003.
 1188 Cape, M. R., Vernet, M., Kahru, M., and Spreen, G.: Polynya dynamics drive primary production in the Larsen
 1189 A and B embayments following ice shelf collapse, *J. Geophys. Res. Ocean.*, 119, 572–594,
 1190 <https://doi.org/10.1002/2013JC009441>, 2014.
 1191 Carvalho, F., Kohut, J., Oliver, M. J., and Schofield, O.: Defining the ecologically relevant mixed-layer depth

for Antarctica's coastal seas, *Geophys. Res. Lett.*, 44, 338–345, <https://doi.org/10.1002/2016GL071205>, 2017.

Cochlan, W. P. and Bronk, D. A.: Effects of ammonium on nitrate utilization in the Ross Sea, Antarctica: Implications for *f*-ratio estimates, 78, 159–178, <https://doi.org/10.1029/078ars10>, 2003.

Cota, G. F., Smith, W. O., Nelson, D. M., Muench, R. D., and Gordon, L. I.: Nutrient and biogenic particulate distributions, primary productivity and nitrogen uptake in the Weddell-Scotia Sea marginal ice zone during winter, *J. Mar. Res.*, 50, 155–181, <https://doi.org/10.1357/002224092784797764>, 1992.

De Baar, H. J. W., Boyd, P. W., Coale, K. H., Landry, M. R., Tsuda, A., Assmy, P., Bakker, D. C. E., Bozec, Y., Barber, R. T., Brzezinski, M. A., Buesseler, K. O., Boyé, M., Croot, P. L., Gervais, F., Gorbunov, M. Y., Harrison, P. J., Hiscock, W. T., Laan, P., Lancelot, C., Law, C. S., Levasseur, M., Marchetti, A., Millero, F. J., Nishioka, J., Nojiri, Y., Van Oijen, T., Riebesell, U., Rijkenberg, M. J. A., Saito, H., Takeda, S., Timmermans, K. R., Veldhuis, M. J. W., Waite, A. M., and Wong, C.-S.: Synthesis of iron fertilization experiments: From the Iron Age in the Age of Enlightenment, *J. Geophys. Res.*, 110, 9–16, <https://doi.org/10.1029/2004JC002601>, 2005.

De Jong, J., Schoemann, V., Lannuzel, D., Croot, P., De Baar, H., and Tison, J. L.: Natural iron fertilization of the Atlantic sector of the Southern Ocean by continental shelf sources of the Antarctic Peninsula, *J. Geophys. Res. Biogeosciences*, 117, <https://doi.org/10.1029/2011JG001679>, 2012.

Deary, A.: A high-resolution study of the early- to late-summer progression in primary production and carbon export potential in the Atlantic Southern Ocean Supervisor : Dr Sarah Fawcett, 2020.

Delmont, T. O., Hammar, K. M., Ducklow, H. W., Yager, P. L., and Post, A. F.: *Phaeocystis antarctica* blooms strongly influence bacterial community structures in the Amundsen Sea polynya, *Front. Microbiol.*, 5, 1–13, <https://doi.org/10.3389/fmicb.2014.00646>, 2014.

DeVries, T.: The Oceanic Anthropogenic CO₂ Sink: Storage, Air-Sea Fluxes, and Transports over the Industrial Era, *Global Biogeochem. Cycles*, 28, 631–647, 2014.

Diamond, D.: QuikChem Method 10-114-21-1-B: Silicate by flow injection analysis., 1994.

Dinniman, M. S., St-Laurent, P., Arrigo, K. R., Hofmann, E. E., and Dijken, G. L. van: Analysis of Iron Sources in Antarctic Continental Shelf Waters, *J. Geophys. Res. Ocean.*, 125, e2019JC015736, <https://doi.org/10.1029/2019JC015736>, 2020.

Ditullio, G. R., Grebmeier, J. M., Arrigo, K. R., and Lizotte, M. P.: Rapid and early export of *Phaeocystis antarctica* blooms in the Ross Sea , Antarctica, 404, 1996–1999, 2000.

Dortch, Q.: The interaction between ammonium and nitrate uptake in phytoplankton, *Mar. Ecol. Prog. Ser.*, 61, 183–201, <https://doi.org/10.3354/meps061183>, 1990.

Dowdeswell, J., Shears, J., Batchelor, C., Christie, F., Rack, W., Montelli, A., Evans, J., Dowdeswell, E., Ottesen, D., Fawcett, S., Bornman, T., Hutchinson, K., Audh, R., Burger, J., Flynn, R., Henry, T., Luyt, H., Smith, S., Spence, K., Woodall, L., Taylor, M., Frinault, B., Bekker, A., Zu, L., van Zilj, C., Matthee, J., and Makgabutlane, M.: The Weddell Sea Expedition 2019: Cruise Scientific Report, <https://doi.org/https://doi.org/10.17863/CAM.58103>, 2019.

Dubelaar, G. B. J. and Jonker, R. R.: Flow cytometry as a tool for the study of phytoplankton, *Sci. Mar.*, 64, 135–156, <https://doi.org/10.3989/scimar.2000.64n2135>, 2000.

Dugdale, R. C. and Goering, J. J.: Uptake of New and Regenerated Forms of Nitrogen in Primary Productivity, *Limnol. Oceanogr.*, 12, 196–206, <https://doi.org/10.4319/lo.1967.12.2.0196>, 1967.

1232 Dugdale, R. C. and Wilkerson, F. P.: The use of ^{15}N to measure nitrogen uptake in eutrophic experimental
1233 considerations1 t2, 3, 1986.

1234 Eicken, H.: The role of sea ice in structuring Antarctic ecosystems, in: *Weddell Sea Ecology*, 3–13, 1993.

1235 El-Sayed, S.: Productivity of the Antarctic Waters — A Reappraisal, in: *Marine Phytoplankton and*
1236 *Productivity. Lecture Notes on Coastal and Estuarine Studies.*, edited by: O., H.-H., L., B., and R., G., Springer
1237 Berlin Heidelberg, 19–34, 1984.

1238 El-Sayed, S. Z. and Taguchi, S.: Primary production and standing crop of phytoplankton along the ice-edge in
1239 the Weddell Sea, *Deep Sea Res. Part A, Oceanogr. Res. Pap.*, 28, 1017–1032, [https://doi.org/10.1016/0198-](https://doi.org/10.1016/0198-0149(81)90015-7)
1240 [0149\(81\)90015-7](https://doi.org/10.1016/0198-0149(81)90015-7), 1981.

1241 Eppley, R. W., Peterson, B.: Particulate organic matter flux and planktonic new production in the deep ocean,
1242 *Nature*, 282, 677–680, 1979.

1243 Fahrbach, E., Rohardt, G., Schröder, M., and Strass, V.: Transport and structure of the weddell gyre, *Ann.*
1244 *Geophys.*, 12, 840–855, <https://doi.org/10.1007/s00585-994-0840-7>, 1994.

1245 Fahrbach, E., Rohardt, G., Scheele, N., Schroder, M., Strass, V., and Wisotzki, A.: Formation and discharge of
1246 deep and bottom water in the northwestern Weddell Sea, *J. Mar. Res.*, 53, 515–538,
1247 <https://doi.org/10.1357/0022240953213089>, 1995.

1248 Ferreira, A., Costa, R. R., Dotto, T. S., Kerr, R., Tavano, V. M., Brito, A. C., Brotas, V., Secchi, E. R., and
1249 Mendes, C. R. B.: Changes in Phytoplankton Communities Along the Northern Antarctic Peninsula: Causes,
1250 Impacts and Research Priorities, *Front. Mar. Sci.*, 7, <https://doi.org/10.3389/fmars.2020.576254>, 2020.

1251 Finkel, Z. V., Quigg, A., Raven, J. A., Reinfelder, J. R., Schofield, O. E., and Falkowski, P. G.: Irradiance and
1252 the elemental stoichiometry of marine phytoplankton, *Limnol. Oceanogr.*, 51, 2690–2701,
1253 <https://doi.org/10.4319/LO.2006.51.6.2690>, 2006.

1254 Franck, V. M., Brzezinski, M. A., Coale, K. H., and Nelson, D. M.: Iron and silicic acid concentrations regulate
1255 Si uptake north and south of the Polar Frontal Zone in the Pacific Sector of the Southern Ocean, *Deep. Res. Part*
1256 *II Top. Stud. Oceanogr.*, 47, 3315–3338, [https://doi.org/10.1016/S0967-0645\(00\)00070-9](https://doi.org/10.1016/S0967-0645(00)00070-9), 2000.

1257 Fripiat, F., Sigman, D. M., Fawcett, S. E., Rafter, P. A., Weigand, M. A., and Tison, J.-L.: New insights into sea
1258 ice nitrogen biogeochemical dynamics from the nitrogen isotopes, *Global Biogeochem. Cycles*, 28, 115–130,
1259 <https://doi.org/10.1002/2013GB004729>, 2014.

1260 Fripiat, F., Meiners, K. M., Vancoppenolle, M., Papadimitriou, S., Thomas, D. N., Ackley, S. F., Arrigo, K. R.,
1261 Carnat, G., Cozzi, S., Delille, B., Dieckmann, G. S., Dunbar, R. B., Fransson, A., Kattner, G., Kennedy, H.,
1262 Lannuzel, D., Munro, D. R., Nomura, D., Rintala, J. M., Schoemann, V., Stefels, J., Steiner, N., and Tison, J. L.:
1263 Macro-nutrient concentrations in Antarctic pack ice: Overall patterns and overlooked processes, 5,
1264 <https://doi.org/10.1525/elementa.217>, 2017.

1265 Fripiat, F., Martínez-García, A., Marconi, D., Fawcett, S., Kopf, S., Luu, V., Rafter, P., Zhang, R., Sigman, D.,
1266 and Haug, G.: Nitrogen isotopic constraints on nutrient transport to the upper ocean, *Nat. Geosci.*, 2021.

1267 Frölicher, T. L., Sarmiento, J. L., Paynter, D. J., Dunne, J. P., Krasting, J. P., and Winton, M.: Dominance of the
1268 Southern Ocean in anthropogenic carbon and heat uptake in CMIP5 models, *J. Clim.*, 28, 862–886, 2015.

1269 Garcia, N. S., Sexton, J., Riggins, T., Brown, J., Lomas, M. W., and Martiny, A. C.: High variability in cellular
1270 stoichiometry of carbon, nitrogen, and phosphorus within classes of marine eukaryotic phytoplankton under
1271 sufficient nutrient conditions, *Front. Microbiol.*, 9, 1–10, <https://doi.org/10.3389/fmicb.2018.00543>, 2018.

1272 Gill, A. E.: Circulation and bottom water production in the Weddell Sea, *Deep. Res. Oceanogr. Abstr.*, 20, 111–
1273 140, [https://doi.org/10.1016/0011-7471\(73\)90048-X](https://doi.org/10.1016/0011-7471(73)90048-X), 1973.

1274 Gleitz, M., Michiel, M. R., Thomas, D. N., Dieckmann, G. S., and Millero, F. J.: Comparison of summer and
1275 winter inorganic carbon, oxygen and nutrient concentrations in Antarctic sea ice brine, *Mar. Chem.*, 51, 81–91,
1276 [https://doi.org/10.1016/0304-4203\(95\)00053-T](https://doi.org/10.1016/0304-4203(95)00053-T), 1995.

1277 Glibert, P. M., Wilkerson, F. P., Dugdale, R. C., Raven, J. A., Dupont, C. L., Leavitt, P. R., Parker, A. E.,
1278 Burkholder, J. M., and Kana, T. M.: Pluses and minuses of ammonium and nitrate uptake and assimilation by
1279 phytoplankton and implications for productivity and community composition, with emphasis on nitrogen-
1280 enriched conditions, *Limnol. Oceanogr.*, 61, 165–197, <https://doi.org/10.1002/lno.10203>, 2016.

1281 Goeyens, L.: Ammonium regeneration in the Scotia-Weddell Confluence area during spring 1988, *Mar. Ecol.*
1282 *Prog. Ser.*, 78, 241–252, <https://doi.org/10.3354/meps078241>, 1991.

1283 Goeyens, L., Tréguer, P., Baumann, M. E. M., Baeyens, W., and Dehairs, F.: The leading role of ammonium in
1284 the nitrogen uptake regime of Southern Ocean marginal ice zones, *J. Mar. Syst.*, 6, 345–361,
1285 [https://doi.org/10.1016/0924-7963\(94\)00033-8](https://doi.org/10.1016/0924-7963(94)00033-8), 1995.

1286 Goffart, A., Catalano, G., and Hecq, J. H.: Factors controlling the distribution of diatoms and *Phaeocystis* in the
1287 Ross Sea, *J. Mar. Syst.*, 27, 161–175, [https://doi.org/10.1016/S0924-7963\(00\)00065-8](https://doi.org/10.1016/S0924-7963(00)00065-8), 2000.

1288 Gonfiantini, R.: Stable isotope reference samples for geochemical and hydrological investigations., *Rep. Advis.*
1289 *Group*, Vienna., 1984.

1290 Gordon, A. L., Huber, B. A., Hellmer, H. H., & Ffield, A.: Deep and bottom water of the Weddell Sea’s western
1291 rim., *Science (80-.)*, 265, 95–97, 1993.

1292 Granger, J. and Sigman, D. M.: Removal of nitrite with sulfamic acid for nitrate N and O isotope analysis with
1293 the denitrifier method, *Rapid Commun. Mass Spectrom.*, 23, 3753–3762, <https://doi.org/10.1002/rcm.4307>,
1294 2009.

1295 Grasshoff, K.: *Methods of seawater analysis*, Weinheim and New York: Verlag Chemie, 1976.

1296 Green, S. E. and Sambrotto, R. N.: Plankton community structure and export of C, N, P and Si in the Antarctic
1297 Circumpolar Current, *Deep. Res. Part II Top. Stud. Oceanogr.*, 53, 620–643,
1298 <https://doi.org/10.1016/j.dsr2.2006.01.022>, 2006.

1299 Gruber, N., Clement, D., Carter, B. R., Feely, R. A., Van Heuven, S., and Hoppema, M.: The oceanic sink for
1300 anthropogenic CO₂ from 1994 to 2007, *Science (80-.)*, 363, 1193–1199, 2019.

1301 Henley, S. F., Tuerena, R. E., Annett, A. L., Fallick, A. E., Meredith, M. P., Venables, H. J., Clarke, A., and
1302 Ganeshram, R. S.: Macronutrient supply, uptake and recycling in the coastal ocean of the west Antarctic
1303 Peninsula, *Deep. Res. Part II Top. Stud. Oceanogr.*, 139, 58–76, <https://doi.org/10.1016/j.dsr2.2016.10.003>,
1304 2017.

1305 Holmes, R. M., Aminot, A., Kerouel, R., Hooker, B. A., and Peterson, B. J.: A simple and precise method for
1306 measuring ammonium in marine and freshwater ecosystems, <https://doi.org/10.1139/cjfas-56-10-1801>, 1999.

1307 Hoppema, M. and Goeyens, L.: Redfield behavior of carbon, nitrogen, and phosphorus depletions in Antarctic
1308 surface water, *Limnol. Oceanogr.*, 44, 220–224, <https://doi.org/10.4319/lo.1999.44.1.0220>, 1999.

1309 Hoppema, M., Stoll, M. H. C., and De Baar, H. J. W.: CO₂ in the Weddell Gyre and Antarctic Circumpolar
1310 Current: Austral autumn and early winter, *Mar. Chem.*, 72, 203–220, [https://doi.org/10.1016/S0304-4203\(00\)00082-7](https://doi.org/10.1016/S0304-4203(00)00082-7), 2000a.

1312 Hoppema, M., Goeyens, L., and Fahrbach, E.: Intense nutrient removal in the remote area off Larsen Ice Shelf
 1313 (Weddell Sea), *Polar Biol.*, 23, 85–94, <https://doi.org/10.1007/s003000050012>, 2000b.
 1314 Hoppema, M.: Weddell Sea is a globally significant contributor to deep-sea sequestration of natural carbon
 1315 dioxide, *Deep. Res. Part I Oceanogr. Res. Pap.*, 51, 1169–1177, <https://doi.org/10.1016/j.dsr.2004.02.011>, 2004.
 1316 Hoppema, M., Middag, R., de Baar, H., Fahrbach, E., van Weerlee, E., and Thomas, H.: Whole season net
 1317 community production in the Weddell Sea, *Polar Biol.*, 31, 101–111, 2007.
 1318 Hoppema, M., Bakker, K., MAC van Heuven, S., van Ooijen, J. C., and de Baar, H. J.: Distributions, trends and
 1319 inter-annual variability of nutrients along a repeat section through the Weddell Sea (1996–2011),
 1320 <https://doi.org/10.1016/j.marchem.2015.08.007>, 2015.
 1321 Hutchins, D. A. and Bruland, K. W.: Iron-limited growth and Si:N ratios in a costal upwelling regime, *Nature*,
 1322 393, 561–564, 1998.
 1323 Hutchinson, K., Deshayes, J., Sallee, J. B., Dowdeswell, J. A., de Lavergne, C., Ansorge, I., Luyt, H., Henry, T.,
 1324 and Fawcett, S. E.: Water Mass Characteristics and Distribution Adjacent to Larsen C Ice Shelf, *Antarctica, J.*
 1325 *Geophys. Res. Ocean.*, 125, 0–2, <https://doi.org/10.1029/2019JC015855>, 2020.
 1326 Isla, E., Rossi, S., Palanques, A., Gili, J. M., Gerdes, D., and Arntz, W.: Biochemical composition of marine
 1327 sediment from the eastern Weddell Sea (Antarctica): High nutritive value in a high benthic-biomass
 1328 environment, *J. Mar. Syst.*, 60, 255–267, <https://doi.org/10.1016/J.JMARSYS.2006.01.006>, 2006.
 1329 Isla, E., Gerdes, D., Rossi, S., Fiorillo, I., Sañé, E., Gili, J.-M., and Arntz, W. E.: Biochemical characteristics of
 1330 surface sediments on the eastern Weddell Sea continental shelf, Antarctica: is there any evidence of seasonal
 1331 patterns?, *Polar Biol.* 2011 348, 34, 1125–1133, <https://doi.org/10.1007/S00300-011-0973-6>, 2011.
 1332 Ito, T., Woloszyn, M., and Mazloff, & M.: Anthropogenic carbon dioxide transport in the Southern Ocean
 1333 driven by Ekman flow, 463, <https://doi.org/10.1038/nature08687>, 2010.
 1334 Jacobs, S. S.: The Antarctic slope front, *Antarct. JUS*, 21, 123–124, 1986.
 1335 Jacobs, S. S.: On the nature and significance of the Antarctic Slope Front, *Mar. Chem.*, 35, 9–24,
 1336 [https://doi.org/10.1016/S0304-4203\(09\)90005-6](https://doi.org/10.1016/S0304-4203(09)90005-6), 1991.
 1337 Jacques, G.: Is the concept of new production—regenerated production valid for the Southern Ocean?, *Mar.*
 1338 *Chem.*, 35, 273–286, [https://doi.org/10.1016/S0304-4203\(09\)90022-6](https://doi.org/10.1016/S0304-4203(09)90022-6), 1991.
 1339 Jennings, J. C., Gordon, L. I., and Nelson, D. M.: Nutrient depletion indicates high primary productivity in the
 1340 Weddell Sea, *Nature*, 309, 51–54, <https://doi.org/10.1038/309051a0>, 1984.
 1341 Kana, T. M. and Glibert, P. M.: Effect of irradiances up to 2000 $\mu\text{E m}^{-2} \text{s}^{-1}$ on marine *Synechococcus*
 1342 WH7803-I. Growth, pigmentation, and cell composition, *Deep Sea Res. Part A, Oceanogr. Res. Pap.*, 34, 479–
 1343 495, [https://doi.org/10.1016/0198-0149\(87\)90001-X](https://doi.org/10.1016/0198-0149(87)90001-X), 1987.
 1344 Kaprelyants, A. S. and Kell, D. B.: Dormancy in stationary-phase cultures of *Micrococcus luteus*: flow
 1345 cytometric analysis of starvation and resuscitation, *1Applied Environ. Microbiol.*, 59, 3187–3196, 1993.
 1346 Karsh, K. L., Trull, T. W., Lourey, M. J., and Sigman, D. M.: Relationship of nitrogen isotope fractionation to
 1347 phytoplankton size and iron availability during the Southern Ocean Iron RElease Experiment (SOIRE),
 1348 *Limnol. Oceanogr.*, 48, 1058–1068, <https://doi.org/10.4319/lo.2003.48.3.1058>, 2003.
 1349 Keffer, T. and Holloway, G.: Estimating Southern Ocean eddy flux of heat and salt from satellite altimetry,
 1350 *Nature*, 332, 624–626, <https://doi.org/10.1038/332624a0>, 1988.
 1351 Keller, D. P., Kriest, L., Koeve, W., and Oschlies, A.: Southern Ocean biological impacts on global ocean

oxygen, *Geophys. Res. Lett.*, 43, 6469–6477, 2016.

Kerr, R., Mata, M. M., Mendes, C. R. B., and Secchi, E. R.: Northern Antarctic Peninsula: a marine climate hotspot of rapid changes on ecosystems and ocean dynamics, *Deep. Res. Part II Top. Stud. Oceanogr.*, 149, 4–9, <https://doi.org/10.1016/j.dsr2.2018.05.006>, 2018.

Klunder, M. B., Laan, P., Middag, R., De Baar, H. J. W., and van Ooijen, J. C.: Dissolved iron in the Southern Ocean (Atlantic sector), *Deep. Res. Part II Top. Stud. Oceanogr.*, 58, 2678–2694, <https://doi.org/10.1016/j.dsr2.2010.10.042>, 2011.

Klunder, M. B., Laan, P., De Baar, H. J. W., Middag, R., Neven, I., and Van Ooijen, J.: Dissolved Fe across the Weddell Sea and Drake Passage: impact of DFe on nutrient uptake, 11, 651–669, <https://doi.org/10.5194/bg-11-651-2014>, 2014.

Koike, I., Holm-Hansen, O., and Biggs, D.: Inorganic nitrogen metabolism by Antarctic phytoplankton with special reference to ammonium cycling, *Mar. Ecol. Prog. Ser.*, 30, 105–116, <https://doi.org/10.3354/meps030105>, 1986.

Lannuzel, D., Schoemann, V., de Jong, J., Chou, L., Delille, B., Becquevort, S., and Tison, J. L.: Iron study during a time series in the western Weddell pack ice, *Mar. Chem.*, 108, 85–95, <https://doi.org/10.1016/j.marchem.2007.10.006>, 2008.

Le Corre, P. and Minas, H.: Distributions et évolution des éléments nutritifs dans le secteur indien de l’Océan Antarctique en fin de période estivale, *Oceanol. Acta*, 6, 365–381, 1983.

Leblanc, K., Arístegui, J., Armand, L., Assmy, P., Beker, B., Bode, A., Breton, E., Cornet, V., Gibson, J., Gosselin, M. P., Kopczynska, E., Marshall, H., Peloquin, J., Piontkowski, S., Poulton, A. J., Quéguiner, B., Schiebel, R., Shipe, R., Stefels, J., Van Leeuwe, M. A., Varela, M., Widdicombe, C., and Yallop, M.: A global diatom database- A bundance, biovolume and biomass in the world ocean, *Earth Syst. Sci. Data*, 4, 149–165, <https://doi.org/10.5194/ESSD-4-149-2012>, 2012.

Llort, J., Lévy, M., Sallée, J.-B., and Tagliabue, A.: Onset, intensification, and decline of phytoplankton blooms in the Southern Ocean, *J. Mar. Sci.*, 72, 1971–1984, <https://doi.org/10.1093/icesjms/fsv053>, n.d.

Locarnini, R. A., Whitworth, T., and Nowlin, W. D.: The importance of the Scotia Sea on the outflow of Weddell Sea Deep Water, *J. Mar. Res.*, 51, 135–153, <https://doi.org/10.1357/0022240933223846>, 1993.

Lomas, M. W. and Glibert, P. M.: Interactions between NH_4^+ and NO_3^- uptake and assimilation: Comparison of diatoms and dinoflagellates at several growth temperatures, *Mar. Biol.*, 133, 541–551, <https://doi.org/10.1007/s002270050494>, 1999.

Lourey, M. J., Trull, T. W., and Sigman, D. M.: Sensitivity of $\delta^{15}\text{N}$ of nitrate, surface suspended and deep sinking particulate nitrogen to seasonal nitrate depletion in the Southern Ocean, *Global Biogeochem. Cycles*, 17, 1–18, <https://doi.org/10.1029/2002gb001973>, 2003.

Martin, J. H., Gordon, R. M., and Fitzwater, S. E.: Iron Limitation, *Limnol. Oceanogr.*, 36, 1793–1802, 1991.

Martínez-García, A., Sigman, D. M., Ren, H., Anderson, R. F., Straub, M., Hodell, D. A., Jaccard, S. L., Eglinton, T. I., and Haug, G. H.: Iron Fertilization of the Subantarctic Ocean During the Last Ice Age, 2014.

Martiny, A. C., Pham, C. T. A., Primeau, F. W., Vrugt, J. A., Moore, J. K., Levin, S. A., and Lomas, M. W.: Strong latitudinal patterns in the elemental ratios of marine plankton and organic matter, *Nat. Geosci.*, <https://doi.org/10.1038/NGEO1757>, 2013.

Mathot, S., Smith, W. O., Carlson, C. A., Garrison, D. L., Gowing, M. M., and Vickers, C. L.: Carbon

partitioning within *phaeocystis antarctica* (prymnesiophyceae) colonies in the ross sea, antarctica, *J. Phycol.*, 36, 1049–1056, <https://doi.org/10.1046/j.1529-8817.2000.99078.x>, 2000.

McIlvin, M. R. and Casciotti, K. L.: Technical updates to the bacterial method for nitrate isotopic analyses, *Anal. Chem.*, 83, 1850–1856, <https://doi.org/10.1021/ac1028984>, 2011.

Mdutyana, M., Thomalla, S. J., Philibert, R., Ward, B. B., and Fawcett, S. E.: The Seasonal Cycle of Nitrogen Uptake and Nitrification in the Atlantic Sector of the Southern Ocean, *Global Biogeochem. Cycles*, 34, 1–29, <https://doi.org/10.1029/2019GB006363>, 2020.

Moisan, T. A. and Mitchell, B. G.: Photophysiological acclimation of *Phaeocystis antarctica* Karsten under light limitation, *Limnol. Oceanogr.*, 44, 247–258, <https://doi.org/10.4319/LO.1999.44.2.0247>, 1999.

Mosseri, J., Quéguiner, B., Armand, L., and Cornet-Barthaux, V.: Impact of iron on silicon utilization by diatoms in the Southern Ocean: A case study of Si/N cycle decoupling in a naturally iron-enriched area, *Deep. Res. Part II Top. Stud. Oceanogr.*, 55, 801–819, <https://doi.org/10.1016/j.dsr2.2007.12.003>, 2008.

Muench, R. D. and Gordon, A. L.: Circulation and transport of water along the western Weddell Sea margin, *J. Geophys. Res.*, 100, 18503–18515, <https://doi.org/10.1029/95jc00965>, 1995.

Nelson, M., Smith, O., Gordon, I., and Huber, A.: nutrient, 92, 7181–7190, 1987.

Nicholls, K. W., Pudsey, C. J., and Morris, P.: Summertime water masses off the northern Larsen C Ice Shelf, Antarctica, *Geophys. Res. Lett.*, 31, 2–5, <https://doi.org/10.1029/2004GL019924>, 2004.

Nicholls, K. W., Østerhus, S., Makinson, K., Gammelsrød, T., and Fahrbach, E.: Ice-ocean processes over the continental shelf of the Southern Weddell Sea, Antarctica: A review, *Rev. Geophys.*, 47, 1–23, <https://doi.org/10.1029/2007RG000250>, 2009.

Nissen, C. and Vogt, M.: Factors controlling the competition between *Phaeocystis* and diatoms in the Southern Ocean in the Southern Ocean, *Biogeosciences Discuss.*, 1–39, <https://doi.org/10.5194/bg-2019-488>, 2021.

Olson, R. J.: Differential photoinhibition of marine nitrifying bacteria: a possible mechanism for the formation of the primary nitrite maximum, *J. Mar. Res.*, 39, 227–238, 1981.

Orsi, A. H., Nowlin, W. D., and Whitworth, T.: On the circulation and stratification of the Weddell Gyre, *Deep. Res. Part I*, 40, 169–203, [https://doi.org/10.1016/0967-0637\(93\)90060-G](https://doi.org/10.1016/0967-0637(93)90060-G), 1993.

Orsi, A. H., Whitworth, T., and Nowlin, W. D.: On the meridional extent and fronts of the Antarctic Circumpolar Current, *Deep. Res. Part I*, 42, 641–673, [https://doi.org/10.1016/0967-0637\(95\)00021-W](https://doi.org/10.1016/0967-0637(95)00021-W), 1995.

Park, M. G., Yang, S. R., Kang, S.-H., Chung, K. H., and Shim, J. H.: Phytoplankton biomass and primary production in the marginal ice zone of the northwestern Weddell Sea during austral summer, *Polar Biol.* 1999 214, 21, 251–261, <https://doi.org/10.1007/S0033000050360>, 1999.

Parsons, T. R., Maita, Y., and Lalli, C. M.: A manual of chemical and biological methods for seawater analysis, 1984.

Paulsen, M. L., Riisgaard, K., Thingstad, T. F., John, M. S., and Nielsen, T. G.: Winter-spring transition in the subarctic Atlantic: Microbial response to deep mixing and pre-bloom production., *Aquat. Microb. Ecol.*, 76, 49–49, 2015.

Peng, X., Fuchsman, C. A., Jayakumar, A., Oleynik, S., Martens-Habbena, W., Devol, A. H., and Ward, B. B.: Ammonia and nitrite oxidation in the eastern tropical North Pacific, *Glob. Biogeochem. Cycles*, 29, 2034–2049, 2015.

Petrou, K., Kranz, S. A., Trimborn, S., Hassler, C. S., Ameijeiras, S. B., Sackett, O., Ralph, P. J., and Davidson,

1432 A. T.: Southern Ocean phytoplankton physiology in a changing climate, *J. Plant Physiol.*, 203, 135–150,
1433 <https://doi.org/10.1016/j.jplph.2016.05.004>, 2016.

1434 Philibert, R., Waldron, H., and Clark, D.: A geographical and seasonal comparison of nitrogen uptake by
1435 phytoplankton in the Southern Ocean, *Ocean Sci.*, 11, 251–267, <https://doi.org/10.5194/OS-11-251-2015>, 2015.

1436 Pineda-Metz, S. E. A., Isla, E., and Gerdes, D.: Benthic communities of the Filchner Region (Weddell Sea,
1437 Antarctica), *Mar. Ecol. Prog. Ser.*, 628, 37–54, <https://doi.org/10.3354/MEPS13093>, 2019.

1438 Pörtner, H. O., Karl, D. M., Boyd, P. W., Cheung, W. W., Lluch-Cota, S. E., Nojiri, Y., and Et, A.: Ocean
1439 systems, in: *Impacts, Adaptation, and Vulnerability. Part A: Global and Sectoral Aspects. Contribution of*
1440 *Working Group II to the Fifth Assessment Report of the Intergovernmental Panel on Climate Change*, edited by:
1441 Field, C. B. and Et, A., Cambridge University Press, 411–484, 2014.

1442 Priddle, J., Boyd, I. L., Whitehouse, M. J., Murphy, E. J., and Croxall, J. P.: Estimates of Southern Ocean
1443 primary production - Constraints from predator carbon demand and nutrient drawdown, in: *Journal of Marine*
1444 *Systems*, 275–288, [https://doi.org/10.1016/S0924-7963\(98\)00043-8](https://doi.org/10.1016/S0924-7963(98)00043-8), 1998.

1445 Probyn, T. A. and Painting, S. J.: Nitrogen uptake by size-fractionated phytoplankton populations in Antarctic
1446 surface waters1, *Limnol. Oceanogr.*, 30, 1327–1332, <https://doi.org/10.4319/LO.1985.30.6.1327>, 1985.

1447 Ragueneau, O., Tréguer, P., Leynaert, A., Anderson, R. F., Brzezinski, M. A., DeMaster, D. J., Dugdale, R. C.,
1448 Dymond, J., Fischer, G., François, R., Heinze, C., Maier-Reimer, E., Martin-Jézéquel, V., Nelson, D. M., and
1449 Quéguiner, B.: A review of the Si cycle in the modern ocean: Recent progress and missing gaps in the
1450 application of biogenic opal as a paleoproductivity proxy, *Glob. Planet. Change*, 26, 317–365,
1451 [https://doi.org/10.1016/S0921-8181\(00\)00052-7](https://doi.org/10.1016/S0921-8181(00)00052-7), 2000.

1452 Revilla, M., Alexander, J., and Glibert, P. M.: Urea analysis in coastal waters: Comparison of enzymatic and
1453 direct methods, *Limnol. Oceanogr. Methods*, 3, 290–299, <https://doi.org/10.4319/lom.2005.3.290>, 2005.

1454 Rönner, U., Sörensson, F., and Holm-Hansen, O.: Nitrogen assimilation by phytoplankton in the Scotia Sea,
1455 *Polar Biol.*, 2, 137–147, <https://doi.org/10.1007/BF00448963>, 1983.

1456 Sallée, J. B., Shuckburgh, E., Bruneau, N., Meijers, A. J., Bracegirdle, T. J., and Wang, Z.: Assessment of
1457 Southern Ocean mixed-layer depths in CMIP5 models: Historical bias and forcing response, *J. Geophys. Res.*
1458 *Ocean.*, 118, 1845–1862, 2013.

1459 Santoro, A. E., Sakamoto, C. M., Smith, J. M., Plant, J. N., Gehman, A. L., Worden, A. Z., Johnson, K. S.,
1460 Francis, C. A., and Casciotti, K. L.: Measurements of nitrite production in and around the primary nitrite
1461 maximum in the central California Current, 10, 7395–7410, <https://doi.org/10.5194/bg-10-7395-2013>, 2013.

1462 Sarmiento, J., Toggweiler, J.: A new model for the role of the oceans in determining atmospheric P CO₂,
1463 *Nature*, 308, 621–624, <https://doi.org/https://doi.org/10.1038/308621a0>, 1984.

1464 Sarmiento, J. L., Gruber, N., Brzezinski, M. A., and Dunne, J. P.: High-latitude controls of thermocline nutrients
1465 and low latitude biological productivity, *Nature*, 427, 56–60, <https://doi.org/10.1038/nature10605>, 2004.

1466 Saxberg, B. E. H. and Kowalski, B. R.: Generalized Standard Addition Method, *Anal. Chem.*, 51, 1031–1038,
1467 <https://doi.org/10.1021/ac50043a059>, 1979.

1468 Scharek, R., Smetacek, V., Fahrbach, E., Gordon, L. I., Rohardt, G., and Moore, S.: The transition from winter
1469 to early spring in the eastern Weddell Sea, Antarctica: Plankton biomass and composition in relation to
1470 hydrography and nutrients, *Deep. Res. Part I*, 41, 1231–1250, [https://doi.org/10.1016/0967-0637\(94\)90042-6](https://doi.org/10.1016/0967-0637(94)90042-6),
1471 1994.

1472 Schodlok, M. P., Hellmer, H. H., & Beckmann, A.: On the transport, variability and origin of dense water masses
 1473 crossing the South Scotia Ridge. *Deep Sea Res. II Trop. Stud. Oceanogr.*, 49, 4807–4825, 2002.
 1474 Schoemann, V., Becquevort, S., Stefels, J., Rousseau, V., and Lancelot, C.: Phaeocystis blooms in the global
 1475 ocean and their controlling mechanisms: A review, *J. Sea Res.*, 53, 43–66,
 1476 <https://doi.org/10.1016/j.seares.2004.01.008>, 2005.
 1477 Schofield, O., Miles, T., Alderkamp, A. C., Lee, S. H., Haskins, C., Rogalsky, E., Sipler, R., Sherrell, R. M., and
 1478 Yager, P. L.: In situ phytoplankton distributions in the Amundsen Sea Polynya measured by autonomous
 1479 gliders, 3, 1–17, <https://doi.org/10.12952/journal.elementa.000073>, 2015.
 1480 Schröder, M., Hellmer, H. H., and Absy, J. M.: On the near-bottom variability in the northwestern Weddell Sea,
 1481 *Deep. Res. Part II Top. Stud. Oceanogr.*, 49, 4767–4790, [https://doi.org/10.1016/S0967-0645\(02\)00158-3](https://doi.org/10.1016/S0967-0645(02)00158-3), 2002.
 1482 Sedwick, P. N., Di Tullio, G. R., and Mackey, D. J.: Iron and manganese in the Ross Sea, Seasonal iron
 1483 limitation in Antarctic, *J. Geophys. Res. Ocean.*, 105, 11321–11336, <https://doi.org/10.1029/2000JC000256>,
 1484 2000.
 1485 Semeneh, M., Dehairs, F., Elskens, M., Baumann, M. E. M., Kopczynska, E. E., Lancelot, C., and Goeyens, L.:
 1486 Nitrogen uptake regime and phytoplankton community structure in the Atlantic and Indian sectors of the
 1487 Southern Ocean, *J. Mar. Syst.*, 17, 159–177, [https://doi.org/10.1016/S0924-7963\(98\)00036-0](https://doi.org/10.1016/S0924-7963(98)00036-0), 1998.
 1488 SI, R., T, T., DW, C., and JG, G.: Primary productivity and nutrient utilization ratios in the Pacific sector of the
 1489 Southern Ocean based on seasonal changes in seawater chemistry, *Deep Sea Res. Part I Oceanogr. Res. Pap.*,
 1490 45, 1211–1234, 1998.
 1491 Sigman, D. M. and Boyle², E. A.: Glacial/interglacial variations in atmospheric carbon dioxide, *NATURE*,
 1492 2000.
 1493 Sigman, D. M., Casciotti, K. L., Andreani, M., Barford, C., Galanter, M., and Böhlke, J. K.: A bacterial method
 1494 for the nitrogen isotopic analysis of nitrate in seawater and freshwater, *Anal. Chem.*, 73, 4145–4153,
 1495 <https://doi.org/10.1021/ac010088e>, 2001.
 1496 Sigman, D. M., Hain, M. P., and Haug, G. H.: The polar ocean and glacial cycles in atmospheric CO₂
 1497 concentration, *Nature*, 466, <https://doi.org/10.1038/nature09149>, 2010.
 1498 Smart, S. M., Fawcett, S. E., Ren, H., Schiebel, R., Tompkins, E. M., Martínez-García, A., Stirnimann, L.,
 1499 Roychoudhury, A., Haug, G. H., and Sigman, D. M.: The Nitrogen Isotopic Composition of Tissue and Shell-
 1500 Bound Organic Matter of Planktic Foraminifera in Southern Ocean Surface Waters, *Geochemistry, Geophys.*
 1501 *Geosystems*, 21, 1–29, <https://doi.org/10.1029/2019GC008440>, 2020.
 1502 Smetacek, V.: The giant diatom dump, *Nat.* 2000 4066796, 406, 574–575, <https://doi.org/10.1038/35020665>,
 1503 2000.
 1504 Smetacek, V., Assmy, P., and Henjes, J.: The role of grazing in structuring Southern Ocean pelagic ecosystems
 1505 and biogeochemical cycles, *Antarct. Sci.*, 16, 541–558, <https://doi.org/10.1017/S0954102004002317>, 2004.
 1506 Smith, J. M., Chavez, F. P., and Francis, C. A.: Ammonium Uptake by Phytoplankton Regulates Nitrification in
 1507 the Sunlit Ocean, *PLoS One*, 9, 108173, <https://doi.org/10.1371/journal.pone.0108173>, 2014.
 1508 Smith, W. O. and Nelson, D. M.: Phytoplankton growth and new production in the Weddell Sea marginal ice
 1509 zone in the austral spring and autumn, *Limnol. Oceanogr.*, 35, 809–821,
 1510 <https://doi.org/10.4319/lo.1990.35.4.0809>, 1990.
 1511 Smith, W. O. and Asper, V. L.: The influence of phytoplankton assemblage composition on biogeochemical

1512 characteristics and cycles in the southern Ross Sea, Antarctica, Deep. Res. Part I Oceanogr. Res. Pap., 48, 137–
 1513 161, [https://doi.org/10.1016/S0967-0637\(00\)00045-5](https://doi.org/10.1016/S0967-0637(00)00045-5), 2001.
 1514 Spiridonov, V. A., Nöthig, E. M., Schröder, M., and Wisotzki, A.: The onset of biological winter in the eastern
 1515 Weddell Gyre (Antarctica) planktonic community, J. Mar. Syst., 9, 211–230, [https://doi.org/10.1016/S0924-7963\(95\)00049-6](https://doi.org/10.1016/S0924-7963(95)00049-6), 1996.
 1517 Stammerjohn, S., Massom, R., Rind, D., and Martinson, D.: Regions of rapid sea ice change: An inter-
 1518 hemispheric seasonal comparison, Geophys. Res. Lett., 39, L06501, 2012.
 1519 Stefels, J. and Van Leeuwe, M. A.: Effects of iron and light stress on the biochemical composition of antarctic
 1520 *Phaeocystis* sp. (Prymnesiophyceae). I. Intracellular DMSP concentrations, J. Phycol., 34, 486–495,
 1521 <https://doi.org/10.1046/j.1529-8817.1998.340486.x>, 1998.
 1522 Strickland, J. D. H. and Parsons, T. R.: A practical handbook of seawater analysis, Bull. Fish. Res. Board
 1523 Canada, 167, 81–86, 1968.
 1524 Strzepek, R. F., Maldonado, M. T., Hunter, K. A., Frew, R. D., and Boyd, P. W.: Adaptive strategies by
 1525 Southern Ocean phytoplankton to lessen iron limitation: Uptake of organically complexed iron and reduced
 1526 cellular iron requirements, Limnol. Oceanogr., 56, 1983–2002, <https://doi.org/10.4319/lo.2011.56.6.1983>, 2011.
 1527 Sunda, W. G. and Huntsman, S. A.: Interrelated influence of iron, light and cell size on marine phytoplankton
 1528 growth, Nature, 390, 389–392, <https://doi.org/10.1038/37093>, 1997.
 1529 Sunda, W. G. and Huntsman, S. A.: High iron requirement for growth, photosynthesis, and low-light
 1530 acclimation in the coastal cyanobacterium *Synechococcus bacillaris*, Front. Microbiol., 6, 561, 2015.
 1531 Takeda, S.: Influence of iron availability on nutrient consumption ratio, Nature, 393, 774–777, 1998.
 1532 Talley, L. D., Pickard, G. L., Emery, W. J., and Swift, J. H.: Southern Ocean, Descr. Phys. Oceanogr., 437–471,
 1533 <https://doi.org/10.1016/b978-0-7506-4552-2.10013-7>, 2011.
 1534 Taylor, B. W., Keep, C. F., Hall, R. O., Koch, B. J., Tronstad, L. M., Flecker, A. S., and Ulseth, A. J.:
 1535 Improving the fluorometric ammonium method: matrix effects, background fluorescence, and standard
 1536 additions, J. North Am. Benthol. Soc., 26, 167–177, [https://doi.org/10.1899/0887-3593\(2007\)26\[167:ITFAMM\]2.0.CO;2](https://doi.org/10.1899/0887-3593(2007)26[167:ITFAMM]2.0.CO;2), 2007.
 1538 Treguer, P. and G, J.: Review Dynamics of nutrients and phytoplankton, and fluxes of carbon, nitrogen and
 1539 silicon in the Antarctic Ocean, edited by: Hempel, G., Springer Berlin Heidelberg, 1992.
 1540 Tréguer, P., Bowler, C., Moriceau, B., Dutkiewicz, S., Gehlen, M., Aumont, O., Bittner, L., Dugdale, R., Finkel,
 1541 Z., Iudicone, D., Jahn, O., Guidi, L., Lasbleiz, M., Leblanc, K., Levy, M., and Pondaven, P.: Influence of diatom
 1542 diversity on the ocean biological carbon pump, Nat. Geosci., <https://doi.org/10.1038/s41561-017-0028-x>, 2017.
 1543 Vernet, M., Geibert, W., Hoppema, M., Brown, P. J., Haas, C., Hellmer, H. H., Jokat, W., Jullion, L., Mazloff,
 1544 M., Bakker, D. C. E., Brearley, J. A., Croot, P., Hattermann, T., Hauck, J., Hillenbrand, C. D., Hoppe, C. J. M.,
 1545 Huhn, O., Koch, B. P., Lechtenfeld, O. J., Meredith, M. P., Naveira Garabato, A. C., Nöthig, E. M., Peeken, I.,
 1546 Rutgers van der Loeff, M. M., Schmidtko, S., Schröder, M., Strass, V. H., Torres-Valdés, S., and Verdy, A.: The
 1547 Weddell Gyre, Southern Ocean: Present Knowledge and Future Challenges, Rev. Geophys., 57, 623–708,
 1548 <https://doi.org/10.1029/2018RG000604>, 2019.
 1549 Vogt, M., O'Brien, C., Peloquin, J., Schoemann, V., Breton, E., Estrada, M., Gibson, J., Karentz, D., Van
 1550 Leeuwe, M. A., Stefels, J., Widdicombe, C., and Peperzak, L.: Global marine plankton functional type biomass
 1551 distributions: <i>Phaeocystis</i> spp., Earth Syst. Sci. Data, 4, 107–120,

1552 <https://doi.org/10.5194/essd-4-107-2012>, 2012.

1553 Volk, T. and Hoffert, M. I.: Ocean Carbon Pumps: Analysis of Relative Strengths and Efficiencies in Ocean-

1554 Driven Atmospheric CO₂ Changes, in: Geophysical Monograph Series, edited by: Sundquist, E. T. and

1555 Broecker, W. S., 1985.

1556 Ward, B. B.: Light and substrate concentration relationships with marine ammonium assimilation and oxidation

1557 rates, *Mar. Chem.*, 16, 301–316, [https://doi.org/10.1016/0304-4203\(85\)90052-0](https://doi.org/10.1016/0304-4203(85)90052-0), 1985.

1558 Ward, B. B.: Temporal variability in nitrification rates and related biogeochemical factors in Monterey Bay,

1559 California, USA, *Mar. Ecol. Prog. Ser.*, 292, 97–109, <https://doi.org/10.3354/meps292097>, 2005.

1560 Weber, T. S. and Deutsch, C.: Ocean nutrient ratios governed by plankton biogeography,

1561 <https://doi.org/10.1038/nature09403>, 2010a.

1562 Weber, T. S. and Deutsch, C.: Ocean nutrient ratios governed by plankton biogeography, *Nature*, 467, 550–554,

1563 <https://doi.org/10.1038/nature09403>, 2010b.

1564 Whitworth, T. and Nowlin, W. D.: Water Masses and Currents of the Southern Ocean at the Greenwich

1565 Meridian, *JOURNAL OF GEOPHYSICAL RESEARCH*, 6462–6476 pp.,

1566 <https://doi.org/10.1029/JC092iC06p06462>, 1987.

1567 Yool, A., Martin, A. P., Fernández, C., and Clark, D. R.: The significance of nitrification for oceanic new

1568 production, <https://doi.org/10.1038/nature05885>, n.d.

1569 Zakem, E. J., Al-Haj, A., Church, M. J., Van Dijken, G. L., Dutkiewicz, S., Foster, S. Q., Fulweiler, R. W.,

1570 Mills, M. M., and Follows, M. J.: Ecological control of nitrite in the upper ocean, *Nat. Commun.*, 9,

1571 <https://doi.org/10.1038/s41467-018-03553-w>, 2018.

1572

1573